Ceramic material under ballistic loading

A numerical approach to sphere impact on ceramic armour material

Simons, Erik

DOI
10.4233/uuid:ee1aa368-86de-44dd-8e14-547709f289e4

Publication date
2020

Document Version
Final published version

Citation (APA)
Simons, E. (2020). *Ceramic material under ballistic loading: A numerical approach to sphere impact on ceramic armour material*. [Dissertation (TU Delft), Delft University of Technology]. https://doi.org/10.4233/uuid:ee1aa368-86de-44dd-8e14-547709f289e4

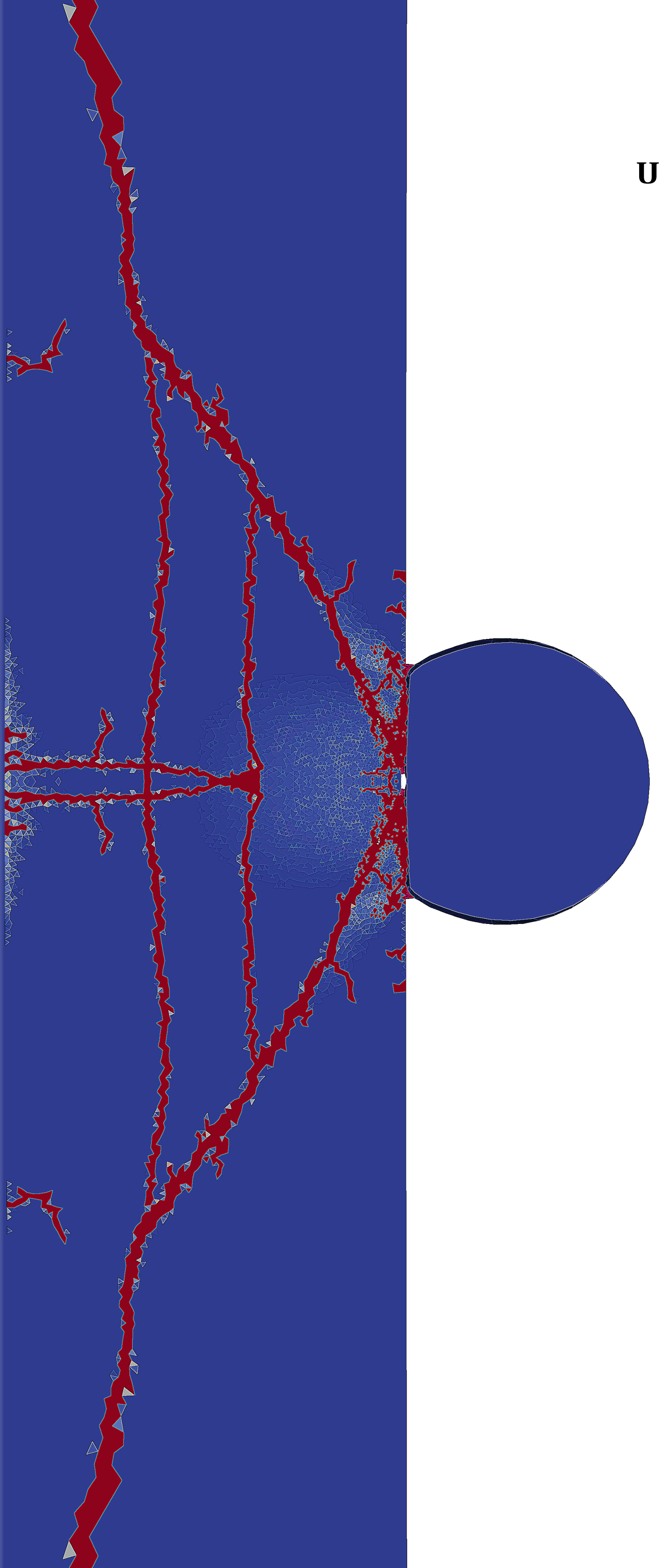

CERAMIC MATERIAL UNDER BALLISTIC LOADING

ERIK CORNELIS SIMONS

CERAMIC MATERIAL UNDER BALLISTIC LOADING

A NUMERICAL APPROACH TO SPHERE IMPACT ON CERAMIC ARMOUR MATERIAL

Propositions

accompanying the dissertation

CERAMIC MATERIAL UNDER BALLISTIC LOADING

A NUMERICAL APPROACH TO SPHERE IMPACT ON CERAMIC ARMOUR MATERIAL

by

Erik Cornelis SIMONS

1. Applying a viscosity to the hydrostatic tensile strength in the Johnson-Holmquist-2 constitutive model leads to numerically sound and physically realistic model predictions.
2. By using two plastic failure strains, brittle failure under tension and ductile failure under compression can be captured in the viscosity regularized Johnson-Holmquist-2 constitutive model, for a single set of parameters.
3. The upgraded viscosity regularized Johnson-Holmquist-2 material model can be used to simulate failure and the sequence of failure events in a ceramic under sphere impact.
4. Using an implicit time integration scheme may lead to faster simulations but will definitely slow down development and implementation of your constitutive model.
5. It is tempting to use our knowledge on 1d wave propagation to explain failure and sequence of failure events in sphere impact. However, complexity soon prevails and wave mechanics brings you nowhere.
6. When developing a constitutive model, ballistic experiments become more useful when they are less spectacular.
7. Writing a paper is an iterative process, talking to your supervisors will precondition the paper to speed up convergence.
8. Group social events are not only fun, they improve your work.
9. Trust in your own competence is a prerequisite for successful completion of a PhD.
10. U.S. swim coach Dave Salo has the training philosophy: “Don’t count the meters, make every meter count.”. The same philosophy should be applied to your work.

These propositions are regarded as opposable and defendable, and have been approved as such by the promotor prof. dr. ir. L. J. Sluys.

Stellingen

behorende bij het proefschrift

CERAMIC MATERIAL UNDER BALLISTIC LOADING
A NUMERICAL APPROACH TO SPHERE IMPACT ON CERAMIC ARMOUR MATERIAL

door

Erik Cornelis SIMONS

1. Het toepassen van een hydrostatische trekstrekte in het Johnson-Holmquist-2 constitutief model zorgt voor numeriek juiste en fysiek realistische model voorspellingen.
2. Door twee plastische faal rekken te gebruiken is het mogelijk bros falen onder trek en ductiel falen onder druk te beschrijven in het door viscositeit geregulariseerde Johnson-Holmquist-2 constitutief model, met een enkele set parameters.
3. Het verbeterde viscositeit geregulariseerde Johnson-Holmquist-2 materiaal model kan worden gebruikt om het falen en de volgorde van falen te simuleren in een keramiek onder sferische inslag.
4. Het gebruik van impliciete tijd integratie kan zorgen voor snellere simulaties, maar zal zeker ontwikkeling en implementatie van het constitutief model vertragen.
5. Het is verleidelijk om kennis van 1d golf voortplanting te gebruiken om het falen en de volgorde van falen te verklaren in sferische inslag. Helaas neemt de complexiteit snel de overhand en kom je met golf voortplanting nergens.
6. Wanneer je een constitutief model ontwikkelt zijn ballistische tests waardevoller als ze minder spectaculair zijn.
7. Het schrijven van een artikel is een iteratief proces, overleg met je supervisors zal het iteratieve proces voorbereiden en de convergentie versnellen.
8. Sociale evenementen met de vakgroep zijn niet alleen leuk, ze verbeteren ook je werk.
9. Vertrouwen in je eigen competentie is een voorwaarde voor een succesvolle afronding van een promotie.
10. De Amerikaanse zwemtrainer Dave Salo gebruikt in zijn trainingen de filosofie: “Tel niet de meters, maar laat elke meter tellen.”. Deze filosofie zou je ook in je werk moeten toepassen.

Deze stellingen worden opponeerbaar en verdedigbaar geacht en zijn als zodanig goedgekeurd door de promotor prof. dr. ir. L. J. Sluys.

CERAMIC MATERIAL UNDER BALLISTIC LOADING

A NUMERICAL APPROACH TO SPHERE IMPACT ON CERAMIC ARMOUR MATERIAL

Proefschrift

ter verkrijging van de graad van doctor
aan de Technische Universiteit Delft,
op gezag van de Rector Magnificus prof. dr. ir. T.H.J.J. van der Hagen,
voorzitter van het College voor Promoties,
in het openbaar te verdedigen op maandag 16 maart 2020 om 15:00 uur

door

Erik Cornelis SIMONS

Ingenieur Civiele Techniek,
Technische Universiteit Delft, Nederland
geboren te Leiden, Nederland.

Dit proefschrift is goedgekeurd door de

promotor : Prof. dr. ir. L.J. Sluys
copromotor : Dr. ir. J. Weerheijm

Samenstelling promotiecommissie:

Rector Magnificus,	voorzitter
Prof. dr. ir. L.J. Sluys,	Technische Universiteit Delft, promotor
Dr. ir. J. Weerheijm,	Technische Universiteit Delft & TNO Defence, Safety & Security, copromotor

Onafhankelijke leden:	
Prof. dr. P. Forquin	Université Grenoble Alpes
Prof. dr. ir. M.G.D. Geers	Technische Universiteit Eindhoven
Prof. dr. M. Veljkovic	Technische Universiteit Delft
Dr. ir. E. Carton	TNO Defence, Safety & Security
Dr. ir. W.G. Sloof	Technische Universiteit Delft
Prof. dr. ir. J.G. Rots	Technische Universiteit Delft, reservelid

Keywords: ceramic, failure, cone crack, finite element method, constitutive modelling

Printed by: Ipskamp Printing B.V.

Front: Cross section of a simulated ceramic target impacted by a spherical steel projectile, showing damage in the ceramic.

Back: Back surface of a simulated ceramic target impacted by a spherical steel projectile, showing damage in the ceramic.

ISBN 978-94-6384-107-8

An electronic version of this dissertation is available at
`http://repository.tudelft.nl/`.

CONTENTS

SUMMARY

Armour systems for ballistic protection can be made from many materials. One type of material used in armour systems is ceramic. Ceramic materials, such as alumina and silicon carbide, can be beneficial in an armour system because of their high hardness and relatively low weight. The high hardness of the ceramic potentially causes a projectile to deform heavily and fracture upon impact with the armour, thereby reducing or even eliminating the threat. The ceramic itself may also damage during the interaction. Although ceramics can damage under impact, they contribute to the protective capability of the armour system as long as they exert a force on the projectile to deform and deceleration it. In order to improve an armour system one does not only need to know when the ceramic component fails, but also how it fails. Once the failure mechanisms of the ceramic are known the armour design may be modified to delay or in an ideal scenario even prevent catastrophic failure of the ceramic. This will eventually result in stronger and lighter armour systems.

Ballistic experiments performed on ceramic material provide a useful source of information. Testing full armour systems shows the protective capabilities of such systems. These tests do however not offer too much insight in the true ceramic behaviour from damage initiation to full failure, simply because the ballistic loads reach far beyond the material strengths and the tests are catastrophic in nature. Performing measurements on the true ceramic behaviour during the ballistic experiments is impossible and even measurements after the test are difficult since the ceramic is often completely pulverized. Instead, simplified tests can be performed to study the pure ceramic behaviour. These can be standard static and dynamic material tests or impact tests under more controlled conditions. Here, the overwhelming forces found in the true ballistic experiments are absent and it is possible to recover the ceramic after the experiment. One of these controlled impact tests is sphere impact. In this test a spherical projectile impacts on an unsupported ceramic tile. This test is simple, cheap, reproducible and compared to full scale armour testing the sphere impact experiments offer a sound failure of the ceramics.

In this thesis sphere impact tests on ceramic material are simulated. The numerical method used for these simulations is the finite element method (FEM). Performing simulations of the sphere impact test can provide new insight in the failure mechanisms and their interaction. The focus of the thesis is the constitutive model for the ceramic, which describes the strength and failure of this material. The well known Johnson-Holmquist-2 (JH2) ceramic material model is used as a starting point. Having a proper constitutive model is tantamount to the success of simulations. Any material model used in simulations should be able to give numerically sound and physically correct results. Unfortunately the JH2 model in its original form does not give numerically sound results, as it suffers from mesh dependency. Furthermore, the JH2 model can be improved to give more physically correct results. In this thesis two variations to the JH2 model are proposed to solve mesh dependency and improve validity of the model, before using the model in sphere impact simulations.

The first modification to the JH2 material model discussed in this thesis is to solve mesh dependency. This dependency arises because the JH2 material model is a softening plasticity model, for which mesh dependency is a notorious problem. This dependency causes spurious locatization of failure and a bias effect of the results on the spatial discretization (i.e. mesh). To solve this a new rate dependency is proposed to the material model, acting on the hydrostatic tensile strength. This is shown to solve the mesh dependency issues and at the same time allows for a realistic description of rate dependent tensile strength. This is the first variation to the JH2 model, which will be refered to as the *JH2-V* model throughout the thesis.

The second modification to the JH2 model is related to the way failure is described in the model. The failure of a ceramic is very brittle under tensile loading, but can exhibit considerable ductility under sufficiently high confining pressures. Comparing the JH2 and JH2-V material models to experiments under a wide range of loading conditions revealed the inability to describe both the brittle and ductile behaviour. A new failure strain formulation is proposed where the behaviour under tensile and compressive loading can be controlled independently. This allows to properly capture both the brittle and ductile response of the material in the constitutive model, for a single set of model parameters. The modified model has been evaluated and validated successfully for a wide range of test conditions. The original formulation failed to do so for a single set of model parameters. The final version of the consitutive model, including both the rate dependency to solve for mesh dependency and the new failure strain formulation, will be refered to as the *upgraded JH2-V* model.

As a final part of this thesis the *upgraded JH2-V* constitutive model is used in sphere impact simulations. The impact experiment is simulated using the Finite Element Method in 3d, with a penalty stiffness contact formulation without friction. Comparing the simulations to new experimental results shows that the upgraded JH2-V model is able to capture all relevant failure mechanisms in sphere impact. It is therefore used to study the sequence of failure mechanisms and the interaction between different failure mechanisms. This clearly reveals the order of failure to be (1) cone cracking and (2) radial cracking during loading by the projectile, followed by (3) lateral cracking during reflection of the projectile.

In this thesis a constitutive model was proposed to describe ceramic material under ballistic loading. This *upgraded JH2-V* model was found to give both mesh independent and physically correct results. The model could be used to study sphere impact on ceramic material and provides a good basis for future research on ceramic armour systems.

SAMENVATTING

Pantsersystemen voor ballistische bescherming kunnen van veel verschillende materialen gemaakt worden. Eén van de materialen die in deze systeem wordt gebruikt is keramiek. Keramische materialen, zoals bijvoorbeeld alumina en silicium carbide, zijn gunstig voor een pantsersysteem vanwege de hoge hardheid en het relatief lage gewicht. De hoge hardheid van het keramiek kan leiden tot grote vervormingen en zelfs opbreken van het projectiel dat inslaat op het pantser, waardoor het gevaar van het projectiel af neemt of zelf helemaal verdwijnt. Het keramiek zelf kan ook beschadigen tijdens de inslag. Ondanks de schade die in een keramisch materiaal optreedt tijdens de inslag, zal het materiaal bijdragen aan de beschermende werking van het pantser zolang er een kracht op het projectiel kan worden uitgeoefend om het af te remmen en te vervormen. Om het pantsersysteem te verbeteren is het niet alleen nodig om te weten wanneer het keramische materiaal faalt, maar ook op welke manier. Zodra de schade mechanismen in het keramische materiaal bekend zijn kan het pantser worden aangepast om het falen van het keramiek te vertragen, of in een ideaal scenario zelfs te voorkomen. Dit zal uiteindelijk leiden tot een sterker en lichter pantser.

Ballistische testen die op keramisch materiaal worden uitgevoerd zijn een belangrijke bron van informatie. Het testen van een volledig pantsersysteem laat de beschermende werking van een dergelijk systeem zien. Deze testen bieden echter geen inzicht in het daadwerkelijke gedrag van het keramiek van beginnend tot en met volledig falen, simpelweg omdat de krachten in een ballistische test vele malen groter zijn dan wat het materiaal aan kan en de test catastrofaal is voor het keramiek. Het meten van het werkelijke materiaal gedrag tijdens een ballistische test is onmogelijk en zelfs metingen na de test zijn moeilijk omdat het keramiek vaak volledig verpulverd is. In plaats hiervan kunnen er vereenvoudigde testen worden uitgevoerd om het pure gedrag van het keramiek te bepalen. Dit kunnen standaard statische of dynamische testen zijn of zelfs gecontroleerde inslag testen. In dergelijke testen is de overweldigende kracht van een ballistische test afwezig en kan het keramiek bestudeerd worden na de test. Eén van deze gecontroleerde testen is de bol inslag test. In deze test slaat een sferisch projectiel in op een vrijstaande keramische tegel. Deze test is simpel, goedkoop, reproduceerbaar en geeft, in vergelijken met een volledige ballistische test, een duidelijk beeld va het faalgedrag van het keramiek.

In deze thesis staat het simuleren van bol inslag op keramisch materiaal centraal. De numerieke methode die hiervoor wordt gebruikt is de eindige elementen methode (EEM). Simuleren van bol inslag testen kan nieuwe inzichten geven in de faalmechanismen en de interactie daartussen. De focus van de thesis ligt bij het constitutief model van het keramiek, waarin de sterkte en het faalgedrag van het materiaal wordt beschreven. Het veelgebruikte model Johnson-Holmquist-2 (JH2) is het gebruikt als startpunt van het onderzoek. Een goed constitutief model is de basis voor succesvolle simulaties. Elk materiaal model dat in een simulatie gebruikt wordt moet numeriek juist en fysiek

correct zijn. Helaas is het JH2 model in originele vorm niet numeriek juist, omdat het model leidt tot mesh afhankelijke resultaten. Daarnaast kan het JH2 model verbeterd worden om de fysieke correctheid van het model te verhogen. In deze thesis zullen er twee variaties op het JH2 model worden voorgesteld om de mesh afhankelijkheid op te lossen en de validiteit van het model te verbeteren, om het vervolgens in bol inslag simulaties te gebruiken.

De eerste aanpassing aan het JH2 model dat in deze thesis wordt besproken is het oplossen van de mesh afhankelijkheid. Deze afhankelijkheid treedt op omdat het JH2 model een verzachtend plasticiteit model is, waarbij mesh afhankelijkheid een notoir probleem is. Deze afhankelijkheid zorgt voor onechte lokalisatie van falen en een beïnvloeding van de resultaten door de ruimtelijke discretisatie (d.w.z. mesh). Om dit probleem op te lossen is een nieuwe snelheidsafhankelijkheid voorgesteld voor het materiaal model, werkende op de alzijdige treksterkte. Het wordt gedemonstreerd dat deze aanpassing de mesh afhankelijkheid oplost en tegelijkertijd zorgt voor een meer realistische beschrijving van de snelheidsafhankelijke treksterkte. Dit is de eerste variatie op het JH2 model, dat in de test van deze thesis het *JH2-V* model zal worden genoemd.

De tweede aanpassing aan het JH2 model is de manier waarop het falen in het model wordt beschreven. Het falen van keramiek is erg bros onder trek belasting, maar kan behoorlijke ductiliteit tonen onder voldoende hoge insluitende drukken. Het vergelijken van de JH2 en JH2-V modellen met experimenten, onder een groot aantal verschillende belastingcondities, laat zien dat beide modellen niet in staat zijn om zowel het brosse als ductiele falen goed te beschrijven. Een nieuwe faal rek formulering is voorgesteld, waar het gedrag onder trek en druk onafhankelijk van elkaar kan worden gecontroleerd. Dit zorgt er voor dat zowel het brosse falen onder trek als het ductiele falen onder druk kan worden beschreven in het constitutieve model, met een enkele set model parameters. Het aangepaste model is geëvalueerd en met succes gevalideerd voor een groot aantal test condities. Met het oorspronkelijke model was het niet mogelijk dit te doen met een enkele set model parameters. Deze laatste versie van het constitutief model, inclusief de snelheidsafhankelijkheid om mesh afhankelijkheid op te lossen, zal het *upgraded JH2-V* model worden genoemd.

Als laatste deel van deze thesis wordt het *upgraded JH2-V* constitutief model gebruikt in simulaties van bol inslag. Dit inslag experiment is gesimuleerd in de eindige element methode in 3d, met een verende contact formulering zonder wrijving. Het vergelijken van de simulaties met nieuwe experimentele resultaten laat zien dat het upgraded JH2-V model in staat is om alle relevante faalmechanismen te beschrijven in bol inslag. Het model is daarom gebruikt om de volgorde van faalmechanismen en de interactie tussen verschillende mechanismen te bestuderen. Dit laat duidelijk zien dat de volgorde van falen bestaat uit (1) het vormen van conische scheuren en (2) radiale scheuren tijdens de voortdurende belasting door het projectiel, gevolgd door (3) laterale scheuren tijdens de reflectie van het projectiel.

In deze thesis is een constitutief model voorgesteld om het faalgedrag van keramisch materiaal te beschrijven onder ballistische belasting. Het is aangetoond dat het *upgraded JH2-V* model zowel mesh onafhankelijke als fysiek correcte resultaten geeft. Het model kan worden gebruikt om bol inslag op keramisch materiaal te bestuderen en vormt een goede basis voor toekomstig onderzoek op keramische pantsersystemen.

1

INTRODUCTION

1.1. GENERAL INTRODUCTION

The Cambridge dictionary defines armour as a “strong covering that protects something, especially the body” [1]. For this purpose humans have used armour in different forms and shapes throughout history. Because the threat of intentional injury by others is still present and constantly changing, design of armour remains a topic of interest.

The materials used in armour systems have changed over time, depending on the type of threats as well as the availability of certain armour materials. Early armour could be made from wood, bones or leather. But these were replaced by metal armours when these materials became available and threats became more serious. The medieval suit of armour is perhaps the most striking example of metal armour. It also illustrates that protection and mobility are (unfortunately) inversely proportional. When the threats in medieval times changed from swords and pikes to crossbows and guns, the suit of armour was quickly abandoned. Steel as an armour material would return during the first world war, both for vehicular and personal protection. Initially steel was used to create helmets, but later even steel body armours were used to protect against shrapnel and rifle shots [2]. Again, the trade-off between mobility and protection played a role and many variations of body armour with textiles and steel were created. The medieval suit and the body armour from the first world war show that this is an age old struggle, which in fact still continues today. In the development of armour systems one always strives to create lighter (and stronger) armour systems [3].

During the Vietnam war ceramic material was first used in armour systems. In the Vietnam war a large number of helicopters transported soldiers on the battlefields. Take-off and landing was a dangerous phase of the transport, as many pilots would get shot through the helicopter floors [4]. As a solution, the floors had to be armoured, with an obvious restriction on weight. Ceramic materials were known to be light and extremely hard, hence were considered for these armour systems. The application of ceramic armour greatly reduced the number of casualties, reportedly by more than 50% [2]. After the Vietnam war the use of ceramics in armour systems continued and research has been ongoing ever since.

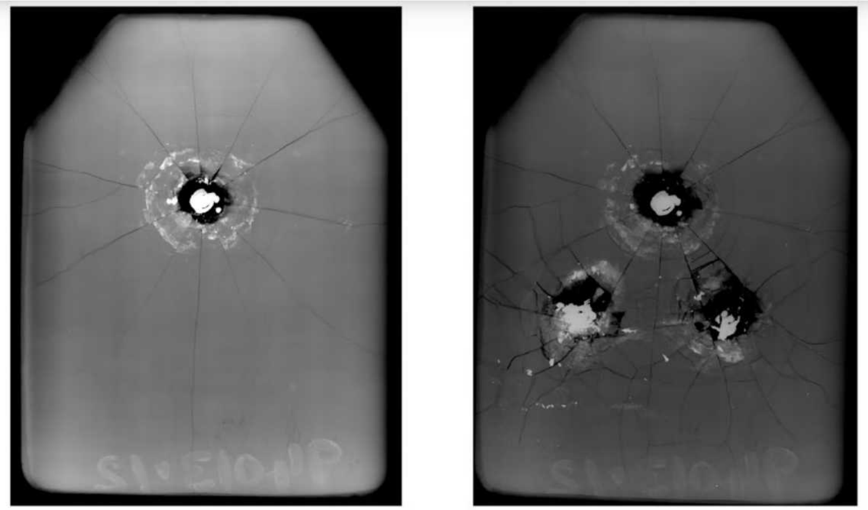

Figure 1.1: Ceramic body armour plate, subjected to single and multiple projectile impacts. Picture is adapted from [15].

1.1.1. EXPERIMENTS ON CERAMICS

To design and improve armour systems one needs to understand the physics of the problem as well as the behaviour of the materials involved. To study armour systems with ceramic materials, experiments may be performed. One way to test these armour systems is to simply subject it to the design threat. This can for instance be a 7.62x39mm bullet fired by an assault rifle, or the tungsten carbide core 7.62mm APM2 bullet fired from a sniper rifle [5]. Figure 1.1 shows how a ceramic body armour plate could respond to such threats. In this particular experiment the bullets are stopped, but the ceramic armour material has failed. Many more similar experimental results can be found in literature [6–14]. Tests such as these may prove the protective capabilities of the armour system, but may be less suitable to study the behaviour of an individual constituent. This is because armour systems typically consist of multiple layers of different materials. Ballistic tests can (and often will) therefore also be performed on the individual materials. By doing so the failure mechanisms of a material can be better understood, which may eventually lead to better armour designs.

The main goal of an armour system is obviously to slow down or even stop an incoming projectile. When a projectile strikes an armour system a number of failure mechanism are activated in both the projectile and target [16]. The ceramic material in such an armour system provides a hard surface, on which the projectile may deform plastically and even fracture. The ceramic material can also fail during this interaction. But as long as the ceramic material can still exert a force on the projectile it will still be slowed down and can be stopped. This is also why it is important to understand the failure mechanisms in the ceramic from initiation to full failure.

It is clear that the failure mechanisms of ceramic material under ballistic loading should be studied. Unfortunately, this is also where the difficulty lies. Ballistic tests will induce forces (far) beyond the ceramic material strength and the results are often catastrophic. Measuring the true ceramic behaviour during the experiment is impossible and since the ceramic is often pulverized, post-mortem analysis is also complicated. To move forward one must first identify the failure mechanisms present in a ceramic after ballistic loading. The second step is then to find a more controlled experiment which shows the same failure mechanisms, to be able to study these failure mechanisms in more detail.

From literature typical failure mechanisms in a ceramic armour under ballistic loading can be found. In the first phase of impact on a ceramic material there are two failure phenomena which occur. Just below the surface, directly underneath the projectile the ceramic material experiences high pressures and high shear stresses. In this zone microcracking and even plastic deformation of the ceramic material is possible when the confining pressures are sufficiently high [17–21]. This zone is often referred to as the quasi-plastic zone or Mescall zone. Just outside the contact area of the projectile tensile stresses are dominant. This leads to the formation of ring cracks at the ceramic surface. These ring cracks can develop into cone cracks, which may eventually grow through the thickness of the ceramic target. Depending on the impact conditions the ceramic cone may also fragment [7, 9, 12, 22]. This fragmented cone can still provide resistance to the projectile if sufficient confinement is provided by the adjacent material [23, 24]. The quasi-plastic zone and cone cracking already indicates the complexity in failure in ceramic under ballistic impact, since they are both present at the front face of the armour and can interact. There are however more failure mechanisms which can be present in a ceramic material under ballistic loading. A third type of failure is radial cracking, which may be visible at the target back side and can provide additional fragmentation to the ceramic target. The fourth failure mechanism is lateral cracking, which occurs when the projectile is reflected and the ceramic material unloads [25–28]. A schematic overview of the four failure mechanisms can also be found in Figure 1.2. The failure mechanisms described here are typical for ceramic under ballistic loading, but when and how they are present depends on many factors. These factors include the type/geometry of the ceramic material, the type/geometry/velocity/orientation of the projectile and boundary conditions. As a result the only way to study these failure mechanisms is in a controlled set-up.

Failure mechanisms, such as described above, can be observed in ceramic armour systems after impact. To study these failure mechanisms there is a need for simple, cheap experiments in a controlled set-up. Perhaps the most simple ballistic test on a ceramic is the so called “bare tile” testing [22]. In this type of test the ceramic alone is left to defeat the projectile, without any additional material layers in front or behind the ceramic. The advantage is that one can study the pure behaviour of the ceramic. However, the response in this test may be both different and weaker than when used in the armour system. In fact, full projectile impact on bare tiles often leads to catastrophic failure of the ceramic material, fully fragmenting the tile and preventing post-mortem analysis on the failure mechanisms. An alternative test which provide semi-infinite backing is the so called depth of penetration (DOP) test [29–32]. In this test a ceramic tile (or other material) is backed by a very large block of metal. Alternatively, one may use another elastic-plastic material as backing, but metal is most frequently used in DOP testing. A projectile may be stopped by the ceramic tile or is found to penetrate through the ce-

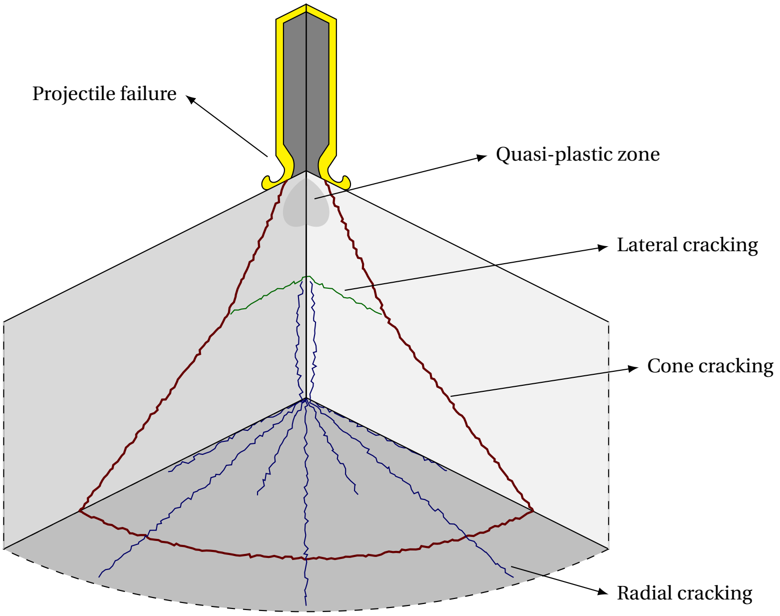

Figure 1.2: Schematic overview of failure mechanisms caused by impact on ceramic material.

ramic into the metal. The depth of penetration into the metal can be used as a comparative measurement of the ceramic's stopping power. Again, the boundary condition is not the same as an armour system and providing a new metal backing for each test is a costly endeavour.

When comparing the bare tile and DOP test the former may be preferred due to low cost and simplicity. But, as mentioned before, the impact event may be catastrophic for the ceramic material. To prevent catastrophic failure in the bare tile test one may use thick ceramic tiles or change the projectile. Figure 1.3 shows a 40mm thick silicon carbide ceramic after it has been impacted by a 7.62 APM2 projectile at a velocity of 830m/s. In this example the projectile was stopped and the failure of the ceramic can be clearly studied from the specimen after impact. The ceramic tile is however very thick and thus expensive, which would remove the argument that bare tile testing is low in cost. This is why bare tile tests are often performed with steel spherical projectiles, with lower impact velocities and weights than a 7.62 APM2 round. This allows for a less catastrophic failure of the ceramic material and tests can be performed on thinner tiles. Figure 1.4 shows the back face of two 12mm thick ceramic tiles after being impacted at 500m/s by a steel spherical projectile. It can be found that the main failure mechanisms are similar to the full scale projectile testing. This is why sphere impact tests on bare tiles are considered a good alternative, as this is a cheap, simple and reproducible test which can be performed on ceramic materials.

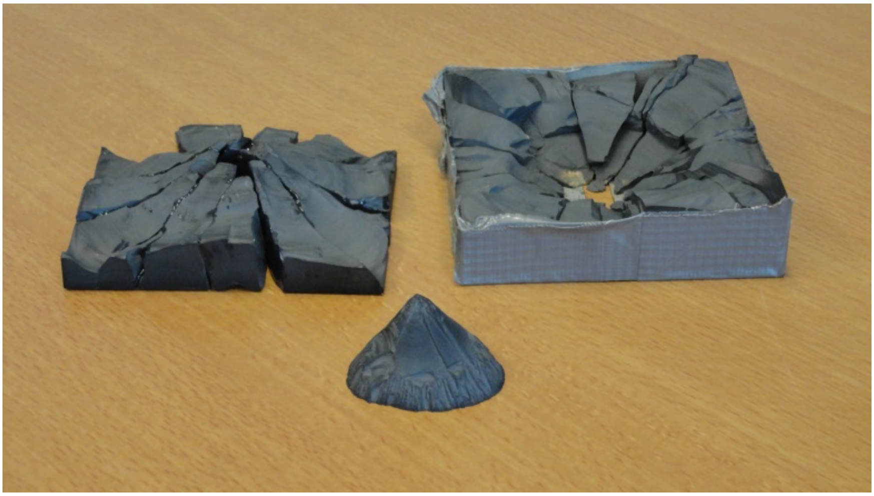

Figure 1.3: Silicon carbide ceramic tile, subjected to a single projectile impact. Cone cracking and radial cracking in the ceramic target is clearly visible. (E. Carton, TNO Laboratory for Ballistic Research, personal communication)

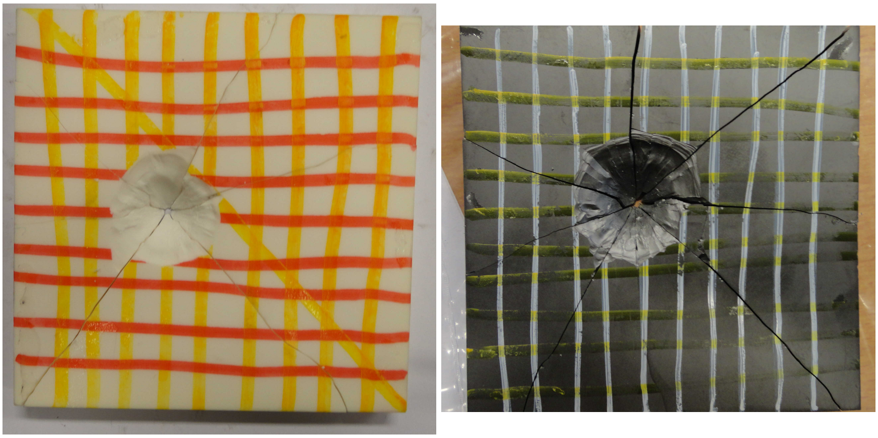

Figure 1.4: Ceramic tiles after "bare tile" testing, the back face is shown. Radial cracking is visible, as is the cone crack. (E. Carton, TNO Laboratory for Ballistic Research, personal communication)

1.1.2. SIMULATING IMPACT ON CERAMICS

In addition to performing experiments on ceramic armour one may perform numerical simulations. Simulating impact on ceramic materials can be a powerful tool to help understand the failure processes. If the models and methods are properly chosen the major benefit of simulations is that it allows the user to follow what happens during the interaction, at any given location. This can help explain why certain failure mechanisms form and possibly give insight in how to suppress them. Numerical simulation can also aid in the design of a ceramic armour system, as it allows the user to quickly and cheaply check a wide range of armour set-ups and material properties. There are many numerical methods which may be used, one of which is the Finite Element Method. This method will also be used in this thesis.

To study impact behaviour on a ceramic material through simulations requires a proper material model. The models by Johnson and Holmquist are often used to simulate armour ceramics. They proposed three versions of their model: JH1 [33], JH2 [34] and a model developed with Beissel which is also known as JHB [35]. Other ceramic material models can be used as well, such as the model by Simha [36] or the more general Kayenta model [37]. All these models are phenomenological softening plasticity models, with variations in their formulations of strength and failure. These phenomenological models do not describe the true microscopical failure mechanisms, but provide the response of the material given a loading condition. The advantage of these models is that they can easily capture the response, without having to know the true underlying material behaviour. Calibrating these models is generally easy, as standard macro-scale tests may be used. Another type of model exists which starts from a more theoretical approach for ceramic failure. Instead of only considering the response of a ceramic, these models may start from a micro-scale description of the material, such as micro-cracks or even dislocation movement. On a higher scale these mechanisms lead to plasticity and softening behaviour and global failure phenomena such as cone cracking or the quasi-plastic zone may be predicted. These models may be closer to reality, but they requires a thorough understanding of the micro-structural response. Furthermore, calibrating these models is more complex, as more detailed information on material is required e.g. micro-crack density. Examples of more theoretical models are the model by Rajendran and Grove [38], the dominant crack model by Zuo [39] or the models proposed by Deshpande and Evans [40, 41]. In the current thesis this second class of models will not be used. The focus lies on the phenomenological models, in particular the JH2 model. The JH2 ceramic material model is chosen as basis in this thesis because it is widely accepted, has simple formulations and was shown to correctly predict ceramic behaviour under impact conditions.

There are, unfortunately, some shortcomings of the JH2 model which will have to be solved before the sphere impact experiment can be simulated successfully. The first issue is that the JH2 model is a softening plasticity model, which is known to suffer from mesh dependency. This may cause spurious localization of failure as well as a bias of the failure to the mesh. This behaviour is highly unwanted if one requires an objective prediction of the failure mechanisms. Fortunately there are a few ways to provide regularization and remove this mesh dependency. These include non-local [42] or gradient [43] formulations as well as the addition of a rate dependency or viscosity [44–46]. The addition of a rate dependency to the material model is particularly interesting for the current armour application, since most materials have some rate dependency in material strength. In this thesis rate dependency will be used to provide both regularization and a physical rate dependency to the JH2 material model. This results in a numerically sound material model. The second shortcoming of the model lies in the description of failure. This has always been a difficult aspect of ceramic models, since direct measurement of ceramic failure under ballistic loading is currently not possible. Instead the failure behaviour is often found through inverse modelling, where a failure formulation is modified until simulation results match the experiments. Since the JH2 model is a softening plasticity model, the strength is reduced as plastic deformation grows. In the JH2 model the magnitude of strength reduction depends on the stress condition under which the plastic deformation occurred. This models the behaviour of ceramic, where failure under tension is very brittle and fast, but failure under compression may be more ductile and slow. In the JH2 model formulation this is however described through a single function, inadvertently coupling failure under tension and compression. Thus, although the JH2 model is widely accepted in ceramic modelling, the objectivity and failure description of this model should be improved.

1.2. OUTLINE OF THE THESIS

The final goal of the thesis work is to simulate sphere impact on ceramic material and use this to study failure of the ceramic material. In general, three steps are required before simulating failure of ceramic under impact loading. The first step is to have a numerically sound material model. Chapter 2 will discuss the addition of rate dependency on the hydrostatic tensile strength of the JH2 material model, which will ensure the results of the model to be objective with respect to the choice in spatial discretization. The second step in this thesis is to have a physically correct material model. Chapter 3 will use the previously developed viscosity regularized material model and check its validity under a wide range of loading conditions. Modifications to the failure formulation are proposed to be able to match all considered experiments. With this upgraded material model the third and final step of the thesis follows in Chapter 4. Here a 3d numerical framework is defined for sphere impact simulations, which is also validated through sphere impact experiments. The numerical framework is then used to study the failure process in a ceramic target under sphere impact. The thesis ends with concluding remarks on the research as well as recommendations for future research.

REFERENCES

[1] *armour,* `https://dictionary.cambridge.org/dictionary/english/armour`, accessed: 2019-02-18.

[2] S. Dunstan and R. Volstad, *Flak Jackets* (Osprey Publishing Ltd, London, 1984).

[3] P. J. Hazell, *Armour: Materials, Theory and Design* (CRC Press, Canberra, 2016).

[4] G. L. Rottman and S. Noon, *US Helicopter Pilot in Vietnam* (Osprey Publishing Ltd, Oxford, 2008).

[5] I. G. Crouch, *The Science of Armour Materials*, Woodhead Publishing in Materials (Woodhead Publishing, 2017).

[6] M. Mayseless, W. Goldsmith, S. Virostek, and S. Finnegan, *Impact on ceramic targets,* Journal of Applied Mechanics **54**, 373 (1987).

[7] R. O'Donnell, *An investigation of the fragmentation behaviour of impacted ceramics,* Journal of Materials Science Letters **10**, 685 (1991).

[8] C. E. Anderson and B. L. Morris, *The ballistic performance of confined Al2O3 ceramic tiles,* International Journal of Impact Engineering **12**, 167 (1992).

[9] R. Woodward, W. G. Jr, R. O'Donnell, W. Perciballi, B. Baxter, and S. Pattie, *A study of fragmentation in the ballistic impact of ceramics,* International Journal of Impact Engineering **15**, 605 (1994).

[10] D. Sherman, *Impact failure mechanisms in alumina tiles on finite thickness support and the effect of confinement,* International Journal of Impact Engineering **24**, 313 (2000).

[11] D. Gonc, F. de Melo, A. Klein, and H. Al-qureshi, *Analysis and investigation of ballistic impact on ceramic / metal composite armour,* Machine Tools & Manufacture **44**, 307 (2004).

[12] E. Medvedovski, *Ballistic performance of armour ceramics : Influence of design and structure . Part 1,* Ceramics International **36**, 2103 (2010).

[13] I. G. Crouch, G. Appleby-Thomas, and P. J. Hazell, *A study of the penetration behaviour of mild-steel-cored ammunition against boron carbide ceramic armours,* International Journal of Impact Engineering **80**, 203 (2015).

[14] D. B. Rahbek, J. W. Simons, B. B. Johnsen, T. Kobayashi, and D. a. Shockey, *Effect of composite covering on ballistic fracture damage development in ceramic plates,* International Journal of Impact Engineering **99**, 58 (2017).

[15] I. Crouch, *Effects of cladding ceramic and its influence on ballistic,* in *28th International Symposium on Ballistics* (2014) pp. 1084–1094.

[16] M. L. Wilkins, C. Cline, and C. Honodel, *Fourth Progress Report of Light Armour Program,* Tech. Rep. (Lawrence Radiation Laboratory, University of California, Livermore, 1969).

[17] J. Cagnoux and F. Longy, *Spallation and shock-wave behaviour of some ceramics,* Le Journal de Physique Colloques **49**, C3 (1988).

[18] J. Lankford, C. A. Jr, A. Nagy, J. Walker, and A. Nicholls, *Inelastic response of confined aluminium oxide under dynamic loading conditions,* Journal of Materials Science **33**, 1619 (1998).

[19] S. Acharya, S. Bysakh, V. Parameswaran, and A. Kumar Mukhopadhyay, *Deformation and failure of alumina under high strain rate compressive loading,* Ceramics International **41**, 6793 (2015).

[20] J. Wade, S. Robertson, and H. Wu, *Plastic deformation of polycrystalline alumina introduced by scaled-down drop-weight impacts,* Materials Letters **175**, 143 (2016).

[21] M. Bhattacharya, S. Dalui, N. Dey, S. Bysakh, J. Ghosh, and A. K. Mukhopadhyay, *Low strain rate compressive failure mechanism of coarse grain alumina,* Ceramics International **42**, 9875 (2016).

[22] E. Carton and G. Roebroeks, *Testing Method for Ceramic Armor and Bare Ceramic Tiles,* Advances in Ceramic Armor X , 1 (2015).

[23] I. Horsfall, M. Edwards, and M. Hallas, *Ballistic and physical properties of highly fractured alumina,* Advances in Applied Ceramics **109**, 498 (2010).

[24] P. J. Hazell, G. J. Appleby-Thomas, and S. Toone, *Ballistic compaction of a confined ceramic powder by a non-deforming projectile: Experiments and simulations,* Materials and Design **56**, 943 (2014).

[25] M. V. Swain and J. T. Hagan, *Indentation plasticity and the ensuing fracture of glass,* Journal of Physics D: Applied Physics **9**, 2201 (1976).

[26] B. M. Liaw, a. S. Kobayashi, and a. F. Emery, *Theoretical Model of Impact Damage in Structural Ceramics,* Journal of the American Ceramic Society **67**, 544 (1984).

[27] X. Chen, J. W. Hutchinson, and A. G. Evans, *The mechanics of indentation induced lateral cracking,* Journal of the American Ceramic Society **88**, 1233 (2005).

[28] A. Yonezu, B. Xu, and X. Chen, *Indentation induced lateral crack in ceramics with surface hardening,* Materials Science and Engineering A **507**, 226 (2009).

[29] P. J. Hazell, *Measuring the strength of brittle materials by depth-of-penetration testing,* Advances in Applied Ceramics **109**, 504 (2010).

[30] P. J. Hazell, T. Lawrence, and C. Stennett, *The Defeat of Shaped Charge Jets by Explosively Driven Ceramic and Glass Plates,* International Journal of Applied Ceramic Technology **9**, 382 (2012).

[31] S. Savio, V. Madhu, and A. Gogia, *Ballistic performance of alumina and Zirconia-toughened alumina against 7.62 armour piercing projectile,* Defence Science Journal **64**, 477 (2014).

[32] A. Krell and E. Strassburger, *Order of influences on the ballistic resistance of armor ceramics and single crystals,* Materials Science and Engineering A **597**, 422 (2014).

[33] G. R. Johnson and T. J. Holmquist, *A Computational Constitutive Model for Brittle Materials Subjected to Large Strains, High Strain Rates and High Pressures,* in *Proceedings of the EXPLOMET Conference* (San Diego, 1990).

[34] G. R. Johnson and T. J. Holmquist, *An improved computational constitutive model for brittle materials,* AIP Conference Proceedings **309**, 981 (1994).

[35] G. R. Johnson, T. J. Holmquist, and S. R. Beissel, *Response of aluminum nitride (including a phase change) to large strains, high strain rates, and high pressures,* Journal of Applied Physics **94**, 1639 (2003).

[36] C. Simha, *Arbor Ciencia Pensamiento Y Cultura*, Ph.D. thesis, University of Texas (1999).

[37] R. Brannon, A. Fossum, and O. Strack, *Kayenta: theory and user's guide*, Tech. Rep. March (Sandia National Laboratories, Albuquerque, 2009).

[38] A. Rajendran, *High Strain Rate Behavior of Metals Ceramics, and Concrete*, Tech. Rep. (University of Dayton Research Institute, Dayton, Ohio, 1992).

[39] Q. Zuo, F. Addessio, J. Dienes, and M. Lewis, *A rate-dependent damage model for brittle materials based on the dominant crack,* International Journal of Solids and Structures **43**, 3350 (2006).

[40] V. S. Deshpande and A. G. Evans, *Inelastic deformation and energy dissipation in ceramics: A mechanism-based constitutive model,* Journal of the Mechanics and Physics of Solids **56**, 3077 (2008).

[41] V. S. Deshpande, E. A. N. Gamble, B. G. Compton, R. M. McMeeking, A. G. Evans, and F. W. Zok, *A Constitutive Description of the Inelastic Response of Ceramics,* Journal of the American Ceramic Society **94**, s204 (2011).

[42] Z. P. Bazant and F.-B. Lin, *Non-local yield limit degradation,* International Journal for Numerical Methods in Engineering **26**, 1805 (1988).

[43] N. Fleck and J. Hutchinson, *Strain Gradient Plasticity,* (1997).

[44] A. Needleman, *Material rate dependence and mesh sensitivity in localization problems,* Computer Methods in Applied Mechanics and Engineering **67**, 69 (1988).

[45] A. Winnicki, C. J. Pearce, and N. Bićanić, *Viscoplastic Hoffman consistency model for concrete,* Computers and Structures **79**, 7 (2001).

[46] M. Lazari, L. Sanavia, and B. Schrefler, *Local and non-local elasto-viscoplasticity in strain localization analysis of multiphase geomaterials,* International Journal for Numerical and Analytical Methods in Geomechanics **39**, 1570 (2015), arXiv:nag.2347 [10.1002] .

2

A VISCOSITY REGULARIZED PLASTICITY MODEL FOR CERAMICS

2.1. INTRODUCTION

Ceramic materials are frequently used in armour systems. Their high hardness and relative light weight make ceramics an ideal candidate for armour systems. Upon impact a projectile can deform heavily and may even fracture [2–4]. Directly underneath the projectile a zone of high compression and shear occurs. In this zone the ceramic may experience micro-cracking and crystal plasticity up to the point of full fragmentation. This zone is referred to as the ’comminuted’ or ’quasi-plastic’ zone, which can posses a considerable residual strength [5]. Some distance away from the projectile impact location the pressure drops and tensile states may be found at the ceramic surface. Ring cracks can be initiated, which may develop into cone cracks. These cone cracks form one of the main contributions to failure of ceramic armour. As a cone crack grows and reaches the back side of the armour, a plug is formed and the material has effectively lost its strength. Understanding the location and direction of these cone cracks is of great importance in armour design. Many experiments have been conducted to study these cone cracks in armour ceramics, both under dynamic [6–11] and quasi-static loading [12–14].

To predict ceramic armour behaviour many material models have been developed over the years. Well known and often used material models are the phenomenological models by Johnson and Holmquist, who proposed three models: JH1 [15], JH2 [16] and JHB [17]. Another phenomenological model was proposed by Simha [18]. Other ceramic models are those by Rajendran and Grove [19], the dominant crack model by Zuo [20] and two models by Deshpande and Evans [21, 22]. This latter group of models is more theoretical and physical based than the first four phenomenological models. Although the latter group is appealing from a theoretical perspective in the current chapter the

---

This chapter is based on [1]

JH2 model is used. This model is often used, simple in its formulation and is shown to correctly predict ceramic behaviour for a wide range of tests.

The ceramic models by Johnson and Holmquist are pressure dependent softening plasticity models. It is well known that softening plasticity models suffer from mesh dependency and the models by Johnson-Holmquist pose no exception. As a result these models may lead to spurious localization and a bias with respect to the discretization (i.e. mesh) when used in a finite element framework. Model results will not be objective with respect to the discretization and vital failure mechanisms such as cone cracks may not be predicted correctly. This is detrimental for the predictive capabilities of these models with respect to armour performance.

To find objective results with respect to the discretization some form of regularization is required. Many methods have been described in literature which can regularize the results from softening plasticity models. Most methods regularize a solution by the introduction of a length scale This can be through the introduction of a specific type of non-local integral formulation [23] or a gradient formulation [24] in the evolution equation for plasticity. It is possible to provide regularization without directly introducing an explicit length scale in the material model. Introducing a rate dependency or viscosity can also provide regularization [25–27].

Simple and often used visco-plasticity formulations are those by Perzyna [28], Duvaut-Lions [29] and Wang [30]. The models by Perzyna and Duvaut-Lions are based on overstress, which means that stress states outside the yield surface are allowed. The method by Wang is the so-called consistency formulation. In this formulation the yield surface is rate dependent and stress states are always inside or on the yield surface. For the Perzyna and Duvaut-Lions formulation the traditional Kuhn-Tucker loading conditions do not apply. However, for the consistency formulation one can still use the Kuhn-Tucker loading conditions.

For the Perzyna model it was recognized that the model may not converge to regular plasticity if multi-surface plasticity is used [31]. The Duvaut-Lions model does not have this problem and is therefore often used in literature. However, it can easily be shown that the model is unsuited to predict a full loss of deviatoric strength. This is because the model requires a converged inviscid solution, which is the so called backbone stress or strength. The viscous stress state is an interpolated value between the backbone and the trial stress state. For a non-zero deviatoric trial stress this will always lead to non-zero viscous stresses, even for a fully failed backbone material.

In the current thesis a consistency formulation is used to regularize the JH2 material model with viscosity. Existing mesh dependency problems for the JH2 model will be illustrated using a tapered bar and a direct shear test. The original rate dependency of the JH2 model will be shown to be insufficient to provide regularization. A viscosity is proposed on the apex pressure (e.g. hydrostatic tensile strength) of the JH2 model. First a linear formulation is adopted for the apex viscosity. This is shown to regularize the solution of the tapered bar and the direct shear test. For high loading rates a linear viscosity may lead to an unrealistic failure zone size. An alternative mixed linear/logarithmic apex formulation is introduced. This mixed formulation is found to limit the failure zone size while still providing mesh independent results. The mixed linear/logarithmic viscosity is formulated such that a linear viscosity can be retrieved. The chapter will end by showing how the spall strength varies as a function of loading rate in the original and proposed mixed linear/logarithmic viscosity formulation . It will be shown that the JH2 model with the proposed apex viscosity can correctly capture the rate dependent strength found in experiments, while the original model can not.

2.2. METHODS AND MODELS

To simulate ceramic behaviour the finite element method (FEM) is used. The FEM and required material models are implemented using the C++ based libraries from the open source package JemJive version 2.2 [32]. JemJive provides a FEM framework which supports both quasi-static and dynamic solution procedures in the form of a Newton-Raphson and Newmark solution scheme. The material models used to simulate ceramic behaviour are explained in the following subsections.

2.2.1. MATERIAL MODELS

ORIGINAL MODEL

The Johnson-Holmquist-2 (JH2) material model is a pressure dependent softening plasticity model. For a general softening plasticity model the yield function can be represented as a function $f(\boldsymbol{\sigma},\boldsymbol{\kappa})$, where $\boldsymbol{\sigma}$ is the stress tensor and $\boldsymbol{\kappa}$ a collection of internal variables. In the JH2 model only a single scalar damage variable $D \in [0..1]$ is used as internal variable. The yield function for the JH2 model can thus be written as

$$f(\boldsymbol{\sigma},D) = \sigma_{eq}(\boldsymbol{\sigma}) - \sigma_y(\boldsymbol{\sigma},D). \tag{2.1}$$

The Von Mises equivalent stress $\sigma_{eq}(\boldsymbol{\sigma}) = \sqrt{{}^3/{}_2\boldsymbol{s}:\boldsymbol{s}}$ is used, were $\boldsymbol{s} = \boldsymbol{\sigma} - \boldsymbol{\sigma}_{hyd}$ is the deviatoric stress tensor found by subtracting the hydrostatic stress component $\boldsymbol{\sigma}_{hyd}$ from the stress tensor $\boldsymbol{\sigma}$. The yield stress σ_y for JH2 model is defined as

$$\sigma_y^*(\boldsymbol{\sigma},D) = (1-D)\ \sigma_i^*(\boldsymbol{\sigma}) + D\,\sigma_f^*(\boldsymbol{\sigma}). \tag{2.2}$$

Here the superscript * indicates that the stress values are normalized with respect to the Hugoniot elastic limit σ_{HEL}. The subscripts i and f relate to the intact and failed (i.e. residual) material strengths

$$\sigma_i^*(\boldsymbol{\sigma}) = A\left(\frac{T+p(\boldsymbol{\sigma})}{P_{HEL}}\right)^n \left(1+C\ln\dot{\bar{\epsilon}}_p^*\right), \tag{2.3}$$

$$\sigma_f^*(\boldsymbol{\sigma}) = B\left(\frac{p(\boldsymbol{\sigma})}{P_{HEL}}\right)^m \left(1+C\ln\dot{\bar{\epsilon}}_p^*\right). \tag{2.4}$$

Here the material strength can be found as a function of the pressure $p(\boldsymbol{\sigma}) = -\boldsymbol{\sigma}_{hyd} = -{}^1/{}_3\boldsymbol{\sigma}:\boldsymbol{I}$. The material's rate dependency can be scaled through parameter C, while a normalized equivalent plastic strain rate $\dot{\bar{\epsilon}}_p^* = \dot{\bar{\epsilon}}_p/\dot{\bar{\epsilon}}_p^0$ is used in the logarithmic formulation. For strain rates below the reference rate there is no rate effect (i.e. $C = 0.0$). Other model parameters are the reference strain rate $\dot{\bar{\epsilon}}_p^0$ and strength parameters A, B, n, m, P_{HEL} and T. The equivalent plastic strain rate is defined as

$$\dot{\bar{\epsilon}}_p = \sqrt{\frac{2}{3}\dot{\boldsymbol{e}}_p:\dot{\boldsymbol{e}}_p}, \tag{2.5}$$

where $\dot{\boldsymbol{e}}_p$ is the deviatoric plastic strain rate. From this equivalent plastic strain rate the rate of damage in the material can be found as

$$\dot{D} = \frac{\dot{\bar{\epsilon}}_p}{\bar{\epsilon}_p^{max}(\boldsymbol{\sigma})}, \tag{2.6}$$

where $\bar{\epsilon}_p^{max}(\boldsymbol{\sigma})$ is the maximum equivalent plastic strain for the given stress state. For pressures below the hydrostatic tensile strength T there is no gradual failure and full failure with $D = 1.0$ is immediately reached. For the Johnson-Holmquist models $\bar{\epsilon}_p^{max}$ is computed as

$$\bar{\epsilon}_p^{max}(\boldsymbol{\sigma}) = d_1 \left(\frac{T + p(\boldsymbol{\sigma})}{P_{HEL}} \right)^{d_2}. \tag{2.7}$$

Here d_1 and d_2 are material parameters. Plastic deformation is obtained through the flow rule

$$\dot{\boldsymbol{\epsilon}}_p = \dot{\lambda}\, \partial g / \partial \boldsymbol{\sigma}, \tag{2.8}$$

where the JH2 model uses a plastic potential function

$$g = \sigma_{eq}(\boldsymbol{\sigma}) = \sqrt{\frac{3}{2}\boldsymbol{s} : \boldsymbol{s}}. \tag{2.9}$$

Two observations can be made on this plastic potential function. First, it can be shown that the volumetric plastic deformation $\epsilon_{V,p} = 0$, which implies isochoric plastic flow. Second, it can be shown that $\dot{\bar{\epsilon}}_p = \dot{\lambda}$.

Inelastic volumetric response is included in the JH2 model through a bulking contribution Δp to the pressure. This bulking formulation is explicit in nature, resulting in step size dependence. In the current chapter bulking is not included.

PROPOSED MODEL

Viscosity (i.e. rate dependency) can be used to regularize the finite element solution. The standard JH2 model has a rate dependency (viscosity) included in its formulation (see equations (2.3) and (2.4)). However, it will be shown in this chapter that the standard rate dependency in the JH2 model is insufficient to provide satisfactory regularization.

A new rate dependency is proposed for the JH2 model. The proposed model will be referred to as the viscosity regularized JH2 model (JH2-V). The material strengths are reformulated from (2.3) and (2.4) to

$$\sigma_i^* = A \left(\frac{T(\dot{\bar{\epsilon}}_p) + p(\boldsymbol{\sigma})}{P_{HEL}} \right)^n, \tag{2.10}$$

$$\sigma_f^* = B \left(\frac{p(\boldsymbol{\sigma})}{P_{HEL}} \right)^m. \tag{2.11}$$

In this formulation the equivalent plastic strain rate $\dot{\bar{\epsilon}}_p$ is used to scale the material's ultimate tensile limit T of the intact material strength. Note that the original logarithmic scaling $(1 + C \ln \dot{\bar{\epsilon}}_p^*)$ from equations (2.3) and (2.4) is absent in this proposed formulation. The proposed scaling of the ultimate tensile limit does not exclude the original rate dependency, both formulations may be used simultaneously. However, in the current chapter the original JH2 rate dependency and the proposed rate dependency on the ultimate tensile limit will not be used simultaneously in order to study their effects independently.

In the consistency formulation a yield function $f(\boldsymbol{\sigma}, \boldsymbol{\kappa}, \dot{\boldsymbol{\kappa}})$ can be defined. Here $\dot{\boldsymbol{\kappa}}$ is the rate of some internal variables. In the proposed material model only the rate of a single internal variable $\dot{\kappa}$ is used. Here $\dot{\kappa} = \dot{\bar{\epsilon}}_p = \dot{\lambda}$, which is the rate of the plastic multiplier. Using the consistency formulation function (2.1) can now be written as

$$f_{rd}(\boldsymbol{\sigma}, D, \dot{\lambda}) = \sigma_{eq}(\boldsymbol{\sigma}) - \sigma_y(\boldsymbol{\sigma}, D, \dot{\lambda}), \tag{2.12}$$

which will be referred to as the rate dependent yield function. This is in accordance with the consistency model and the Kuhn-Tucker loading conditions

$$f_{rd} \leq 0, \qquad \dot{\lambda} \geq 0, \qquad \dot{\lambda} \cdot f_{rd} = 0 \tag{2.13}$$

still apply.

The rate dependency of the ultimate tensile pressure is initially assumed in a linear form

$$T(\dot{\bar{\epsilon}}_p) = T(\dot{\lambda}) = T_0 + \eta\dot{\lambda}, \tag{2.14}$$

where η is the viscosity and T_0 the original rate independent strength parameter. The current viscosity is proposed to provide regularization. The initial choice for a linear rate dependency will be critically reviewed in section 2.5. Recent experimental work indicates that there is also a physical component to this rate effect on the tensile strength of ceramics [33] [34]. It will also be investigated in section 2.5 how the proposed rate dependency affects the predicted tensile strength.

The original and the proposed rate dependencies are visualized in Figure 2.1. It is clear from Figure 2.1a that the original rate dependency provides a deviatoric scaling of the material strength. The apex point T is left unaltered by the original rate dependency. From Figure 2.1b it may be observed that the proposed rate dependency provides a hydrostatic shift of the yield function with the loading rate. It is important to note the effect of both rate dependencies over the range of pressures. For the original rate dependency the absolute strength increase is found to be largest for higher pressures. For the proposed rate dependency the opposite holds true, as the largest absolute strength increase is found at the original apex point T.

Other types of rate dependency may be obtained by performing a similar scaling on different model parameters. Although this may work for the other JH material models it will not work for the JH2 model. This is due to the singularity at the apex. Scaling for instance A with rate will only provide a deviatoric scaling and will not give the desired increase in strength under tension. The proposed formulation on the apex pressure is however more general and a similar approach can also be used for the other JH models.

2.3. ALGORITHMIC ASPECTS

For plasticity models the (infinitesimal) strain rate can be split into an elastic and plastic component

$$\dot{\boldsymbol{\epsilon}} = \dot{\boldsymbol{\epsilon}}_e + \dot{\boldsymbol{\epsilon}}_p. \tag{2.15}$$

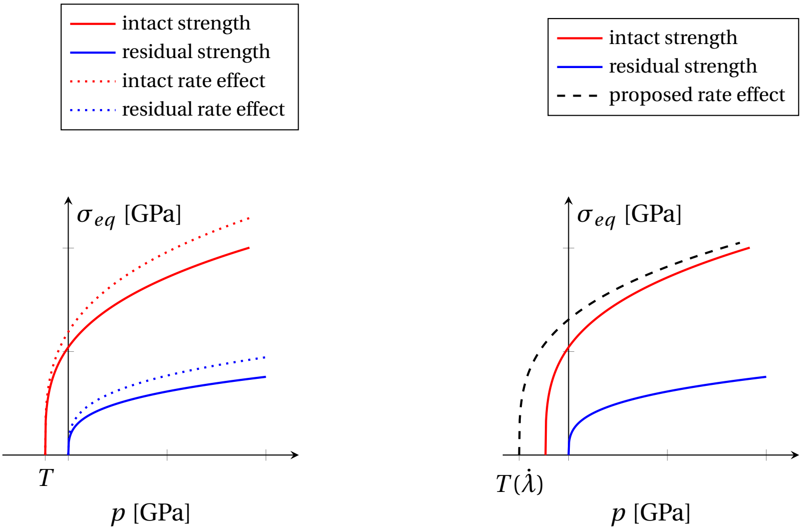

(a) Original rate effect

(b) Proposed rate effect

Figure 2.1: Deviatoric strength σ_{eq} of the Johnson-Holmquist-2 material model plotted as function of pressure p. Figures show the original and proposed rate effects. Note the relatively large increase in strength under tension and the minimal increase under compression for the proposed model.

The stress rate is expressed as

$$\dot{\boldsymbol{\sigma}} = \boldsymbol{D}_e : \dot{\boldsymbol{\epsilon}}_e = \boldsymbol{D}_e : \left(\dot{\boldsymbol{\epsilon}} - \dot{\boldsymbol{\epsilon}}_p\right), \tag{2.16}$$

where the elastic stiffness tensor $\boldsymbol{D}_e$ is used. Application of the flow rule (2.8) results in

$$\dot{\boldsymbol{\sigma}} = \boldsymbol{D}^e : \left(\dot{\boldsymbol{\epsilon}} - \dot{\lambda}\frac{\partial g}{\partial \boldsymbol{\sigma}}\right) = \boldsymbol{D}^e : \left(\dot{\boldsymbol{\epsilon}} - \dot{\lambda}\boldsymbol{m}\right). \tag{2.17}$$

In this formulation $\dot{\lambda}$ is the rate of plastic multiplier, while $\boldsymbol{m} = \partial g / \partial \boldsymbol{\sigma}$ is the flow direction with the plastic potential function g. In the current chapter the plastic potential function from (2.9) is used where g is only a function of deviatoric stress. It is also possible to define a plastic potential function which depends on the full stress tensor, which includes a hydrostatic component. One may, for instance, use associative plasticity ($g = f$), which introduces volumetric inelastic deformation [35].

Rate equations cannot be used directly in the discrete formulation of the finite element method. The relations above can be written in incremental form, where the stress increment reads

$$\Delta\boldsymbol{\sigma} = \boldsymbol{D}^e : (\Delta\boldsymbol{\epsilon} - \Delta\lambda\boldsymbol{m}). \tag{2.18}$$

A new stress can now be found as

$$\begin{aligned}\boldsymbol{\sigma}^{n+1} &= \boldsymbol{\sigma}^{n} + \Delta\boldsymbol{\sigma}, \\ &= \boldsymbol{D}^{e} : \left(\boldsymbol{\epsilon}^{n} - \boldsymbol{\epsilon}_{p}^{n}\right) + \boldsymbol{D}^{e} : (\Delta\boldsymbol{\epsilon} - \Delta\lambda \boldsymbol{m}), \\ &= \boldsymbol{D}^{e} : \left(\boldsymbol{\epsilon}^{n+1} - \boldsymbol{\epsilon}_{p}^{n} - \Delta\lambda \boldsymbol{m}\right). \end{aligned} \tag{2.19}$$

Here n and $n+1$ refer to the previous and current load increment. The unknowns in this incremental form are: the new stress $\boldsymbol{\sigma}^{n+1}$ and the increment of plastic multiplier $\Delta\lambda$. For simple plasticity models a closed form solution to this plastic multiplier is known and it can be computed directly from the given strain increment. For more complex plasticity formulations which include non-linearities, such as the JH2 model, a close form expression usually does not exist. For these cases an iterative scheme can be used at integration point level to find the correct stress and plastic multiplier. In the current thesis an Euler backward formulation is used [36].

2.3.1. PLASTICITY OR ELASTICITY

When a new global load increment is performed the new stress and internal states have to be determined at integration point level. For an integration point a trial stress state is computed under the assumption of elastic loading ($\Delta\lambda = 0$). From (2.19) this trial state can be computed as

$$\boldsymbol{\sigma}^{tr} = \boldsymbol{D}^{e} : \left(\boldsymbol{\epsilon}^{n+1} - \boldsymbol{\epsilon}_{p}^{n}\right). \tag{2.20}$$

Using this trial stress the yield function from (2.12) can be evaluated. A yield function $f_{rd} < 0$ results in elastic deformation of the material, while $f_{rd} \geq 0$ will result in plastic deformation. For the consistency model the initial check for plasticity is based on $f_{rd}(\boldsymbol{\sigma}^{tr}, D^{n}, 0.0)$. Here D^{n} is the final damage predicted by the previous load increment and an initial rate $\dot{\lambda} = 0.0$ is assumed. This is in line with the assumption of an elastic trial step (i.e. $\Delta\lambda = 0$).

For plastic deformation in the JH2 material model there are two domains in the stress space of interest, each with a specific algorithmic treatment. The first domain is where the trial stress can be returned to the yield surface in the flow direction $\partial g/\partial\boldsymbol{\sigma}$. In this stress domain the Euler backward return mapping scheme can be used to find the new stress state $\boldsymbol{\sigma}^{n+1}$ and increment in plastic multiplier $\Delta\lambda$. The second stress domain is where the trial stress can not be returned to the yield surface in the flow direction $\partial g/\partial\boldsymbol{\sigma}$. For the JH2 model with plastic potential (2.9) this includes all states with $p^{tr} < T$. Once the material is fully failed (i.e. $D = 1$) the apex point shifts to a zero pressure and the check becomes $p^{tr} < 0$. To find an admissible stress for this second group of trial states requires the use of a so-called apex return. The three domains in the stress space (two plastic and one elastic) are also visualized in Figure 2.2, where the blue domain indicates regular return, the red domain apex return and the green domain indicates an elastic state.

The proposed check for apex return has some limitations. The check only works for a pure deviatoric flow rule where it is known that $p^{tr} = p^{n+1}$. If volumetric plastic deformation would be included through the plastic potential function $p^{tr} \neq p^{n+1}$, which means the check $p^{tr} < T$ is no longer conclusive for apex return. Also if the material

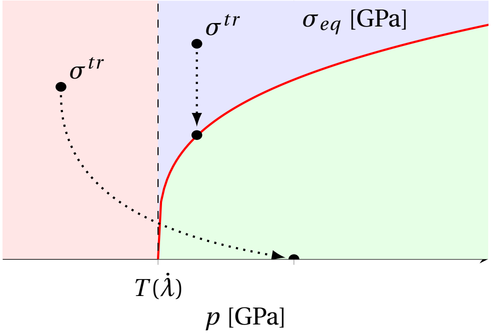

Figure 2.2: Return mapping for the JH2 model visualized. Any trial state in the green stress space remains elastic, in the blue stress space regular return mapping is applied while the red domain requires apex return.

reaches full damage (i.e. $D = 1$), the apex pressure reduces to zero and the check $p^{tr} < T$ is no longer valid. Finally, if rate dependency is considered on the apex also a different check is required, since the trial rate was assumed to be zero and $T(0.0) \neq T(\dot{\lambda}^{n+1})$ for any $\dot{\lambda}^{n+1} > 0$.

A more robust approach is to assume regular return mapping and check for a violation of the apex criterion $p^{n+1} < T(\dot{\lambda}^{n+1})$ in every Euler backward iteration. If the apex criterion is violated, a switch to apex return is necessary. This algorithmic treatment is shown in Box 1. The exact formulation of the apex return scheme is discussed in 2.3.3.

2.3.2. REGULAR RETURN ALGORITHM

An Euler backward scheme is used for the regular return mapping algorithm. For a visco-plastic model in the consistency formulation this can be used to find a solution of (2.19). The derivation and formulation of an Euler backward scheme for such a model has already been discussed in literature [30], it will therefore not be repeated in the current thesis.

2.3.3. APEX RETURN ALGORITHM

When the apex check is violated regular return mapping can no longer be applied. This can be found from (2.9), which shows the original JH2 model only allows deviatoric plastic strain. Therefore the plastic flow cannot result in an increase of pressure and a point inside the yield surface is never reached. Full failure is immediately applied (i.e. $D = 1$) and the stress is mapped to the apex of the residual strength curve at $p = 0$. The new stress state will be

$$\boldsymbol{\sigma}^{n+1} = \mathbf{0}. \tag{2.21}$$

The consistent tangent for this returned stress is easy to compute as

$$\boldsymbol{D}^{vp} = \mathbf{0}. \tag{2.22}$$

Finally, the plastic deformation under apex return has to be assigned. It was already mentioned that the JH2 model only predicts pure deviatoric plastic flow. For a fully failed

```
compute $\epsilon^{n+1}$ from $\boldsymbol{u}^{n+1}$
compute $\boldsymbol{\sigma}^{tr}$
initialize $D^{n+1} = D^n$ and $\dot{\lambda}^{n+1} = 0.0$
if $f_{rd}(\boldsymbol{\sigma}^{tr}, D^{n+1}, \dot{\lambda}^{n+1}) \geq 0$
PLASTIC DEFORMATION:
    1. start with:
       → REGULAR RETURN MAPPING
    2. if $p^{n+1} < T(\dot{\lambda}^{n+1})$ or $(p^{n+1} < 0$ and $D^{n+1} = 1)$:
       → APEX RETURN
else
ELASTIC DEFORMATION:
    1. $\boldsymbol{\sigma}^{n+1} = \boldsymbol{\sigma}^{tr}$
```

Box 1: Elastic or plastic loading

Table 2.1: All shared material properties for the JH2-ri, JH2-rd and JH2-V model.

variable	value	unit	variable	value	unit	variable	value	unit
E	375.0	GPa	T	0.2	GPa	d_1	0.05	-
ν	0.0	-	n	0.6	-	d_2	0.0	-
ρ	3700	kg/m^3	m	0.6	-			
A	0.930	GPa	P_{HEL}	0.1250	GPa			
B	0.310	GPa	σ_{HEL}	0.3746	GPa			

material under tension no deviatoric strength is present. From (2.19) it can be found that zero deviatoric stress is predicted if

$$\Delta\boldsymbol{\epsilon}_p = \boldsymbol{e}_e^{n+1}. \tag{2.23}$$

This reduces the deviatoric stress to zero and also satisfies the purely deviatoric flow rule for the JH2 model.

2.4. RESULTS

The material models presented in section 2.2.1 are used to simulation a number of test cases. Each test case will be simulated using the JH2 model with $C = 0.0$ (JH2-ri), the JH2 model with $C = 0.025$ and $\dot{\epsilon}_p^0 = 1\text{s}^{-1}$ (JH2-rd) and the viscosity regularized JH2 model (JH2-V). Other material properties are shown in Table 2.1. The values of P_{HEL} and σ_{HEL} are obtained by choosing $\mu_{HEL} = 0.001$. Note that by choosing $d_2 = 0.0$ the failure strain becomes independent of pressure. This ensures a finite rate of damage in the JH2-V model for pressures below the static apex pressure T.

The aim of the simulations in the current section is threefold. First, the simulations will show mesh dependency for the JH2 model. Second, the results show that the JH2-rd model has regularizing properties but these are insufficient for some loading cases. Third, the JH2-V model is shown to properly regularize the simulation results for all reviewed loading cases.

2.4.1. UNIT TEST

Mesh-dependency is a result of the loss of ellipticity of the boundary value problem in static analyses [37]. It can be shown mathematically when this loss of ellipticity occurs. An acoustic tensor is defined as

$$\boldsymbol{A} = \boldsymbol{n} \cdot \boldsymbol{D}^{vp} \cdot \boldsymbol{n}, \tag{2.24}$$

where $\boldsymbol{n}$ is a normal vector to a (localized) failure surface and $\boldsymbol{D}^{vp}$ the (visco)plastic tangent matrix. Loss of ellipticity occurs if

$$\det(\boldsymbol{A}) \leq 0, \tag{2.25}$$

for any or some $\boldsymbol{n}$. The current chapter will not provide proof for the loss of ellipticity in the JH2 model nor for the sustained ellipticity in the JH2-V model. Instead a numerical investigation with single element tests is adopted.

A single Q4 plane strain element with a single Gauss integration point is subjected to pure shear or pure uniaxial tensile deformation. The deformation is incrementally increased to allow for plastic deformation of the material and possibly invoking apex return. For each load increment in which the integration point experiences plastic deformation the visco-plastic tangent matrix is stored. Assuming a normal vector $\boldsymbol{n}$ in the plane of the element with an in-plane orientation varying from $\phi = 0°,\ 1°, .. \ 180°$ the acoustic tensor can be computed for each direction. During plastic deformation one or more directions may show a negative determinant, indicating loss of ellipticity. Note that for apex return (2.22) holds, thus $\det(\boldsymbol{A}) = 0$ and the material will lose ellipticity.

Figure 2.3 shows the minimum values for the determinant of the acoustic tensor found during unit testing. The vertical axes show the values of the determinant normalized with respect to the determinant of the elastic acoustic tensor. Figure 2.3a shows the results for the shear test. The horizontal axis represents the increments from start of plastic deformation to the end of the simulation, full failure (i.e. $D = 1.0$) was not reached during this shear test. The JH2-ri model shows a negative determinant for all plastic load steps. This was to be expected as softening plasticity models are known to lead to loss of ellipticity. The addition of a rate dependency either in form of JH2-rd or JH2-V model regularizes the model and ensures a positive determinant of the acoustic tensor. Figure 2.3b presents the unit test results under tension. Again the horizontal axis represents the increments during the simulation, this time from the start of plasticity to the step just before apex return. These results show that both the JH2-ri and JH2-rd models lose ellipticity during loading. For the JH2-V model ellipticity is maintained during plastic deformation.

The unit test shows that the JH2-rd model can provide regularization, but not for all loading cases. The JH2-V model does provide regularization under the investigated loading scenarios. In the next subsections the mesh-dependency resulting from the loss of ellipticity will be shown. Initial results focus on spurious localization, while later results focus on mesh-bias.

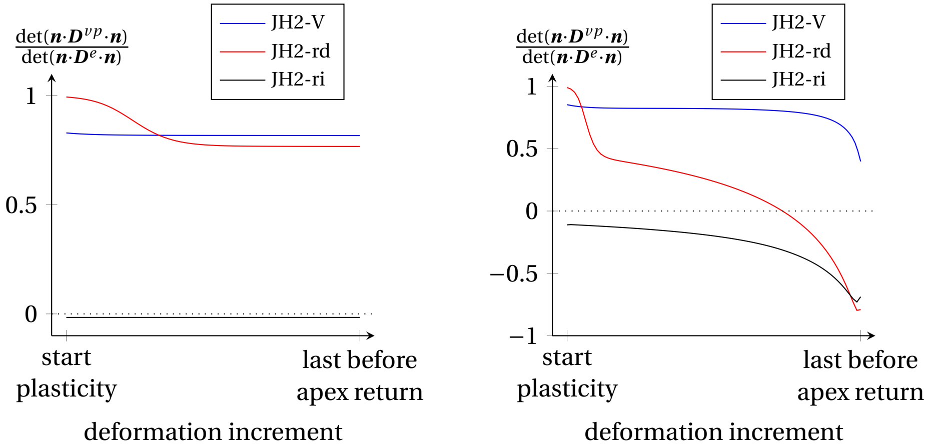

(a) Shear loading

(b) Tensile loading

Figure 2.3: Single element tested under pure shear and uniaxial tension. The graphs show the normalized determinant of the acoustic tensor. A negative value indicates a loss of ellipticity of the boundary value problem. This will lead to mesh-dependent results.

2.4.2. TAPERED BAR CASES

The first test case is a tapered bar subjected to shear, tensile or compressive loading. The bar has a length of 5mm and a width ranging from 1.0-1.1mm. For a tapered bar failure is expected to initiate in the smallest and thus weakest cross section of the bar. Figure 2.4 shows a schematic view of the three tapered bar tests, including the boundary conditions. A deformation δ is applied on the left boundary and a reaction force F is measured.

In all simulations a plane strain formulation is used for the tapered bar. Four noded quadrilateral elements are used with a $2*2$ Gaussian integration scheme. The number of elements is variable, to study mesh dependency 5, 10 and 20 equidistributed elements are used. The displacement is applied in increments of $\Delta u = 1.0 \cdot 10^{-5}$mm. When viscous models are considered a time step is introduced as $\Delta t = 1.0 \cdot 10^{-4}$ms. This ensures a loading rate of 0.1m/s. Although the viscous cases have a time step involved, the loading is quasi-static and inertia effects are excluded from the simulation.

An adaptive load stepping scheme is adopted in order to obtain convergence. In this scheme the previously mentioned increment in displacement is reduced or increased depending on the convergence of the global Newton-Raphson scheme [36]. A constant rate of loading is maintained by scaling the time increment in the same way as the displacement increment.

TAPERED BAR UNDER SHEAR

The tapered bar case under shear from Figure 2.4a is simulated using the JH2-ri model. Figure 2.5a shows the resulting equivalent plastic strain of the tapered bar after 10μm of deformation. From top to bottom 5, 10 and 20 elements are used. The figure clearly shows localization of plastic deformation in a single element. This is confirmed by Fig-

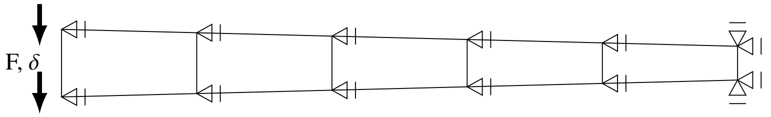

(a) Shear loading

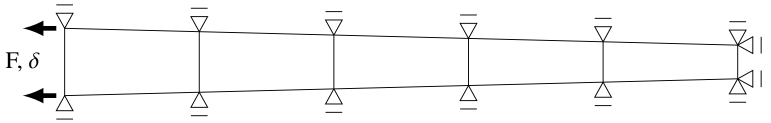

(b) Tensile loading

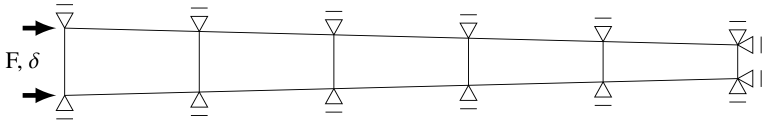

(c) Compressive loading

Figure 2.4: Schematic representation of tapered bar tests. Boundary conditions are shown, the triangles represent a fixed degree of freedom, the arrows indicate the direction of loading.

ure 2.5c, where the equivalent plastic strain is plotted along the bar axis. The load displacement data for these simulations are shown in Figure 2.5b. This confirms the mesh dependency once more, as a finer mesh results in a more brittle response.

A second series of simulations was performed using the new JH2-V model. A viscosity parameter $\eta = 0.2 \cdot 10^{-3}$ GPa·s is chosen such that the plastic deformation occurs in a finite zone. Figure 2.6a shows the resulting equivalent plastic strain of the tapered bar after 10μm of total deformation, which confirms the finite zone of plastic deformation. Figures 2.6b and 2.6c confirm that the plastic zone size has converged for the given range of elements. Compared to the 20 element JH2-ri results (black dotted line in Figure 2.6b) a 3.16% increase of peak load is found.

A third series of simulations is performed with the standard JH2-rd model. The rate parameter $C = 0.025$ is chosen such that the plastic deformation occurs in a finite zone. Figure 2.7a shows the resulting plastic deformation of the tapered bar after 10μm of total deformation. From the figures it can be found that the plastic deformation indeed spreads over a zone rather than localizing in a single element (as was observed for the JH2-ri model). Although the JH2-rd model shows a zone of plastic deformation, the size of this zone still appears to change as the mesh is refined from 10 to 20 elements (Figure 2.7a). Only when the 40 element mesh is compared to the 20 element mesh, the zone appears to be somewhat similar in size. This is confirmed by the equivalent plastic stain profile in Figure 2.7c. It is interesting to note that the plastic zone spreads through the entire bar for the JH2-rd model. The load displacement data in Figure 2.7b shows equal responses for the 5, 10 and 20 element meshes. The increase of peak force is 9.11% compared to the JH2-ri model. This is significantly more than the 3.16% found for the JH-V model.

To compare the plastic zone predicted by the JH2-ri , JH2-rd and JH2-V models the

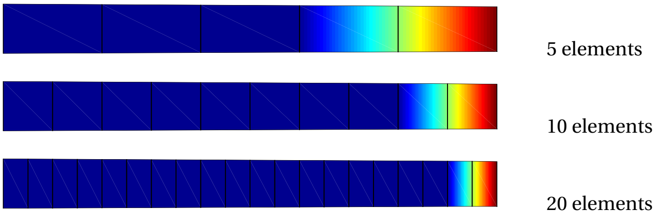

(a) Equivalent plastic strain. Localization upon mesh refinement is clearly visible.

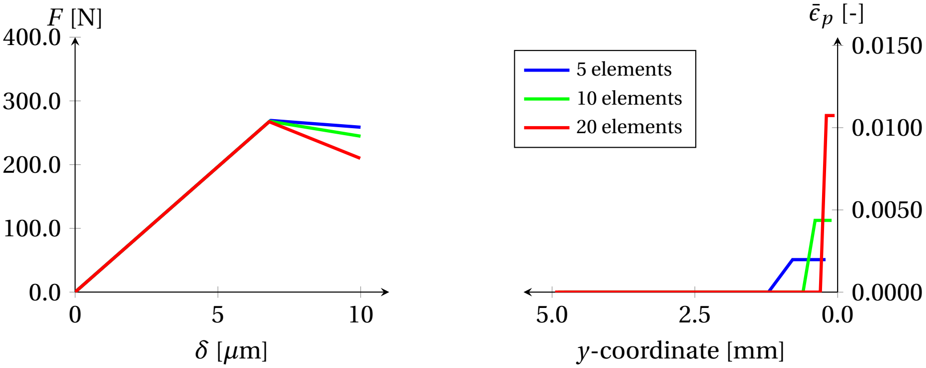

(b) Force displacement graph. Localization upon mesh refinement is clearly visible.

(c) Equivalent plastic strain profile along the tapered bar axis. An increase in equivalent plastic strain can be found for decreasing mesh size.

Figure 2.5: Tapered shear bar results for the JH2-ri model.

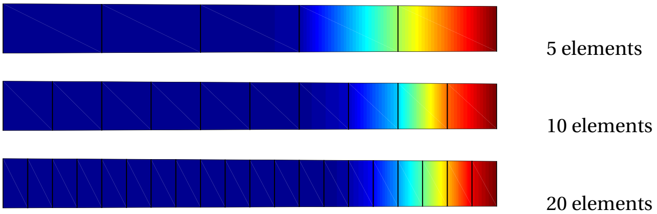

(a) Equivalent plastic strain. Viscosity parameter η is chosen such that regularization is observed. Plastic deformation is found to spread over a zone rather than to localize.

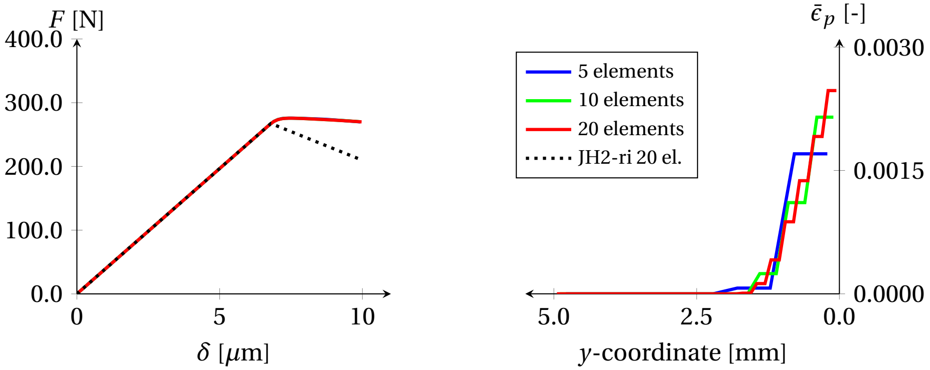

(b) Force displacement graph. All three meshes give similar results. Small increase of strength is observed compared to the JH2-ri model.

(c) Equivalent plastic strain plotted along the tapered bar axis. The profiles are found to converge upon mesh refinement.

Figure 2.6: Tapered shear bar results for the JH2-V model.

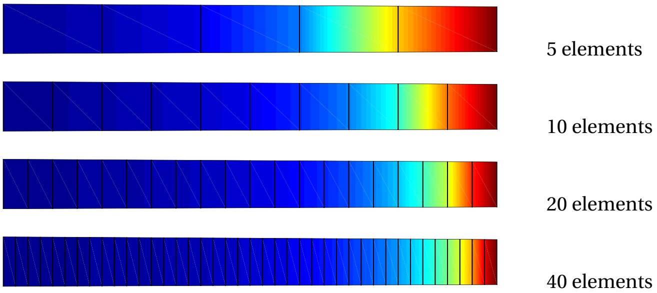

(a) Equivalent plastic strain. Rate dependency parameter C is chosen such that regularization is observed. Plastic deformation is found to spread over a zone rather than to localize.

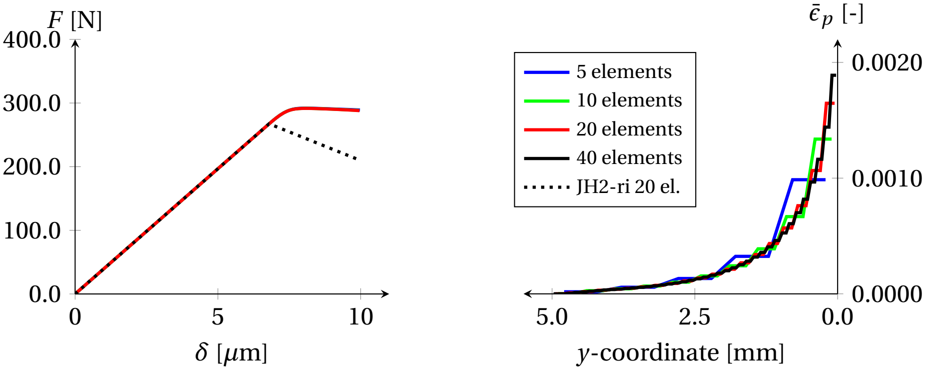

(b) Force displacement graph. All three meshes give similar results. Small increase of strength is observed compared to the JH2-ri and JH2-V model.

(c) Equivalent plastic strain plotted along the tapered bar axis. The profiles are found to converge upon mesh refinement.

Figure 2.7: Tapered shear bar results for the JH2-rd model.

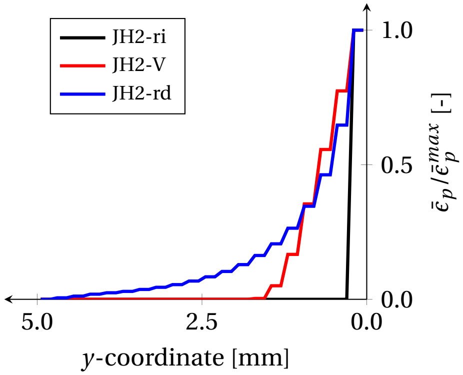

Figure 2.8: Normalized equivalent plastic strain plotted along the tapered bar axis. The 20 element mesh is used, results are for three different material models.

normalized equivalent plastic strain profiles are plotted along the bar axis. Figure 2.8 shows the integration point values of this normalized equivalent plastic strain. The 20 element mesh is used for this comparison. A stepwise profile can be observed for all three cases. This is the result of the use of linear elements, which are only capable of predicting a constant strain in a single element. The figure shows a localized plastic deformation of the JH2-ri model. For the JH2-rd and JH2-V model plastic deformation is found to occur in a zone rather than a single element. The plastic deformation zone of the JH2-rd model is found to extend throughout the entire bar, while the plastic zone of the JH2-V model is smaller.

TAPERED BAR UNDER TENSION

A simulation of the tapered bar under tension from Figure 2.4b is conducted using the JH2-ri model. Figure 2.9a shows the resulting plastic deformation of the tapered bar, discretized with 5, 10 and 20 elements. Similar to the shear loaded bar the plastic deformation localizes in a single element. Neighbouring elements show no plastic deformation. The equivalent plastic strain profiles from Figure 2.9c confirm this. All three meshes are found to have the same amount of equivalent plastic strain. This is because an arc-length method is used and all elements follow the exact same stress strain path.

Arc-length control is used in these simulations to be able to trace snap-back behaviour. This is typical for brittle materials and results from the softening behaviour of the material. As plasticity localizes in a single element other elements are found to unload elastically. This reduces the total force on the bar and also the total deformation to reach this force. The load displacement graph for the tensile bar is shown in Figure 2.9b. The snap-back is clearly seen in the figure. As soon as plastic deformation is initiated the force is reduced and continues to reduce until the element has fully failed. A sudden drop in force is observed when the pressure in the weakest element reaches the apex pressure T, after which apex return is invoked and negative pressures can no longer be supported. Again, similar to the shear case, the curves do not converge when the mesh is refined and mesh-dependency is clearly shown.

A second series of simulations is performed on the tapered tensile bar with the JH2-V

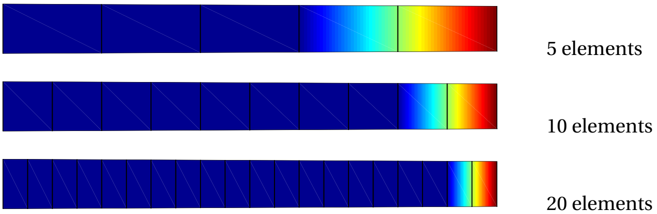

(a) Equivalent plastic strain. Localization upon mesh refinement can be seen clearly.

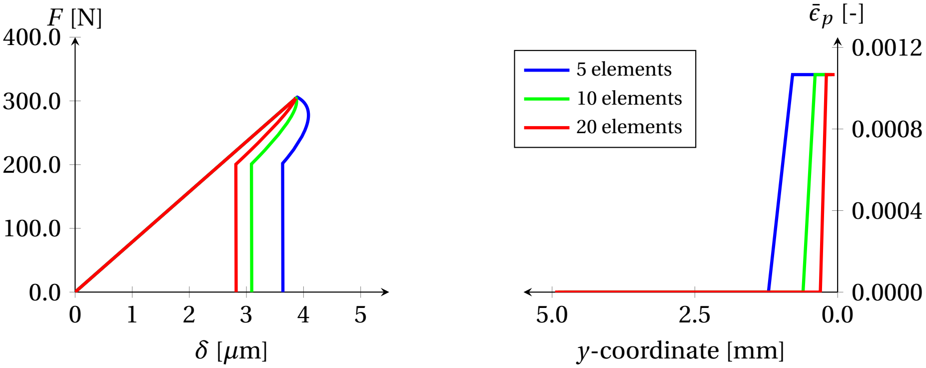

(b) Force displacement graph. Localization upon mesh refinement is clearly visible.

(c) Equivalent plastic strain profile along the tapered bar axis. The equivalent plastic strain can be found to be equal for all mesh sizes.

Figure 2.9: Tapered tensile bar results for the JH2-ri model.

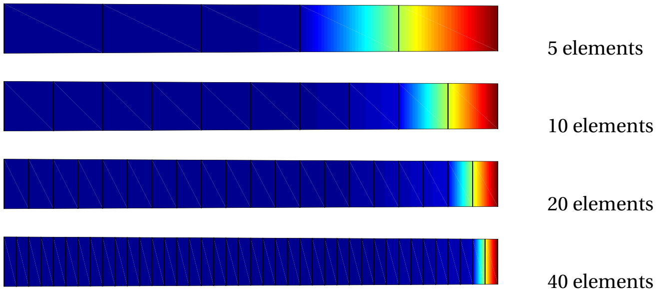

(a) Equivalent plastic strain. Plastic deformation is bound to a zone rather than a single element.

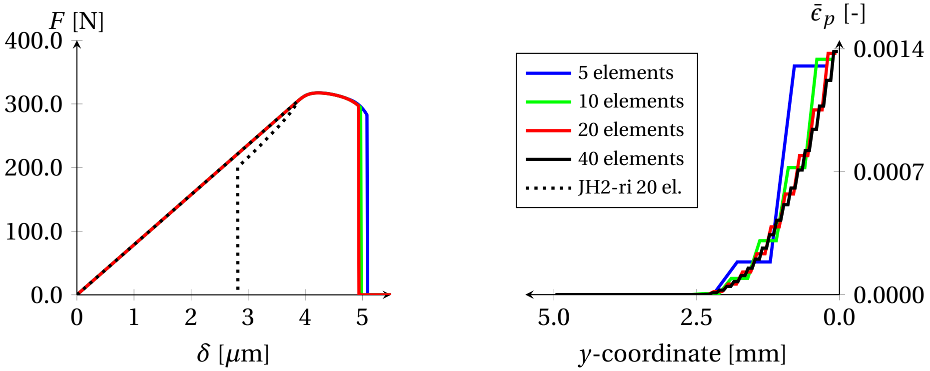

(b) Force displacement graph. All three meshes give similar results. Small increase of strength is observed compared to the regular JH2-ri model.

(c) Equivalent plastic strain plotted along the tapered bar. Profiles are found to converge upon mesh refinement.

Figure 2.10: Tapered tensile bar results for the JH2-V model.

model. Figure 2.10a shows the resulting plastic deformation of the tapered bar right before apex return is invoked. In the tapered bar with the JH2-V model apex return will only be invoked in the weakest element, similar to the JH2-ri model. Showing the equivalent plastic deformation after this apex return would give the impression of mesh-dependency, as the magnitude of equivalent plastic strain in this weakest element under apex return is considerably larger than in neighbouring elements. Showing the equivalent plastic strain before apex return correctly shows the mesh-independence of the model. This mesh-independence is confirmed by the equivalent plastic strain profiles shown in Figure 2.10c. For the JH2-V model the arc-length method can not be used, and therefore the peak values of equivalent plastic strain are not exactly the same for all meshes. The figure shows plastic deformation spreading over a zone rather than localizing in a single element. The load displacement in Figure 2.10b again confirms the mesh independent behaviour of the JH2-V model. The peak load of the JH2-V model is found to be 4.47% higher than the JH2-ri peak load.

A third and final series of simulations is performed on the tapered tensile bar, using the JH2-rd model. Recall that the rate dependency parameter $C = 0.025$ was chosen such that the results under shear were regularized. Figure 2.11b shows the load displacement graph for the JH2-rd model. The peak load of the JH2-rd model is found to be 5.94% higher than the JH2-ri peak load. Compared to the JH2-V results the post peak deformation is smaller and the behaviour appears to be more brittle. Figure 2.11a shows the equivalent plastic strain plots for the tapered bar under tension. Similar to the results from the JH2-V model the equivalent plastic strain is plotted before apex return. The plastic deformation no longer spreads over a zone comparable to the shear case. The figure suggests that plastic deformation is localized in the last element of the bar. However, close examination of integration point data in Figure 2.11c reveals that the plastic deformation does spread to neighbouring elements, although most deformation occurs in the last element of the bar. The peak value of the equivalent plastic strain may be found to reduce upon mesh refinement. Since plastic strain is related to energy dissipation it is clear that reducing the mesh size also reduces the dissipated energy in the system. Next to (spurious) localization this is one characteristic of mesh dependency. So although the value of $C = 0.025$ appears to regularize the solution for the tapered bar under shear, it may not provide regularization under tensile loading. This would be in line with the unit test results from section 2.4.1, which showed that ellipticity was lost for the JH2-rd model under tension but not under shear. To confirm these findings the determinant of the acoustic tensor is computed during the tapered bar test. For this purpose a single integration point in the smallest element at the right side of the bar (Figure 2.4) is analysed. The normalized values of the determinant of the acoustic tensor are presented in Figure 2.12. Both the results for the JH2-rd and the JH2-V model are presented. Ellipticity is lost if condition (2.25) is met. The results once more show that the JH2-rd model loses ellipticity, while the JH2-V model retains ellipticity throughout the simulations. For the JH2-rd model oscillations in the value of the determinant of the acoustic tensor are observed if the value approaches zero. These oscillations are related to reductions of the step size by the adaptive load stepping scheme.

For a more thorough comparison the normalized equivalent plastic strain profiles are compared in Figure 2.13. The 20 element mesh is used for this comparison. Similar to the shear cases the JH2-ri model shows spuriously localized plastic deformation, while the JH2-rd and the JH2-V models show a zone of plastic deformation. When both viscous models are compared by means of the normalized profiles, the sharpest profile is found for the JH2-rd model. Although this model predicts a zone of plastic deformation, most deformation still occurs in the last element. This explains why the plot in Figure 2.11a appears to have localized plastic deformation.

TAPERED BAR UNDER COMPRESSION

As a final check in the tapered bar under compression from Figure 2.4c is studied. The equivalent plastic strain profile for the JH2-ri model is shown in Figure 2.14a. Under compression the plastic deformation is found to occur in a zone rather than to localize in a single element. This behaviour is to be expected since the tapered bar is confined in lateral directions and the material strength increases with pressure. As the bar is loaded the material will experience both plastic softening and an increase in strength with increasing pressure. The latter is observed as an effective hardening of the material. As a result plasticity spreads through the bar. The results for the JH2-V model are similar

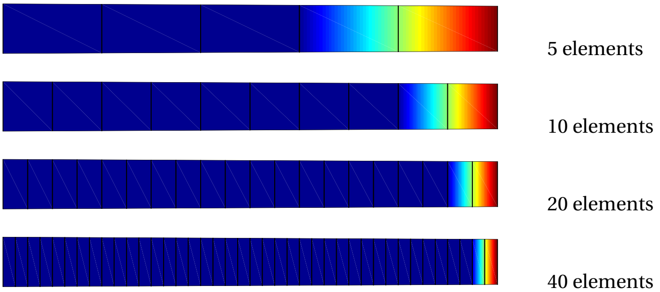

(a) Equivalent plastic strain. Localization upon mesh refinement can be observed, although a small amount of plasticity is found to spread over neighbouring elements. This is in contrast with the shear case, where regularized results were found.

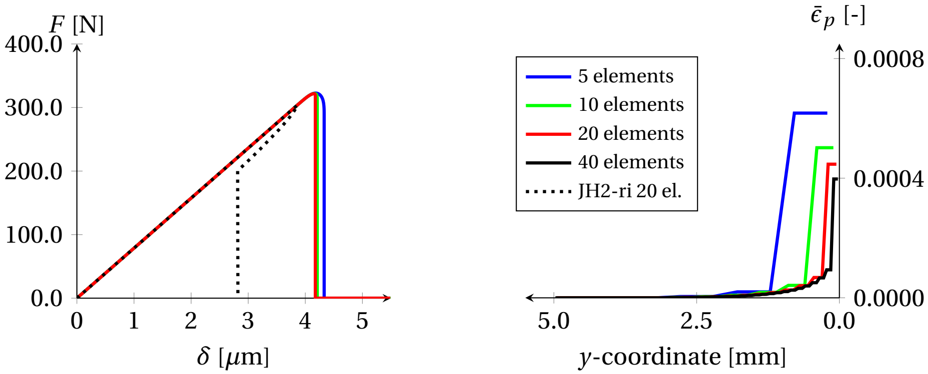

(b) Force displacement graph. Small increase of strength is observed compared to the JH2-ri and JH2-V model.

(c) Equivalent plastic strain plotted along the tapered bar. The profiles do not converge for the current meshes.

Figure 2.11: Tapered tensile bar results for the JH2-rd model. Rate dependent parameter C is equal to the tapered shear bar case. Recall that results were regularized under shear for the chosen C parameter.

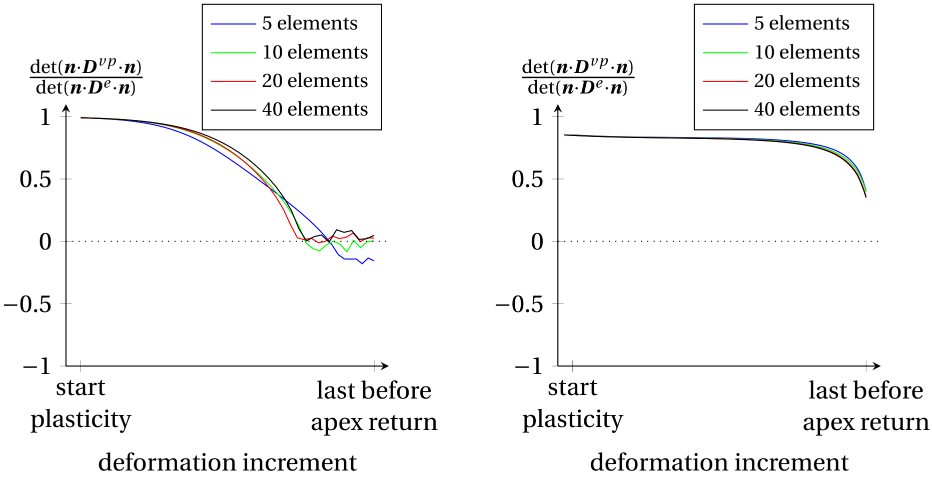

(a) JH2-rd model

(b) JH2-V model

Figure 2.12: A normalized determinant of the acoustic tensor, computed in a single integration point of the weakest element in the tapered bar test. A negative value indicates a loss of ellipticity of the boundary value problem. This will lead to mesh-dependent results.

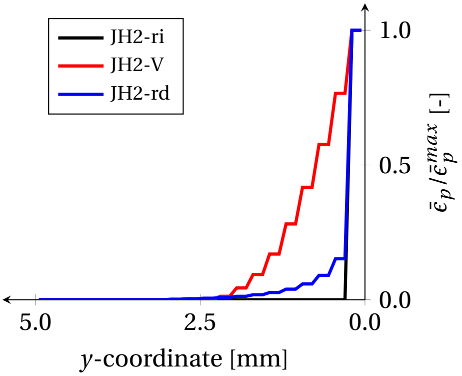

Figure 2.13: Normalized equivalent plastic strain plotted along the tapered bar, loaded under tension. Results are obtained for the 20 element case with three different material models.

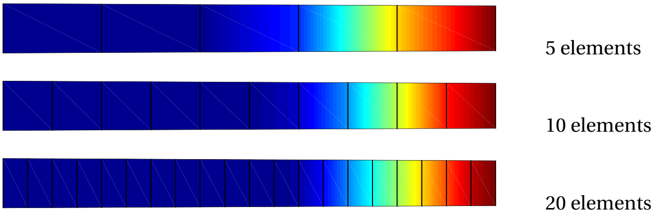

(a) JH2-ri model.

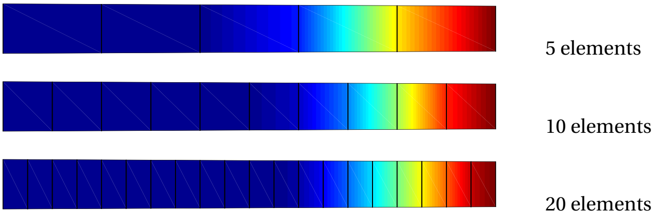

(b) JH2-V model.

Figure 2.14: Tapered compression bar, equivalent plastic strain plots. Localization upon mesh refinement is absent.

and can be found in Figure 2.14b. The similarity was to be expected, as the difference in strength of the JH2-V model is mainly found under tension (Figure 2.1).

TAPERED BAR IN DYNAMICS

The previous results on the tapered bar were all obtained by performing quasi-static simulations. These exclude inertia effects and wave propagation in the bar. Since the JH2 model was originally designed for dynamic loading the model's behaviour under dynamic loads should also be checked. The test case remains the same tapered bar with an applied displacement. The displacement is applied at a rate of 0.1m/s, similar to the quasi-static tapered bar case. This applied rate or velocity will generate a stress wave in the bar. The stress wave will propagate at approximately 10.000m/s given the material parameters from Table 2.1. For the current boundary conditions the stress wave will reflect multiple times before failure is initiated in the weak element.

To obtain the dynamic results an implicit time integration scheme is applied. The Newmark-β scheme is used with $\beta =^1 /_4$ and $\gamma =^1 /_2$. This solution scheme uses the consistent tangent as well as the mass matrix to iteratively find a converged solution for each load increment.

Figure 2.15a shows the equivalent plastic strain in the tapered bar under dynamic tensile loading simulated with the JH2-ri model. Localization of the plastic deformation can be observed at the right side of the tapered bar, similar to the quasi-static results shown previously in Figure 2.9a. The equivalent plastic strain plots are obtained at the final increment before apex return is invoked. Figure 2.16a shows the results for the tapered bar under dynamic loading with the JH2-V model. As seen before, this model provides regularization and the results are mesh independent.

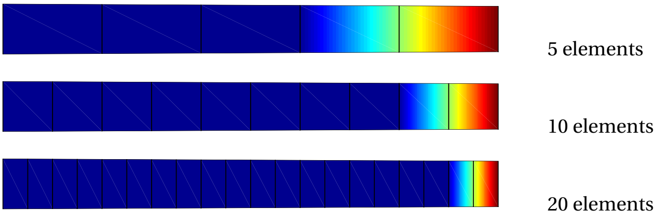

(a) Equivalent plastic strain. Note the localization upon mesh refinement on the right side of the bar.

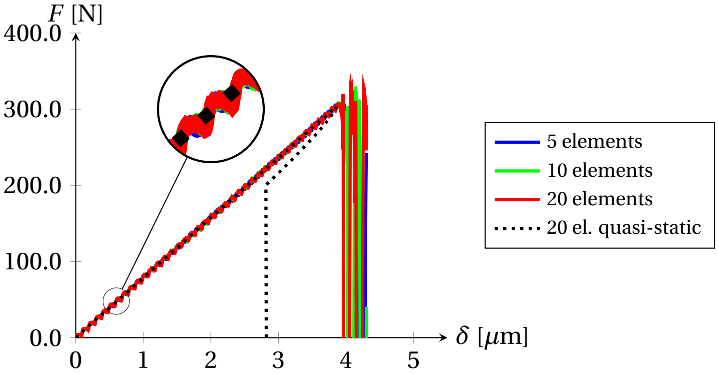

(b) Force displacement graph. All three meshes give the same results. Black dotted line is obtained by quasi-static simulation of the tapered bar under tension.

Figure 2.15: Tapered tension bar results for the JH2-ri model under dynamic loading.

The load displacement graphs of the dynamic tapered bar test are shown in Figure 2.15b and 2.16b. The graphs are similar to the quasi-static case in terms of peak force, but post peak behaviour can be found to differ. For the JH2-ri model the snap-back behaviour is not present in dynamics as arc-length control cannot be applied. For the JH2-V model the total deformation between the peak force and the sudden drop of strength under apex return is extended. In both cases strong oscillations can be found after apex return. This is caused by the sudden loss of strength experienced during apex return. These oscillations may cause additional damage to the material after apex return.

TAPERED BAR CONCLUDED

From the tapered bar tests it is clear that the JH2 model suffers from mesh dependency under tension and shear loading. For compressive loading there is no apparent mesh dependency. The original JH2 model with rate dependency (JH2-rd model) can regularize the problem under shear, but no regularization is found under tension. The proposed JH2-V model offers regularization for both the tensile and shear loaded cases. This conclusion holds for both quasi-static and dynamic loading.

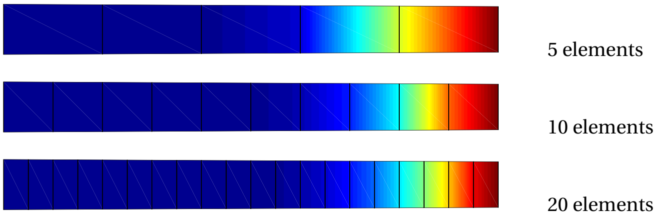

(a) Equivalent plastic strain. Localization upon mesh refinement is absent.

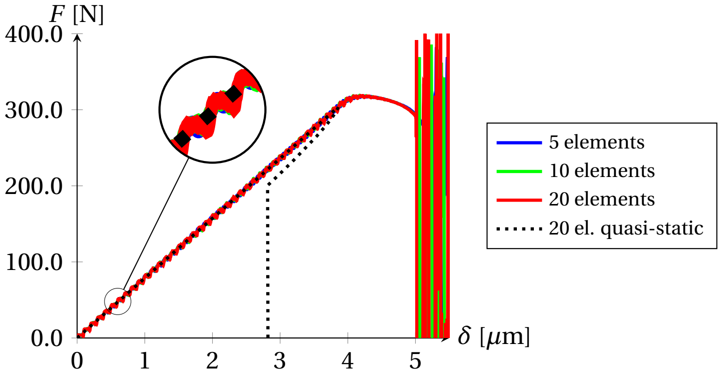

(b) Force displacement graph. All three meshes give the same results. Black dotted line is obtained by quasi-static simulation of the tapered bar under tension.

Figure 2.16: Tapered tension bar results for the JH2-V model under dynamic loading.

2.4.3. MESH BIAS

An important problem related to mesh dependency is mesh bias of the results. When studying ceramics a mesh bias can result in an erroneous prediction of crack propagation. As cone cracks can lead to full armour failure in ceramic armour systems it is of vital importance to objectively capture cracks in the simulations. To study the effect of mesh bias in the JH2 model a direct shear test is considered. By varying the mesh alignment the mesh bias effect can be demonstrated.

The direct shear test is commonly applied in rock mechanics to determine a material's shear strength [38]. A schematic representation of the direct shear test is shown in Figure 2.17a. A cubic specimen is placed in two boxes, each enveloping half of the specimen. The bottom box is fixed, while the top box is displaced to load the specimen in shear. For the current test a loading rate of 1.0 m/s is assumed. The simulations are performed quasi-statically, thus excluding inertia effects. For the current test the width and height of the specimen are assumed to be 3mm.

In the direct shear experiment the boundary conditions of the specimen are defined by the contact with the boxes, which can only transmit compressive loads. For the FE simulations the boundaries are applied as in Figure 2.17b. The specimen sides are supported in normal direction over half of their length only. These conditions are a simplification of the contact problem defined by the boxes. The current boundary conditions were found to prevent boundary induced tensile damage in the material.

To study the effect of bias three different meshes are used: a horizontally aligned mesh, an upward slanted mesh and a downward slanted mesh. These meshes will be referred to as the mesh with “no bias”, “upward bias” and “ downward bias”. The upward biassed mesh is aligned with the principal stress direction found for this direct shear test, as is shown in Figure 2.17c.

DIRECT SHEAR FOR JH2-RI

To provide a benchmark of the direct shear test initially the JH2-ri model is used. Material parameters are the same as those used to study the tapered bar case, except the Poisson's ratio which is $\nu = 0.22$ for the direct shear tests. Load displacement data for the different mesh alignments are shown in Figure 2.18. Peak forces are similar for all three meshes, while large differences in post peak behaviour can be found. The meshes with an up- and downward bias are able to maintain a higher force in the post-peak regime when compared to the horizontally aligned mesh. Of all three mesh alignments the upward slanted mesh predicts the highest force for a given level of deformation, thus having the most ductile post peak response. These results once again illustrate the mesh dependency problem facing the JH2-ri model. Figure 2.20a shows the damage profiles of this direct shear test after 25μm of applied deformation. For all three mesh directions the damage profile is found to follow the mesh alignment. This is particularly clear in the upward slanted mesh, where two lines of high damage (i.e. cracks) are found to propagate from the boundary along a single line of elements. These damage profiles clearly demonstrate the mesh bias problem for the JH2-ri model.

DIRECT SHEAR FOR JH2-RD

Figure 2.20b shows the damage variable after 25μm of applied deformation for the JH2-rd material model. The viscosity is the same as for the tapered bar test. The damage pro-

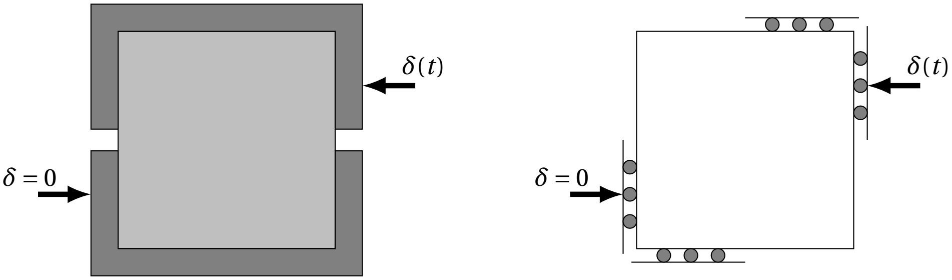

(a) Schematic representation.

(b) Simulation boundary conditions.

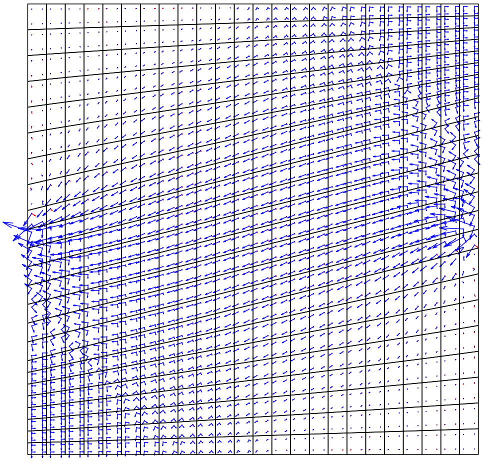

(c) Principal stress direction, elastic loading, upward slanted mesh.

Figure 2.17: Direct shear test.

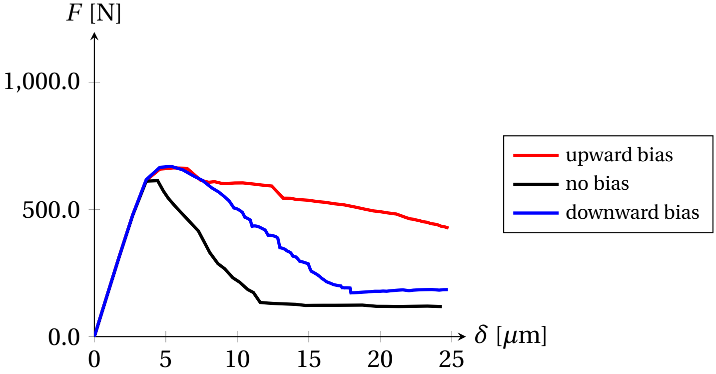

Figure 2.18: Direct shear test using the JH2-ri model. The peak strength of the material is more or less equal for all meshes. However, a strong mesh dependency can be found in the post peak behaviour of the material.

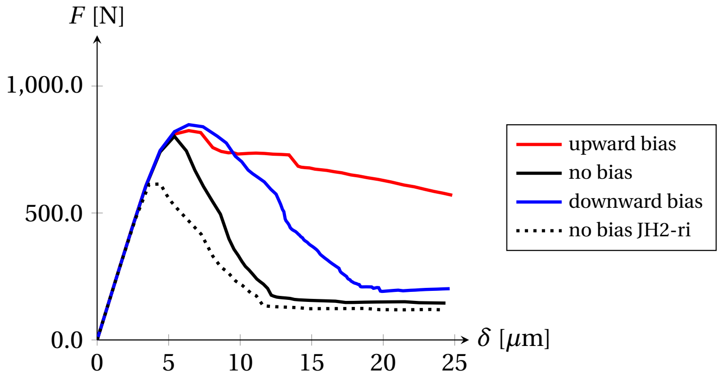

Figure 2.19: Direct shear test using the JH2-rd model with $C = 0.025$. A strong mesh dependency is present in the post peak behaviour of the material.

files for the JH2-ri and JH2-rd models appear to be similar and both show a mesh bias in the results. This is in line with the previous sections, where the JH2-rd model was found to provide insufficient regularization. The load displacement graph for this model can be found in Figure 2.19. Compared to the JH2-ri model the peak values are considerably higher, for the horizontal aligned mesh the difference is 30.59%. The post peak behaviour for the JH2-rd model does still show mesh dependence. Where the mesh dependence is a consequence of the bias effect and is not related to the mesh size as seen for the tapered bar.

DIRECT SHEAR FOR JH2-V

The damage profiles for the JH2-ri model are compared to the JH2-V model in Figure 2.22. The viscosity is the same as for the tapered bar test. For the horizontally aligned mesh it is clear that damage is also found outside the middle two rows of elements. Similarly the downward slanted mesh predicts failure in a larger zone than what is found for the JH2-ri model. The upward slanted mesh simulated with the JH2-V model shows damage to occur in a smaller zone compared to the JH2-ri model. The damage profiles for all three meshes show more resemblance for the JH2-V model compared to the profiles of the JH2-ri model. It must be stated that although the results are an improvement, there is still some mesh bias present in these results. The load displacement data can be studied from Figure 2.21. The peak force values are found to increase significantly compared to the JH2-ri model. For the horizontal aligned mesh the difference is as large as 52.77%, much more than what was found for the JH2-rd model. This is the opposite of what was found for the tapered bar test, where JH2-rd predicted a larger peak force than the JH2-V model. For the JH2-V model the post peak behaviour is now found to be similar for all three meshes up to $15-20\mu$m of deformation.

MESH BIAS RECONSIDERED

The direct shear test has been simulated with four noded quadrilateral elements. These elements are known to suffer from mesh locking. To alleviate mesh locking, the B-bar method developed by Hughes [39] is applied. This method relies on a mixed integration

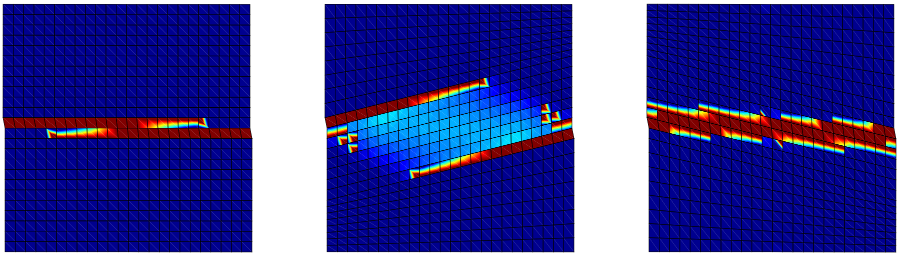

(a) JH2-ri

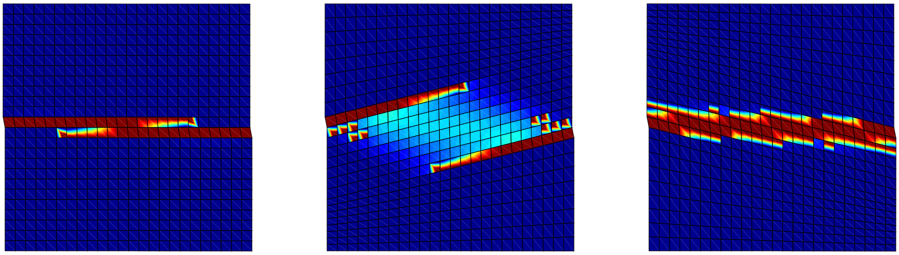

(b) JH2-rd

Figure 2.20: Direct shear test, damage scalar $D \in [0..1]$ is plotted. Different mesh alignment is considered from left to right.

scheme. Deviatoric stresses are integrated using a $2 * 2$ Gauss integration scheme, while the hydrostatic stress is computed using a reduced 1 point Gauss integration.

Figure 2.23 shows the load displacement plots for both the JH2-ri and JH2-V models simulated with the B-bar method. The simulation results with the B-bar method appear to be much less mesh dependent, as the post peak responses lie closer for all three meshes. This holds true for both the JH2-ri and JH2-V model.

The damage profiles of the direct shear test with the B-bar method are shown in Figure 2.24. For the JH2-ri model the profiles are similar for all three meshes. Similarly, the JH2-V model shows good agreement for the damage profiles from all three meshes. For the mesh with horizontal alignment the JH2-ri model predicts failure in a single row of elements. The JH2-V model results in a failure zone including and surrounding this central line of elements. These results show that although mesh bias may be strongly reduced by using the B-Bar method they may still suffer from minor spurious localization.

MESH BIAS CONCLUDED

The direct shear test has been simulated using the JH2-ri , JH2-rd and JH2-V models. The JH2-ri model showed a clear mesh bias effect in both the damage profile and the load displacement plots. Using the JH2-rd model did not remove or reduce this type of the mesh dependency. This is in line with the results from the previous section where JH2-rd was not able to fully regularize the tapered bar test. When the JH2-V model is applied the

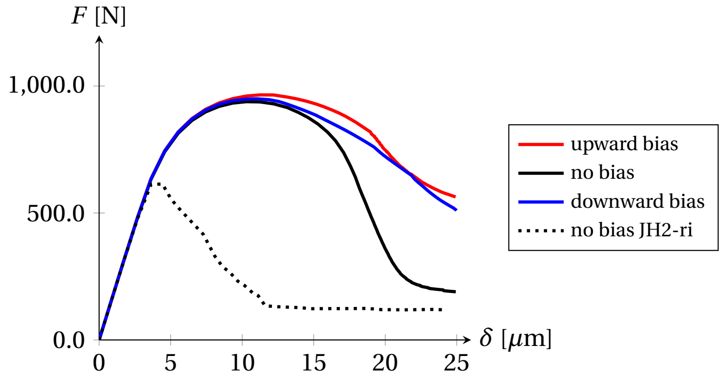

Figure 2.21: Direct shear test using JH2-V model with $\eta = 0.2 \cdot 10^{-3}$ GPa·s. The peak shear force is similar for all meshes. Compared to the JH2-ri model results there is a large increase in peak force. The post peak behaviour is similar for all three meshes, up to a deformation of around 15μm.

damage profiles clearly show a reduced mesh bias effect. This is also confirmed by the load-displacement data. When using the B-bar method with the JH2-V model the mesh bias can be reduced even further, while still predicting a failure zone wider than a single line of elements.

2.5. DISCUSSION

The proposed viscosity of the JH2-V model has a linear formulation. In the previous sections it was shown that this regularizes the solution of the tapered bar case for all investigated load scenarios. However, these results were all obtained for the same loading rate. If the applied loading rate changes by some orders of magnitude the time scale of the load may be of a different order compared to the relaxation time of the viscous system. This mismatch in load and relaxation time can lead to one of the two following problems. The first problem appears for low loading rates, where the viscosity may be insufficient to provide regularization [40]. For the tapered bar this is easy to show, as localization reappears for very low loading rates. A non-local model may be used in addition to visco-plasticity to solve for this problem at low loading rates [27]. A second problem for viscous regularization can be found for much larger loading rates, where the failure zone size is found to increase dramatically in size. The latter problem will be addressed in the current section. The loading rate effect is studied for the JH2-V model. The JH2-rd model is not used, as previous results showed unsatisfactory regularization for this model. The tapered bar under tension is considered. The case is simulated dynamically, where a velocity boundary condition is applied to generate a tensile stress wave.

The proposed viscous model has been studied for its regularizing properties up to this point. The current section will end by showing the physical implications of the proposed viscous model. To do so, a spall experiment is simulated and results are compared.

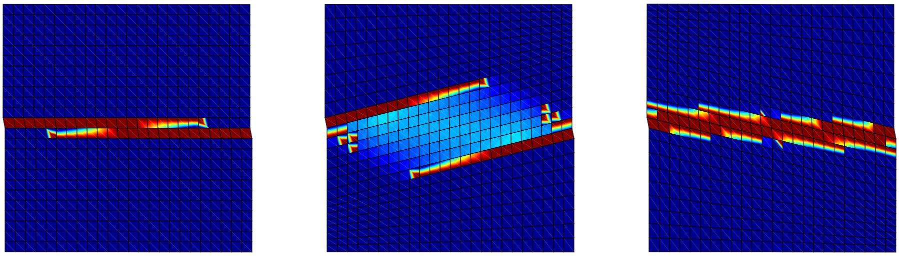

(a) JH2-ri

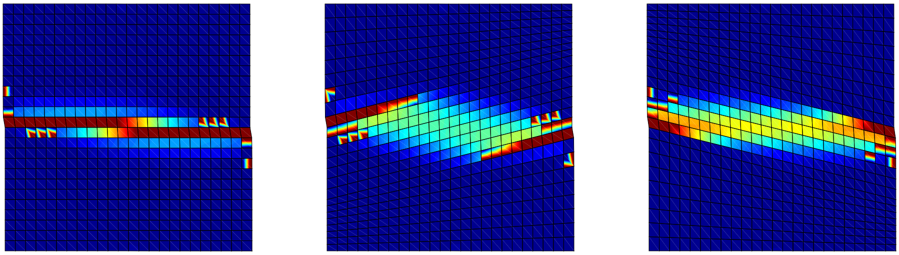

(b) JH2-V

Figure 2.22: Direct shear test, damage scalar $D \in [0..1]$ is plotted. Different mesh alignment is considered from left to right.

2.5.1. LOADING RATE

Figure 2.25a shows the equivalent plastic strain profiles for the tapered tensile bar subjected to a range of loading rates. The profiles are plotted right before apex return is invoked in the weak element. From top to bottom the applied loading rate is 0.05, 0.1, 0.2, 0.4, 0.8, 1.6, 3.2, 6.4 m/s. Note that the applied loading rate has been 0.1 m/s so far.

It can be seen that the lower loading rate of 0.05m/s predicts a smaller failure zone. If the failure zone size falls below the element size the results would be similar to those obtained by the standard JH2-ri model. Please note that the regularization effect is still present and would reappear upon mesh refinement. For increased loading rates these figures clearly demonstrate a widening of the failure zone. For the four highest loading rates plastic deformation can even be found to spread through the entire bar. The equivalent plastic strain profile found in Figure 2.25b confirms the widening of the failure zone with increased rate.

2.5.2. NON-LINEAR VISCOSITY

In the previous section the failure zone size was found to increase rapidly with loading rate. Figure 2.25b shows that an increase of loading rate from 0.1 to 0.4m/s is sufficient to double the failure zone size from 2.5 to 5.0mm. When applying the JH2-V material model for real world problems (e.g. indentation or impact simulations) the loading rates may differ by a few orders of magnitude. An increase of failure zone size of this magni-

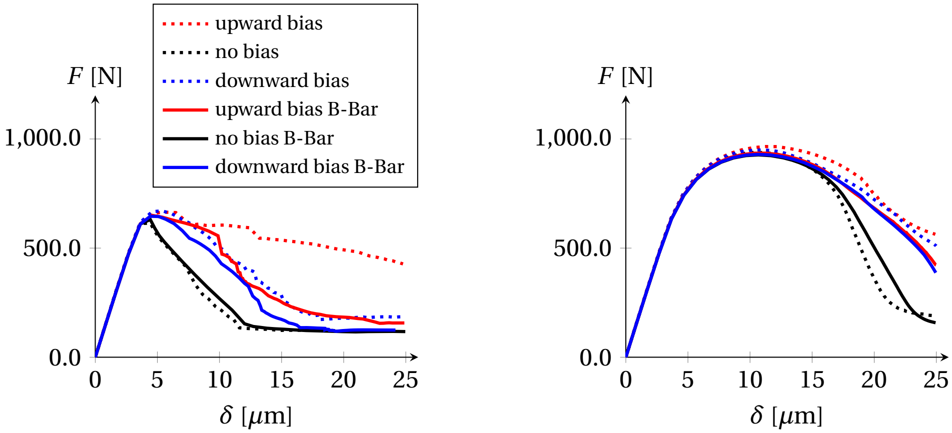

(a) JH2-ri model.

(b) JH2-V model.

Figure 2.23: Direct shear test load displacement plots. Solid lines are obtained with the B-bar method, dotted lines without.

tude may not be desired. For regularization this increase is unnecessary and physically it may be unrealistic. To limit the failure zone size for high rates the viscosity parameter must be reduced. The simplest way to do this is manually through the input parameters. The viscosity would be problem dependent and would require prior knowledge on the occurring rates in the material during the simulation. A second and more robust approach would be to use a non-linear viscosity formulation, in which the viscosity is automatically reduced as the loading rate increases. The second option is chosen and the original viscosity formulation from (2.14) is reformulated. For low loading rates the original model is used, but beyond a threshold rate of $\dot{\lambda}_t$ a logarithmic function is be used. The apex pressure may be formulated to read

$$T(\dot{\lambda}) = \begin{cases} T_0 + \eta\dot{\lambda} & \text{for } \dot{\lambda} < \dot{\lambda}_t, \\ T_t\left(1 + \frac{\eta\dot{\lambda}_t}{T_t}\ln\left(\frac{\dot{\lambda}}{\dot{\lambda}_t}\right)\right) & \text{else.} \end{cases} \tag{2.26}$$

The apex pressure corresponding to the threshold rate can be found as $T_t = T_0 + \eta\dot{\lambda}_t$. The formulation in (2.26) is C^1 continuous, which aids in the convergence of the local Newton-Raphson scheme. Also note that this formulation converges to the linear viscosity formulation (2.14) for $\dot{\lambda}_t \to \infty$.

Figure 2.26 shows how the apex pressure from (2.26) evolves with rate in the mixed linear/logarithmic formulation. A viscosity $\eta = 0.2 \cdot 10^{-3}$ GPa·s and an initial apex pressure $T_0 = 0.2$ GPa are used. The black dotted line provides the evolution of the apex pressure in the limit case of a viscosity formulation with $\dot{\lambda} = \infty$, the black dashed line is the fixed apex pressure found for the JH2-ri and JH2-rd models. The coloured lines show the evolution of the apex pressure for a variation of the threshold rate $\dot{\lambda}_t$. The increase of apex pressure (i.e. strength) with loading rate for rates above the threshold value is considered. As the rate increases the incremental increase in strength gradually reduces. For

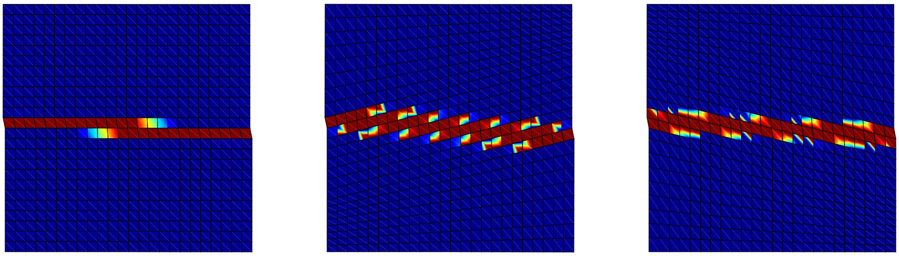

(a) JH2-ri

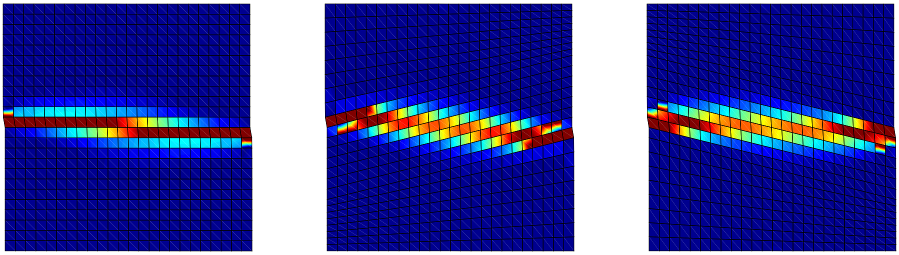

(b) JH2-V

Figure 2.24: Direct shear test using JH2-ri model (top) and JH2-V model with $\eta = 0.2 \cdot 10^{-3}$ GPa·s (bottom). Damage scalar $D \in [0..1]$ is plotted. Different mesh alignment is considered in the three figures. A mixed integration scheme is used for all simulations.

sufficiently high rates the increase in material strength may even become negligible and approaches zero. If the strength increase with loading rate is sufficiently small the material model effectively loses its rate dependency and thus loses its regularizing property. This effect can be found for sufficiently large loading rates. How large this loading rate should be before the regularization is lost depends on the threshold value. For a lower threshold value a smaller rate will suffice to lose the capability of regularization.

The apex formulation (2.26) is used to simulate the tapered bar for loading rates ranging from 0.05 – 6.40m/s. The following results are found for $\eta = 0.2 \cdot 10^{-3}$ GPa·s and three threshold values $\dot{\lambda}_t = 5.0,\ 50.0$ and $500.0\ \mathrm{s}^{-1}$. Figure 2.27 shows the equivalent plastic strain profiles along the bar axis, plotted for three different threshold values $\dot{\lambda}_t$. On top in Figure 2.27a a low value of the threshold $\dot{\lambda}_t = 5.0\ \mathrm{s}^{-1}$ is used. All loading rates show that most failure occurs in the weak element of the bar. These results appear to be similar to the inviscid model results and one could conclude that this threshold value does not provide sufficient regularization. This is in line with previous observations from Figure 2.26, where it was concluded that regularization may be lost if the rate is relatively high compared to the threshold value.

For a threshold value $\dot{\lambda}_t = 50.0\ \mathrm{s}^{-1}$ the failure can already be found to spread over a zone rather than to occur in a single element, as is shown in Figure 2.27b. For this threshold value all loading rates produce similar failure zones at the weak side of the

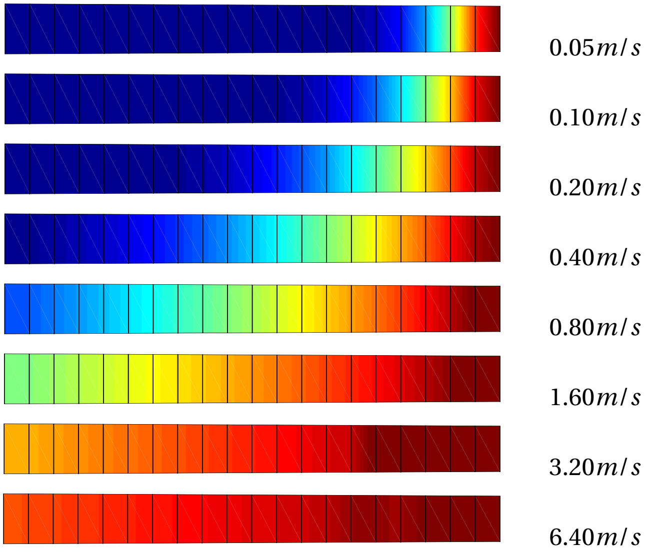

(a) Equivalent plastic strain.

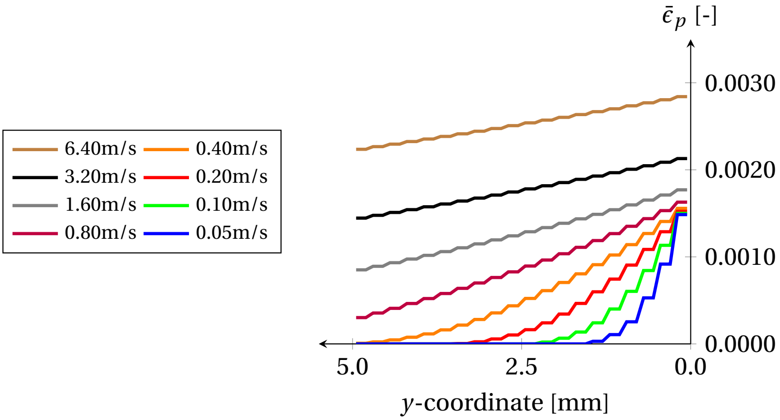

(b) Equivalent plastic strain profile along the tapered bar axis.

Figure 2.25: Tapered tension bar results for the JH2-V model with a linear rate dependency. The velocity is applied suddenly on the boundary.

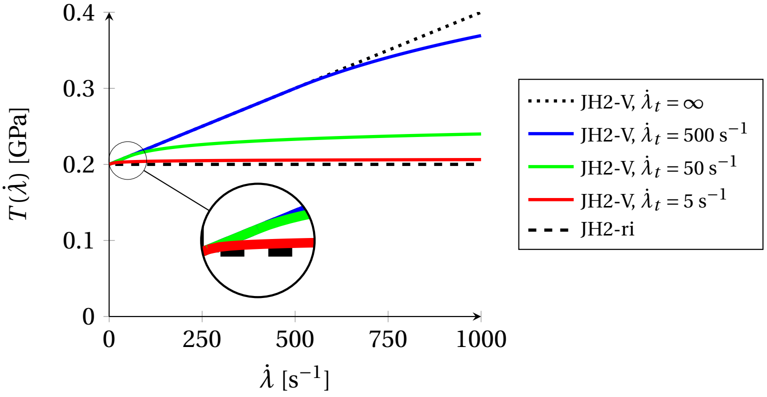

Figure 2.26: Apex pressure T from (2.26) plotted as a function of loading rate. Three different threshold rates $\dot{\lambda}_t$ are used. The apex evolution for JH2-V and JH2-ri with rate are added as a reference.

bar. Small deviations in peak values are observed, but the main profile shapes are maintained. For this threshold value it appears that the spreading of the failure zone is limited for increasing values of loading rate.

When the threshold value is increased to $\dot{\lambda}_t = 500.0$ s^{-1} the profiles of Figure 2.27c are found. These show a growing failure zone size with loading rate. As a comparison the results for the limit case of a viscosity with $\dot{\lambda} = \infty$ are added as the dotted lines. Up to a rate of 0.80m/s both parameter sets give the same results and the solid and dotted line are on top of each other. Only for higher rates there is a noticeable difference in the results. For the finite threshold rate $\dot{\lambda}_t = 500.0$ s^{-1} the equivalent plastic strain profiles for 3.20 and 6.40m/s are found to approach one another. This shows that the desired limiting behaviour of the mixed linear/logarithmic viscosity formulation remains present, but only for a high loading rate. In practice the latter means that the failure zone size is not only controlled by the viscosity η but also through the threshold rate value $\dot{\lambda}_t$.

The tapered bar problem simulated with three values of the threshold rate shows that the failure zone size can be limited by the linear/logarithmic formulation. It does depend on the chosen value of the threshold, if chosen too small the model loses its regularizing properties, if chosen too high the failure zone size may be larger than desired.

The newly proposed mixed linear/logarithmic formulation is subjected to a mesh refinement study. Figure 2.28 shows the resulting equivalent plastic strain profiles for four different meshes, loaded with a suddenly applied velocity of 0.8m/s. The profiles are found to converge for a increasingly fine mesh. It is therefore concluded that the mixed linear/logarithmic formulation can provide mesh independent results. However, the limitations on the threshold rate mentioned in the previous paragraph should be taken into account.

A final remark on the viscosity formulation is given. In section 3.3 it was concluded that the JH2-V model with a linear apex viscosity is sufficient for regularization. In the current section it is shown that this also holds for a mixed linear/logarithmic formulation. The latter is a more general formulation as it can be shown that the linear/logarithmic

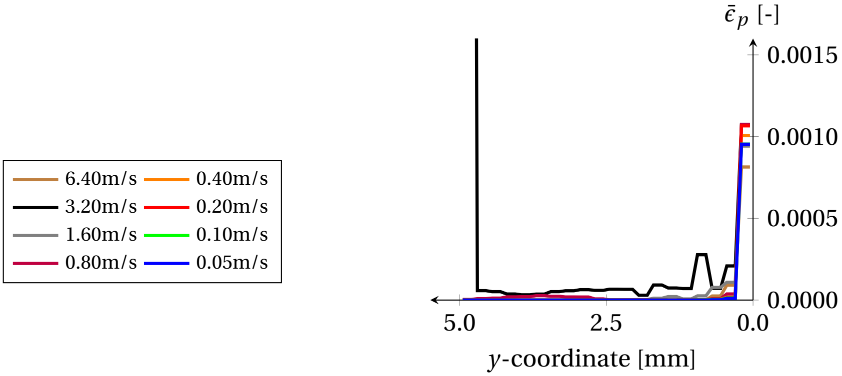

(a) JH2-V model with linear/logarithmic formulation and $\dot{\lambda}_t = 5.0\,\mathrm{s}^{-1}$.

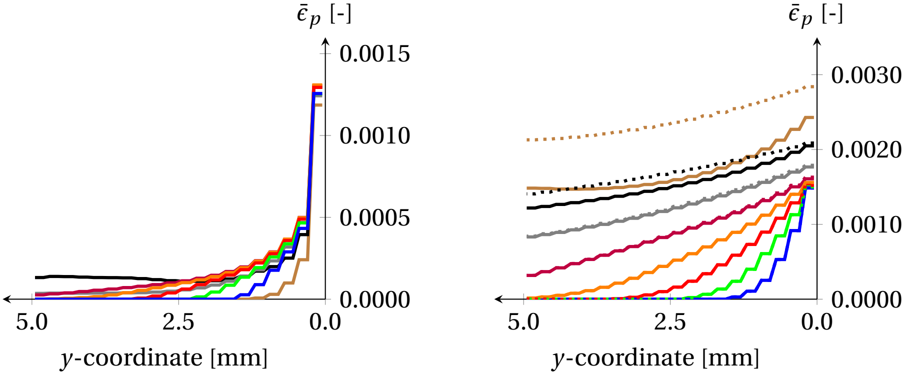

(b) JH2-V model with linear/logarithmic formulation and $\dot{\lambda}_t = 50.0\,\mathrm{s}^{-1}$.

(c) JH2-V model with linear/logarithmic formulation and $\dot{\lambda}_t = 500.0\,\mathrm{s}^{-1}$.

Figure 2.27: Tapered tension bar results for the JH2-V model with a mixed linear/logarithmic rate dependency. Equivalent plastic strain profiles are plotted along the bar axis.

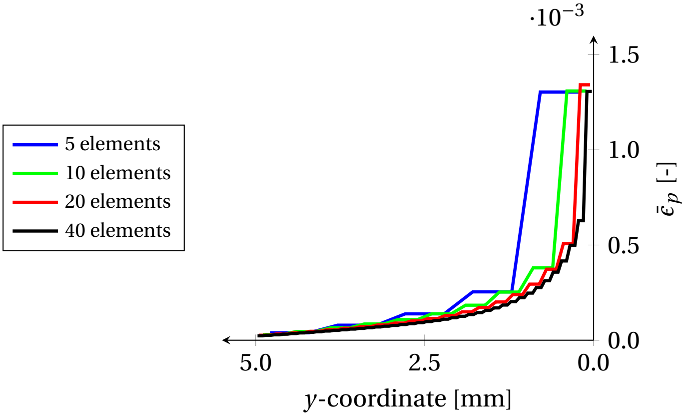

Figure 2.28: Tapered tension bar results for the JH2-V model with a mixed linear/logarithmic rate dependency. Threshold parameter $\dot{\lambda}_t = 50.0$ s^{-1}. Equivalent plastic strain profiles are plotted along the bar axis for four different meshes.

formulation reduces to a linear one for $\dot{\lambda} \to \infty$. The mixed formulation is preferred, as it allows for control of the failure zone size. Which may be required from a physical point of view. Obtaining an objective and physical response of the proposed linear/logarithmic formulation now depends on the model parameters η and $\dot{\lambda}_t$. For a given type of ceramic these parameters will have to be calibrated to match experimental results. The next section shows how this can be done for an alumina ceramic.

2.5.3. COMPARISON TO EXPERIMENTS

Until now the proposed viscous model has been studied for its numerical behaviour only. The previous sections have shown that the proposed model can lead to mesh-independent results. As a final step the physical implication of the proposed model is investigated. A spall experiment on alumina ceramic is used, as described in [33]. In this experiment an alumina plate is subjected to a stress wave, propagating though the thickness of the plate. The centre of this plate experiences uniaxial strain conditions. Therefore the test is simulated as a single column of elements, where only axial movement is allowed. A compressive stress pulse is induced by applying one of the velocity profiles from Figure 2.29a to the bottom surface of the column. These profiles are simplified representations of the waves shown in [33]. In the current chapter nine different wave amplitudes are considered, for each a spall strength and a certain loading rate can be determined. Upon reflection of the compressive stress wave at the (free) top surface of the column tensile stresses will be generated and the material fails. The paper [33] provides the material properties $E = 360$GPa, $\nu = 0.22$ and $\rho = 3890$ kg/m^3. The other model parameters are taken from Table 2.1, but with $P_{HEL} = 3.5$ GPa, $\sigma_{HEL} = 4.125$ GPa, $d_1 = 0.005$ and $d_2 = 0.75$. A minimal failure strain of $\bar{\epsilon}_p^{max} = 1.5 \cdot 10^{-4}$ is enforced to prevent immediate full failure below the static apex pressure T.

For the spall simulation the strength is defined as the highest axial stress found in all material points, up to the point of first apex failure. At the same location and time where this highest stress is found, the strain rate will also be determined. This strain rate is simply defined as the rate of total axial strain.

Figure 2.29b shows the predicted spall strength from the simulations, compared to the experiment. It is clear that the JH2-ri and JH2-rd models fail to capture the rate dependency of the spall strength. The JH2-ri model predicts a constant strength as a function of rate. This agrees well with the theoretical strength of the rate independent JH2 model. This theoretical strength may be computed from the yield surface, as it is the location where the surface is first reached under the applied loading and boundary conditions. For the given material parameters it can easily be shown that this occurs for an axial tensile stress $\sigma = 321.56$MPa. The spall strength predicted by the JH2-rd model is higher than the JH2-ri strength, which can be attributed to the rate dependency in the model. The strength for the JH2-rd model is nearly constant, a slight increase with loading rate may be observed. For the higher rates a minor scatter in the spall strength is found, this can be attributed to the time step size in the simulations. The JH2-V model does capture the rate dependency, a good fit is found for $\eta = 0.028 \cdot 10^{-3}$ GPa·s and $\dot{\lambda}_t = \infty$. The results for finite values of the threshold rate are also shown in Figure 2.29b, they do not match the experimental results for the chosen values of η and $\dot{\lambda}_t$.

With the spall strength results the threshold rate $\dot{\lambda}_t$ can also be given a physical meaning. Figure 2.29b shows a change in slope of the spall strength at the finite threshold rates $\dot{\lambda}_t$. Physically this change in slope can be related to a change in failure mechanism, which is often observed when investigating rate dependency of brittle materials. If known, one may use the rate at which the mechanism changes as the value of $\dot{\lambda}_t$.

When only the spall strength is considered it is clear that a finite threshold rate is not required to match the experimental data. In subsection 2.5.2 it was concluded that an unphysical failure zone size is a reason to use a finite threshold rate. Therefore a check on the failure zone size is performed for the spall test, to confirm that the current infinite threshold rate is indeed correct. The simulations are now extended to a 2d simulation on a 10mm high and 2.5mm wide plane strain column. Boundary conditions and material parameters remain the same as before.

In Figure 2.30 the failure zones from the spall simulations are compared to the experimental result. Experimentally the spall zone could only be studied for the lowest applied stress wave, as for higher stress waves the specimen could not be recovered. For the original experimental results a failure zone size of 2.3mm is reported, starting 2.1mm from the free surface. The simulation results are obtained by applying wave 2 from Figure 2.29a to the structure , with the same material parameters as those used to obtain the spall strengths of Figure 2.29b. The colours in Figure 2.30 represent the damage variable $D \in [0..1]$. The JH2-rd results are omitted, as this model already failed to capture the spall strength. The JH2-V and JH2-ri results are both presented, the JH2-ri model is added because it is a limit case of the JH2-V model (i.e. $\eta \to 0$). All simulation results show full failure in the 2.3mm zone, similar to the experiment. The JH2-ri model shows either full damage or no damage in the mesh, which once again confirms the results for the JH2-ri model being mesh dependent. The JH2-V model results show a more gradual failure process, with material which is neither intact nor fully failed. The zone with partial failure extends beyond the 2.3mm wide zone. It is uncertain if this is also true in the experiments, as only macrocracks (i.e. full failures) are visible. As more ex-

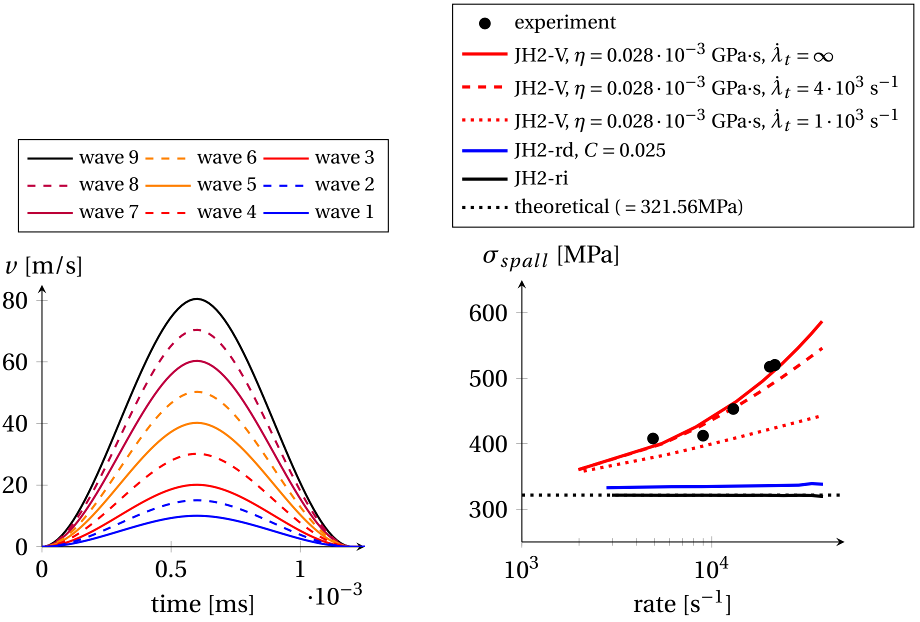

(a) Applied velocity to induce a stress wave in the spall simulations.

(b) Spall strength, experimentally measured and predicted by simulation. The original JH2 model is unable to capture the rate dependency, while the proposed JH2-V model can capture the rate dependency.

Figure 2.29: Spall test on alumina ceramic, comparing experiments to simulations.

perimental data become available this question might be answered. For now the JH2-V model with $\eta = 0.028 \cdot 10^{-3}$ GPa·s and $\dot{\lambda}_t = \infty$ is considered to be sufficient, as the spall strength agrees with the experimental data and a comparison with the single available experimentally measured failure zone size does not offer any objection to this conclusion. More experimental results on the failure zone are required to validate this choice.

2.6. CONCLUSIONS

The JH2 material model was found to suffer from mesh dependency. Tapered bar and direct shear tests showed spurious localization as well as mesh bias. The logarithmic rate dependency included in the original model was found to remove mesh dependency in the tapered bar test under shear loading. However, when using the same model parameters under tensile loading mesh dependency reappeared. In the direct shear test the original rate dependency also failed to provide sufficient regularization.

An apex viscosity was proposed as a modification to the JH2 material model. A linear apex viscosity formulation was found to provide sufficient regularization as spurious localization was not present and mesh bias effects were reduced compared to the JH2 model.

In dynamic simulations the introduced linear formulation revealed a potential prob-

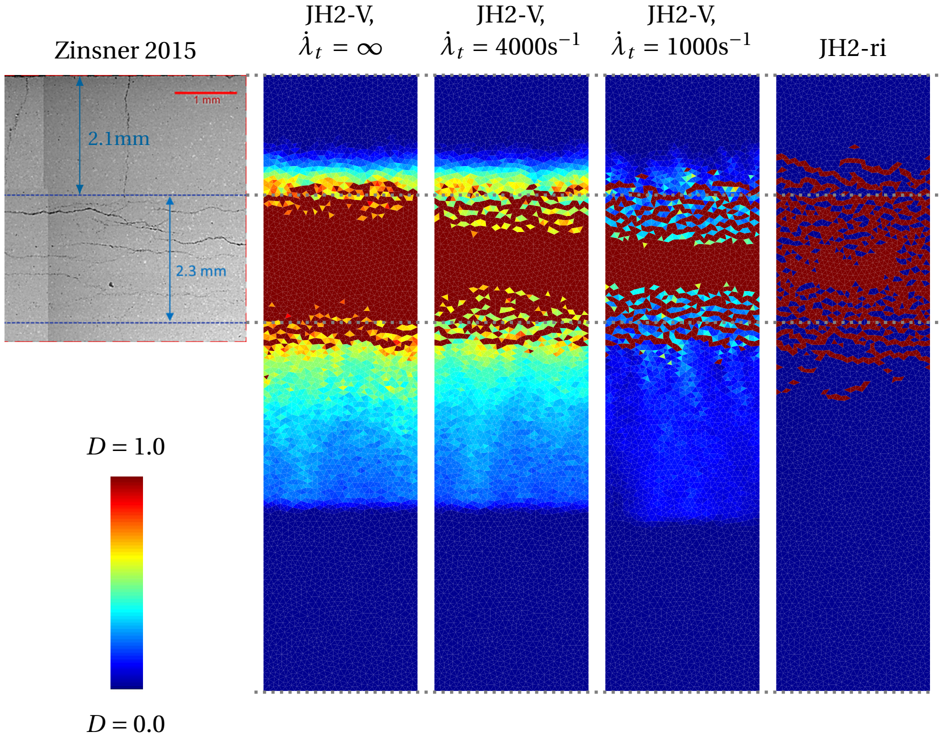

Figure 2.30: Spall failure zones in experiment (from [33]) and simulations compared. Simulation results show the damage variable $D \in [0..1]$. The JH2-V model results are obtained with $\eta = 0.028 \cdot 10^{-3}$ GPa·s and varying values of the threshold rate $\dot{\lambda}_t$.

lem. When exposed to loading rates ranging over multiple orders of magnitude the predicted failure zone is found to grow fast. In reality a failure zone may not grow as fast, or not at all if the loading rate is increased. To control the failure zone size a combined linear/logarithmic viscosity formulation was proposed. The combined linear/logarithmic apex viscosity was found to limit the failure zone size for higher loading rates while still providing mesh independent results for the range of loading rates considered here. The linear viscosity formulation is found to be a limit case of the mixed linear/logarithmic formulation. Hence the mixed linear/logarithmic formulation is recommended for general use.

As a final step the physical implication of the proposed rate dependent apex pressure was tested by simulating a spall experiment on alumina ceramic. The apex viscosity was found to correctly capture the rate dependent spall strength of the ceramic. The original JH2 material model failed to capture this rate dependency.

REFERENCES

[1] E. C. Simons, J. Weerheijm, and L. J. Sluys, *A viscosity regularized plasticity model for ceramics,* European Journal of Mechanics / A Solids **72**, 310 (2018).

[2] P. J. Hazell, *Ceramic Armour: Design and Defeat Mechanisms* (Argos Press, Canberra, 2006).

[3] S. M. Walley, *Historical review of high strain rate and shock properties of ceramics relevant to their application in armour,* Advances in Applied Ceramics **109**, 446 (2010).

[4] Z. Rosenberg and E. Dekel, *Terminal ballistics,* 2nd ed. (Springer-Verlag, Heidelberg, 2012).

[5] T. J. Holmquist and G. R. Johnson, *The failed strength of ceramics subjected to high-velocity impact,* Journal of Applied Physics **104** (2008), 10.1063/1.2955456.

[6] D. Sherman and T. Ben-Shushan, *Quasi-static impact damage in confined ceramic tiles,* International Journal of Impact Engineering **21**, 245 (1998).

[7] G. Subhash, S. Maiti, P. H. Geubelle, and D. Ghosh, *Recent Advances in Dynamic Indentation Fracture, Impact Damage and Fragmentation of Ceramics,* Journal of the American Ceramic Society **91**, 2777 (2008).

[8] A. A. Wereszczak, T. P. Kirkland, K. T. Strong, T. J. Holmquist, and D. S. A, *ORNL Quasi-Static Mechanical Characterization and Analysis : FY09 Annual Report to TARDEC Under contract DE-AC05-00OR22725,* Tech. Rep. (Oak Ridge National Laboratory, 2009).

[9] B. G. Compton, E. A. Gamble, and F. W. Zok, *Failure initiation during impact of metal spheres onto ceramic targets,* International Journal of Impact Engineering **55**, 11 (2013).

[10] J. Wade, S. Robertson, and H. Wu, *Plastic deformation of polycrystalline alumina introduced by scaled-down drop-weight impacts,* Materials Letters **175**, 143 (2016).

[11] K. A. Iyer, *Relationships between multiaxial stress states and internal fracture patterns in sphere-impacted silicon carbide,* International Journal of Fracture **146**, 1 (2007).

[12] T. J. Holmquist and A. A. Wereszczak, *Using Hertzian Indentation to Understand the Strength and Ballistic Resistance of Silicon Carbide,* International Journal of Applied Ceramic Technology **7**, 625 (2010).

[13] J. Wade, S. Ghosh, P. Claydon, and H. Wu, *Contact damage of silicon carbide ceramics with different grain structures measured by Hertzian and Vickers indentation,* Journal of the European Ceramic Society **35**, 1725 (2015).

[14] K. P. Marimuthu, F. Rickhey, J. H. Lee, and H. Lee, *Spherical indentation for brittle fracture toughness evaluation by considering kinked-cone-crack,* Journal of the European Ceramic Society **37**, 381 (2016).

[15] G. R. Johnson and T. J. Holmquist, *A computational constitutive model for brittle materials subjected to large strains, high strain rates, and high pressures,* Shock Wave and High-Strain-Rate Phenomena in Materials (1992).

[16] G. R. Johnson and T. J. Holmquist, *An improved computational constitutive model for brittle materials,* AIP Conference Proceedings **309**, 981 (1994).

[17] G. R. Johnson, T. J. Holmquist, and S. R. Beissel, *Response of aluminum nitride (including a phase change) to large strains, high strain rates, and high pressures,* Journal of Applied Physics **94**, 1639 (2003).

[18] C. Simha, S. Bless, and A. Bedford, *Computational modeling of the penetration response of a high-purity ceramic,* International journal of impact engineering **27**, 65 (2002).

[19] A. Rajendran, *High Strain Rate Behavior of Metals Ceramics, and Concrete*, Tech. Rep. (University of Dayton Research Institute, Dayton, Ohio, 1992).

[20] Q. Zuo, F. Addessio, J. Dienes, and M. Lewis, *A rate-dependent damage model for brittle materials based on the dominant crack,* International Journal of Solids and Structures **43**, 3350 (2006).

[21] V. S. Deshpande and A. G. Evans, *Inelastic deformation and energy dissipation in ceramics: A mechanism-based constitutive model,* Journal of the Mechanics and Physics of Solids **56**, 3077 (2008).

[22] V. S. Deshpande, E. A. N. Gamble, B. G. Compton, R. M. McMeeking, A. G. Evans, and F. W. Zok, *A Constitutive Description of the Inelastic Response of Ceramics,* Journal of the American Ceramic Society **94**, s204 (2011).

[23] Z. P. Bazant and F.-B. Lin, *Non-local yield limit degradation,* International Journal for Numerical Methods in Engineering **26**, 1805 (1988).

[24] N. Fleck and J. Hutchinson, *Strain Gradient Plasticity,* (1997).

[25] A. Needleman, *Material rate dependence and mesh sensitivity in localization problems,* Computer Methods in Applied Mechanics and Engineering **67**, 69 (1988).

[26] A. Winnicki, C. J. Pearce, and N. Bićanić, *Viscoplastic Hoffman consistency model for concrete,* Computers and Structures **79**, 7 (2001).

[27] M. Lazari, L. Sanavia, and B. Schrefler, *Local and non-local elasto-viscoplasticity in strain localization analysis of multiphase geomaterials,* International Journal for Numerical and Analytical Methods in Geomechanics **39**, 1570 (2015), arXiv:nag.2347 [10.1002] .

[28] P. Perzyna, *Fundamental Problems in Viscoplasticity,* Advances in Applied Mechanics **9**, 243 (1966).

[29] G. Duvaut and J.-L. Lions, inequations en mecanique et en physique [Les] (1976).

[30] W. Wang, L. Sluys, and R. De Borst, *Viscoplasticity for instabilities due to strain softening and strain-rate softening,* International Journal for Numerical Methods in Engineering **40**, 3839 (1997).

[31] J. C. Simo, J. G. Kennedy, and S. Govindjee, *Non-smooth multisurface plasticity and viscoplasticity. Loading/unloading conditions and numerical algorithms,* Int J Numer Meth Eng **26**, 2161 (1988).

[32] Dynaflow Research Group, *Jem-jive,* http://jem-jive.com.

[33] J. L. Zinszner, B. Erzar, P. Forquin, and E. Buzaud, *Dynamic fragmentation of an alumina ceramic subjected to shockless spalling: An experimental and numerical study,* Journal of the Mechanics and Physics of Solids **85**, 112 (2015).

[34] J.-l. Zinszner, B. Erzar, and P. Forquin, *Strain rate sensitivity of the tensile strength of two silicon carbides : experimental evidence and micromechanical modelling,* Philosophical transactions A (2017).

[35] E. C. Simons, J. Weerheijm, and L. J. Sluys, *Fully Implicit Plasticity Model for the Characterization of Ceramics in Ballistic Protection,* in *22nd Technical Meeting DYMAT 'Experimental Testing and Modelling of Brittle Materials at High Strain-Rates'* (Grenoble, 2016) pp. 17–22.

[36] M. A. Crisfield, *Non-Linear Finite Element Analysis of Solids and Structures: Essentials* (John Wiley & Sons, Inc., New York, NY, USA, 1991).

[37] M. Jirásek, *Mathematical analysis of strain localization,* Revue fran{ç}aise de g{é}nie civil **11**, 977 (2007).

[38] *Astm*, Tech. Rep. D5607-02 (International, ASTM, 2002).

[39] T. J. Hughes, *Generalization of Selective Integration Procedures to Anisotropic and Nonlinear Media,* Short Communications , 1413 (1980).

[40] Z. P. Bažant and M. Jirásek, *Nonlocal Integral Formulations of Plasticity and Damage: Survey of Progress,* Journal of Engineering Mechanics **128**, 1119 (2002).

3

SIMULATING BRITTLE AND DUCTILE RESPONSE OF ALUMINA CERAMICS UNDER DYNAMIC LOADING

3.1. INTRODUCTION

Ceramic materials such as alumina and silicon carbide are widely used in armour systems. These ceramics have a high hardness and relatively low weight when compared to traditional armour materials such as steel. The high hardness of the ceramic ensures heavy deformation and even fracturing of incoming projectiles. The ceramic material itself may also damage during this interaction. As long as the ceramic can exert a force on the projectile, the deformation and deceleration of the projectile continues. Understanding the failure process of a ceramic material is therefore key in understanding the projectile/armour interaction [2–4]. Armour ceramics show multiple modes of failure. Under tension the behaviour is brittle, while a more ductile behaviour can be found under compression. The brittle nature under tensile loading is attributed to macro crack formation. While the ductile behaviour of the ceramics under compression can be explained by micro-crack formation and plasticity. Plastic deformation of ceramics under impact is well known and appears for sufficiently high confining pressures [5–9].

Although the main modes of failure are known for armour ceramics it is still difficult to properly capture their behaviour, the sequence of occurrence and the interaction of mechanisms with a computational model. Experimental measurements of the individual failure processes are very limited. True impact experiments with projectiles can be

---

This chapter is based on [1]

performed, but material behaviour is often deducted rather than measured. The latter is difficult due to highly varying stress states and the catastrophic nature of the experiments. There are two main paths one can take to better understand the failure process. The first way is to limit the loading rates, and therefore consider quasi-static indentation tests [10, 11] and slow dynamic testing such as drop-weight impact tests [8]. The main advantage of these tests is that the ceramic does not fail catastrophically. This makes it possible to examine intermediate stages of failure which lie between intact and fully failed. A second way to study ceramic failure is by simplifying the dynamic loading, e.g. by plate impact or spall tests. In these experiments the material is loaded in a well defined way, which makes it possible to deduce the material behaviour under these dynamic loading scenarios. When building a constitutive model for ceramics this type of information is essential. The main advantage of the second type of tests over the first one is that the dynamic nature of the impact problem is maintained, which is why the second approach is adopted in this chapter.

Plate impact tests have been performed on ceramic materials over the past decades, providing a great deal of information in literature [12–21]. In a plate impact experiment high pressures can be reached and the material fails under compressive loading. The material is loaded in uniaxial strain and by measuring the free surface velocity of the impacted plate the stress wave inside the material can be reconstructed. This stress wave signal can then be used to derive material behaviour. Spall tests provide a second simplified loading scenario. Two types of spall tests can be performed, either a slender bar [22–25] of ceramic or a wide plate [26–28] is loaded. Similar to plate impact a spall test performed on a plate will load the material in uniaxial strain conditions, but in the spall test the target material fails under tension.

The plate impact and spall tests provide good insight in the material behaviour under pure compressive or tensile loading. This information can be used to calibrate or validate a constitutive model. The constitutive model should be able to capture the behaviour of the ceramic for both tests. This means that the model should be able to capture the brittle and ductile behaviour under tension and compression. Multiple constitutive models for ceramics have been proposed in literature over the past decades. Noteworthy models are those by Johnson and Holmquist [29–31], Simha [32] and Deshpande-Evans [33, 34]. Most of the available ceramic material models are essentially softening plasticity models. The main difference lies in the description of the material strength and the way the models deal with ceramic failure. In the current thesis the second model by Johnson-Holmquist [30] (JH2) is chosen as this is an often used and widely accepted ceramic material model for ballistic impact.

Softening plasticity models (such as the JH2 model) are well known to suffer from mesh dependency. In [35] a modification of the JH2 model was proposed which solved this mesh dependency. The modification consisted of the inclusion of rate dependency (i.e. viscosity) on the hydrostatic tensile strength of the material. Adding a viscosity to a constitutive model is known to provide an implicit length scale, which can regularize the solution and solve the mesh dependency problem [36–38]. In addition to providing mesh independency for the JH2 model results it was seen that the rate dependency of the tensile strength allowed the model to properly capture experimentally measured rate dependency of the spall strength of ceramic [27], where the original JH2 model failed to do so.

The goal of the current chapter is to find a generic model, capable of simulating ceramic failure both under tension and compression, subjected to a range of loading rates. The viscosity regularized JH2 model (JH2-V) from [35] is used as a starting point. This model will be described in Section 3.2. In Section 3.3 the JH2-V model (and the original JH2 model) will be extensively tested. The models will be used to simulate a spall test, a plate impact tests, a sphere impact test and a quasi-static ring-on-ring bending test. For a correct material model all of these tests should give an adequate match between experiments and simulations, for a single set of model parameters. Unfortunately the analysis shows that this is not true for the JH2-V model (or the JH2 model). Fortunately the simulation results give a clear indication that this is related to the failure formulation of the model. The failure formulation in these models only allows for either brittle failure under tension or ductile failure under compression. This is because the damage rate in the failure formulation is a single pressure dependent function, coupling the behaviour under tension and compression through the model parameters. In section 3.4 the failure formulation is modified such that the failure response under tension and compression is separated. This allows independent control over the damage rate under tensile and compressive loading. Calibration of the new formulation is done based on spall and plate impact tests. It is shown that the JH2-V model with the new softening formulation can properly capture the ceramic's behaviour in all four considered loading scenarios, for a single set of model parameters.

3.2. METHODS AND MODELS

Finite element (FE) simulations are performed. For the FE simulations a C++ based code is used, developed with the open source FE libraries provided by JemJive[39]. Implicit solution schemes are used for the simulations in this thesis, Newton-Raphson for the quasi-static simulations and Hilbert-Hughes-Taylor-α for the dynamic simulations.

The choice for this numerical framework will be briefly explained by two comments. First a comment on the FE method. This is a well established method to solve a partial differential equation (PDE). Other methods may also be used, such as the material point method (MPM) [40, 41], smooth particle hydrodynamics (SPH) [42–46] and many others. These methods may have some advantages and disadvantages over the FE method. One major advantage of MPM and SPH is that these mesh-less methods easily deal with large deformations, but they tend to be more computationally heavy than FEM. Since the test cases in the current chapter do not experience large deformation the FE method remains a good choice. The second comment is on the choice for the implicit time integration scheme. Compared to explicit time integration schemes these implicit schemes have two main advantages. The first is that the balance of linear momentum is exactly satisfied in each time step, which is not true for explicit schemes. The second advantage is that these implicit schemes are unconditionally stable, and as such do not have a critical time step. This means time steps can be much larger than what is possible in explicit time integration schemes. This feature is further exploited in the current thesis by using an adaptive time integration scheme, to keep the implicit scheme robust and fast. The Hilbert-Hughes-Taylor-α method furthermore has some damping included in its formulation, which may help when simulating dynamic contact problems [47]. The choice of how one solves the PDE and how one deals with time integration is independent of the material model. The constitutive model developed in the current chapter should therefore be considered as a general model, not bound by the FEM or implicit time integration.

In the current thesis the Johnson-Holmquist-2 [30] model is used, as this is a widely accepted material model for ceramics. The section will start with a short description of the material strength in this model, as well as the viscosity regularized formulation from [35]. The second part of the section will show how failure is captured in the ceramic material models JH2 and JH2-V, as well as several others.

3.2.1. MATERIAL STRENGTH

JOHNSON-HOLMQUIST-2

In the Johnson-Holmquist-2 (JH2) model the yield function f of the material is described as

$$f(\boldsymbol{\sigma}, D) = \sigma_{eq}(\boldsymbol{\sigma}) - \sigma_y(\boldsymbol{\sigma}, D), \tag{3.1}$$

where $\boldsymbol{\sigma}$ is the stress tensor, D a scalar damage variable, σ_{eq} the Von Mises stress and σ_y the material strength. This material strength can be found as

$$\sigma_y^*(\boldsymbol{\sigma}, D) = (1 - D)\ \sigma_i^*(\boldsymbol{\sigma}) + D\,\sigma_f^*(\boldsymbol{\sigma}), \tag{3.2}$$

where * indicates that the values are normalized with respect to the equivalent stress at the Hugoniot elastic limit, i.e. σ_{HEL}. The material strength σ_y is an interpolation of the intact and residual strengths σ_i and σ_f with damage D. The intact and residual material strengths are a function of the pressure $p(\boldsymbol{\sigma}) = -\frac{1}{3}\sigma_{ii}$ and can be expressed as

$$\sigma_i^*(\boldsymbol{\sigma}) = A\left(\frac{T + p(\boldsymbol{\sigma})}{P_{HEL}}\right)^n \left(1 + C\ln\dot{\epsilon}_p^*\right), \tag{3.3}$$

$$\sigma_f^*(\boldsymbol{\sigma}) = B\left(\frac{p(\boldsymbol{\sigma})}{P_{HEL}}\right)^m \left(1 + C\ln\dot{\epsilon}_p^*\right). \tag{3.4}$$

Here A, B, C, n, m, T and P_{HEL} are material properties and $\dot{\epsilon}_p^*$ is the rate of equivalent plastic strain normalized with respect to reference rate $\dot{\epsilon}_0$. The rate dependency is controlled through parameter C. This rate dependency provides a deviatoric scaling of the material strength.

JOHNSON-HOLMQUIST-2 VISCOSITY-REGULARIZED

In [35] a modification to the JH2 model was proposed. To solve mesh dependency of the original model an apex viscosity was introduced (hence Johnson-Holmquist-2 viscosity-regularized or JH2-V). The material strengths from (3.3) and (3.4) are now replaced by

$$\sigma_i^*(\boldsymbol{\sigma}) = A\left(\frac{T(\dot{\epsilon}_p) + p(\boldsymbol{\sigma})}{P_{HEL}}\right)^n, \tag{3.5}$$

$$\sigma_f^*(\boldsymbol{\sigma}) = B\left(\frac{p(\boldsymbol{\sigma})}{P_{HEL}}\right)^m. \tag{3.6}$$

In this formulation the apex pressure T is now a function of rate, providing a rate dependent tensile strength to the material. In the above formulations the original logarithmic rate dependency is absent, however the new formulation does not exclude the original formulation as both formulations may be used together.

The proposed apex viscosity is a mixed linear/logarithmic formulation

$$T(\dot{\bar{\epsilon}}_p) = T(\dot{\lambda}) = \begin{cases} T_0 + \eta\dot{\lambda} & \text{for } \dot{\lambda} < \dot{\lambda}_t, \\ T_t\left(1 + \frac{\eta\dot{\lambda}_t}{T_t}\ln\left(\frac{\dot{\lambda}}{\dot{\lambda}_t}\right)\right) & \text{else.} \end{cases} \tag{3.7}$$

Here, $\dot{\lambda}$ is the rate of plastic multiplier, which is equal to the rate of equivalent plastic strain when using a deviatoric plastic flow rule. Furthermore, T_0 is the rate independent apex pressure, η is the viscosity and $\dot{\lambda}_t$ is the threshold rate for which the viscosity changes from linear to logarithmic. A transition pressure $T_t = T_0 + \eta\dot{\lambda}_t$ is also used in the formulation. The mixed linear/logarithmic formulation was found to provide mesh-independent results. In addition it was shown that the proposed viscosity formulation could match experimentally measured rate dependency of the spall strength of ceramics. The original strength formulation of the JH2 model failed to have mesh-independent results and also failed to capture the rate dependency in the spall strength.

3.2.2. CERAMIC SOFTENING

A strength reduction in the JH2 and JH2-V models is achieved by the damage parameter D, as is shown in (3.2). This single damage parameter should be able to properly describe the underlying failure phenomena. This may be challenging since the failure behaviour of a ceramic under tension and compression can be very different. In this subsection damage growth of the JH2 model is compared to other models.

JOHNSON-HOLMQUIST-2

In the JH2 model failure is a gradual process, where the yield stress reduces as the damage parameter D grows (as shown in (3.2)). The rate of damage is found as

$$\dot{D} = \frac{\dot{\bar{\epsilon}}_p}{\bar{\epsilon}_p^f}, \tag{3.8}$$

where $\dot{\bar{\epsilon}}_p$ is the rate of equivalent plastic strain and $\bar{\epsilon}_p^f$ is the plastic failure strain, for which the material is fully failed. The failure strain is not constant in the JH models but follows

$$\bar{\epsilon}_p^f(\boldsymbol{\sigma}) = d_1\left(\frac{T + p(\boldsymbol{\sigma})}{P_{HEL}}\right)^{d_2}, \tag{3.9}$$

where d_1 and d_2 are material constants. The values of d_1 and d_2 are typically unknown for a ceramic, because direct measurement of plastic failure strain in ballistic experiments is currently impossible. The functional form of the failure strain formulation in (3.9) is therefore an assumption and the parameters are determined through inverse modelling. Table 3.1 lists some of the failure related properties used in literature when modelling alumina ceramic. The material density is added to give insight in the type of alumina ceramic considered in these sources. The difference between highest and lowest values for d_1 and d_2 is found to be one order of magnitude. This great diversity is a clear indication of their level of uncertainty.

Table 3.1: JH2 failure strain constants for alumina ceramics

d_1	d_2	$\rho\ [kg/m^3]$	source
0.002	0.83	3625	[48]
0.005	0.83	3625	[49]
0.005	1.00	3700	[50]
0.010	1.00	3800	[51]
0.001	1.00	3890	[52]
0.010	0.07	3890	[53]
0.0125	0.70	3890	[54]

In the JH2 formulation the failure strain for $p < T$ is zero and failure is instantaneous. In the JH2-V model the rate dependent material strength allows for the material to reach $p < T$. However, if the JH2 failure strain is used this will still result in sudden failure. Tensile failure in ceramic material is related to fracture and thus crack propagation. Crack propagation is known to occur at a finite and limited velocity. This argues against the sudden failure found in the JH2 softening formulation. A simple modification can be made to (3.9) to ensure a finite rate of damage and at the same time allow pressure beyond the apex pressure. The failure strain formulation is changed to read

$$\bar{\epsilon}_p^f(\boldsymbol{\sigma}) = \max\left(d_1\left(\frac{T + p(\boldsymbol{\sigma})}{P_{HEL}}\right)^{d_2}, \bar{\epsilon}_p^{f,min}\right), \tag{3.10}$$

where $\bar{\epsilon}_p^{f,min}$ is a small but non-zero failure strain value. Please note that this is not the 'modified formulation' of the failure strain as mentioned in the introduction. Equation (3.10) is merely a fix to allow the failure strain to exist for pressures below the apex pressure. This is the formulation used to perform the initial comparative analyses in Section 3.3. Later in Section 3.4 a completely new failure strain formulation will be proposed to improve the model results.

OTHER CERAMIC MODELS

The way the JH2 model deals with a reduction of strength is not unique. There are other softening plasticity models for ceramics which use similar approaches. For instance the closely related Johnson-Holmquist-1 (JH1) and the Johnson-Holmquist-Beissel (JHB) model, as presented in [29] and [31], respectively. These models use the same damage parameter as the JH2 model. However, the gradual interpolation of the material strengths is not present in the JH1/JHB models. Instead, for these models an intact strength is maintained until full failure is reached at $D = 1.0$, at which there is a sudden transition to the residual strength. This approach essentially means that the ceramic behaves perfectly plastic, with one sudden reduction of strength as full damage is reached.

Another approach is found in the Deshpande-Evans-2 (DE2) model [34]. In this model there are three distinct failure mechanisms incorporated. Depending on the triaxiality $\zeta = \sigma_m/\sigma_e$, with mean stress σ_m and equivalent stress σ_e, cracks grow: in pure

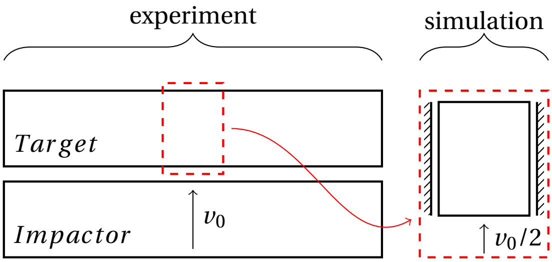

Figure 3.1: Plate impact experiment and simplified model. Due to the axial loading nature the problem can be simplified to a column of material, subjected to some applied velocity on its lower edge. In plate impact the impactor arrives with initial velocity v_0 and impacts on the target material, generating $v(t) = 0.5v_0$ if both materials are the same. Methods other than impact can also be used to apply a velocity profile, such as the "shockless spall" method from [27].

tension, in tension/shear or do not grow. In this model the rate of damage increases as the stress state is closer to hydrostatic tension. Also interesting to note is that a hardening response is found for high compressive stress states.

A third approach is found in the material model by Simha [32]. In this model again three domains are identified, based on the principal stress in the material. The rate of damage is then determined by the number of principal stresses in tension, as well as the magnitude of the largest principal tensile stress. The difference between damage rate for compression and hydrostatic tension is even in the order of 10^4.

3.3. JH2-V MODEL ANALYSIS

In the previous section multiple models for the failure behaviour of ceramics have been presented. In the current section the JH2-V model with the original JH2 failure strain formulation from (3.10) is examined. The model is validated with four different experimental tests: Spall, plate impact, sphere impact and quasi-static ring-on-ring bending. If the JH2-V material model is valid, it should be able to match experimental results in all four tests, for a single set of model parameters. This thorough analysis is meant to challenge and critically analyse the current material model. It will reveal shortcomings of the material model. Based on the analysis in the current section an improved model will be proposed in Section 3.4.

One comment should be made in advance regarding the experiments in this section. The experimental results are obtained from literature. These experiments have all been performed on a similar high purity alumina ceramic. In an ideal scenario they should have been performed on the exact same material, but unfortunately no such data set is available. Small variations in the material properties are therefore expected and have to be accepted.

3.3.1. SPALL SIMULATIONS

Spall experiments on plate material are typically performed by impact. One plate of material is given an initial velocity (the "impactor") and impacts a plate of the same material (the "target"), as is shown in Figure 3.1. The impacting plate generates a shockwave, which can lead to spall failure in the target material. The free surface velocity of the target plate can be measured to determine the spall strength of the material. Given that the lateral dimensions of the plates are much larger than the thickness, the central part of the plate experiences uniaxial strain. The problem can thus be simplified to a single column of material, with an axial velocity applied to the bottom surface. This is also shown in Figure 3.1, by the red dashed box.

Spall experiments on AL23 high purity alumina ceramics have been performed by Forquin's group [27]. These spall experiments were performed on alumina plates, but the stress wave was induced through an electromagnetic device rather than impact. This allows for the generation of a more controlled stress wave, or as the authors state a "shockless" spalling. In Chapter 2 this experiment was simulated using the JH2 and JH2-V material models. It was found that the original JH2 model with or without rate dependency fails to capture the rate effect under tension, while the JH2-V model is able to capture the rate dependency measured in the spall strength of alumina ceramic. The current section briefly describes the simulations and results for the JH2-V model. The material properties from Table 3.2 in the column 'Spall value' are used in the simulations. These properties are based on [27], complemented by typical alumina values for the JH2 model from literature. Note that a minimal failure strain is imposed through equation (3.10) to allow a pressure below the (static) apex pressure T.

The spall test is simulated as a 10mm long and 2.5mm wide column, using linear three noded triangular elements under plane strain. The mesh is unstructured with element size $h \approx 0.1$mm. A velocity is prescribed on the bottom of the column, while the top remains free to move. As mentioned before, the sides of the column are constrained from lateral movement. The applied velocities in the experiments are known. Idealized applied velocity profiles are presented in Figure 3.2a, which are the velocities applied in the simulations.

The predicted spall strength as a function of rate is shown in Figure 3.2b. The spall strength is defined as the highest axial stress found when apex failure is first experienced. The rate is the total axial strain rate experienced by the point of maximum stress at this moment. From the graph it is clear that a viscosity formulation with $\eta = 0.028 \cdot 10^{-3}$ GPa·s and $\dot{\lambda}_t = \infty$ is sufficient to capture the rate effect of the spall strength. For $\eta = 0.000$ GPa·s the rate independent JH2 formulation is retrieved. It can be seen that this model fails to capture the rate dependency. The rate independent model results are similar to the stress at which a yield surface is reached under tension, which is the 'theoretical' strength in Figure 3.2b.

Figure 3.3 holds both the experimental and numerical predicted failure in the spall tests. Experimentally the ceramic could only be recovered from a single test. In this test the material was subjected to a wave similar to wave 2 from Figure 3.2a. The failure zones predicted in both simulations agree well with the experiment. The JH2-V model with zero viscosity shows a discrete failure pattern, typical for a material model suffering from mesh dependency. The viscous JH2-V model shows a more smooth damage profile, with intermediate values between intact and fully failed. Furthermore the viscous case shows damage extending beyond the experimentally observed failure zone. Whether this is also the case in the experiment is unknown, but the simulations performed in [27] also show non-zero crack densities beyond the cracked zone.

Table 3.2: JH2-V material properties used in simulations, based on [27] and complemented by typical alumina values for the JH2 model from literature. The initial model values are found in the column 'Spall value'. Modified parameter sets are found in the other columns, where bold face notation is used for the parameters different from the spall value.

variable	unit	Spall	Plate impact	variation 1	variation 2	variation 3	variation 4
		value	value	value	value	value	value
E	GPa	360.0	**380.0**	**380.0**	**380.0**	**380.0**	360.0
ν	-	0.22	0.22	0.22	0.22	0.22	0.22
ρ	kg/m^3	3850	**3890**	**3890**	**3890**	**3890**	3850
A	GPa	0.930	0.930	0.930	0.930	0.930	0.930
B	GPa	0.310	0.310	**0.810**	0.310	0.310	0.310
n	-	0.6	0.6	0.6	0.6	0.6	0.6
m	-	0.6	0.6	0.6	0.6	0.6	0.6
C	-	0.0	0.0	0.0	0.0	0.0	0.0
T	GPa	0.2	0.2	0.2	0.2	0.2	0.2
η	GPa·s	$2.8{\cdot}10^{-5}$	$2.8{\cdot}10^{-5}$	$2.8{\cdot}10^{-5}$	$2.8{\cdot}10^{-5}$	$2.8{\cdot}10^{-5}$	$2.8{\cdot}10^{-5}$
$\dot{\lambda}_t$	s^{-1}	∞	∞	∞	$\mathbf{4\cdot 10^4}$	$\mathbf{4\cdot 10^4}$	∞
HEL	GPa	6.25	6.25	6.25	6.25	6.25	6.25
P_{HEL}	GPa	3.50	**3.25**	**3.25**	**3.25**	**3.25**	3.50
σ_{HEL}	GPa	4.125	**4.50**	**4.50**	**4.50**	**4.50**	4.125
d_1	-	0.005	0.005	0.005	**0.050**	**0.500**	**0.500**
d_2	-	0.75	0.75	0.75	0.75	0.75	0.75
$\bar{\epsilon}_p^{f,min}$	-	$1.5\cdot 10^{-4}$	$1.5\cdot 10^{-4}$	$1.5\cdot 10^{-4}$	$1.5\cdot 10^{-4}$	$1.5\cdot 10^{-4}$	$1.5\cdot 10^{-4}$

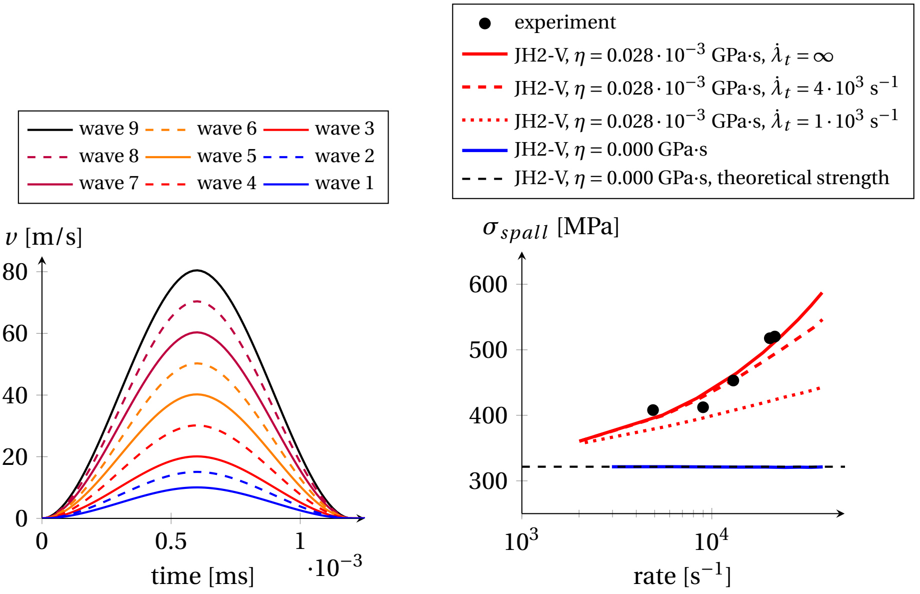

(a) Applied velocity to induce a stress wave in the spall simulations.

(b) Spall strength, experimentally measured and predicted by simulation. Without viscosity the JH2-V model is not able to capture the rate dependency, but it gives a good match with experiments when $\eta = 0.028 \cdot 10^{-3}$ GPa·s and $\dot{\lambda}_t = \infty$ are used.

Figure 3.2: Spall test on alumina ceramic, comparing experiments to simulations.

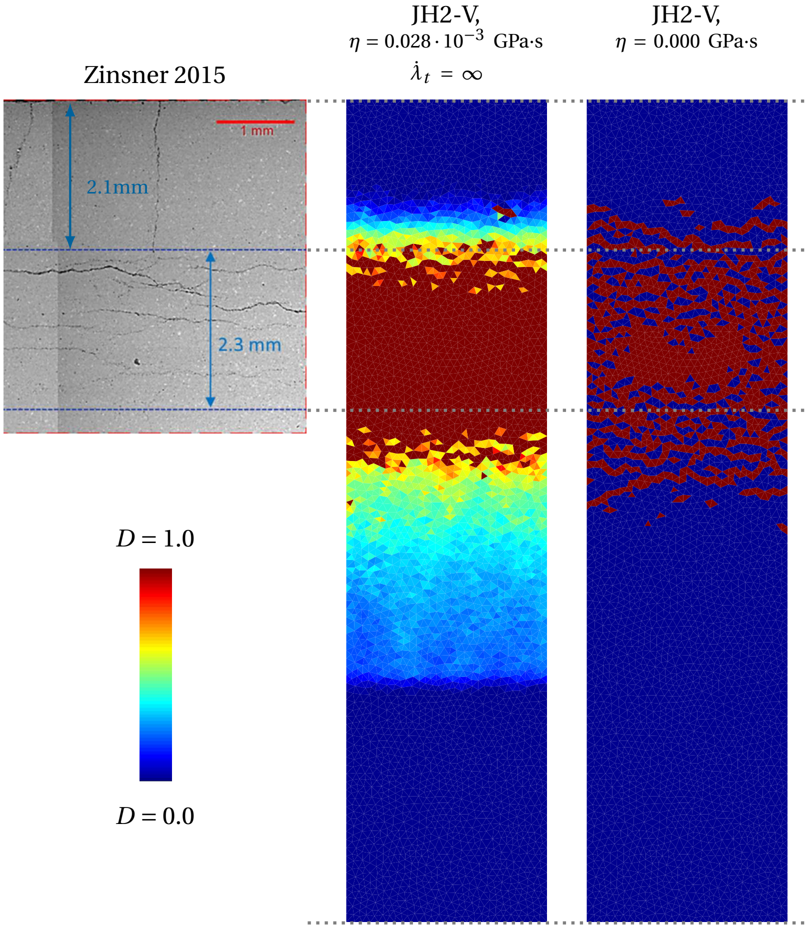

Figure 3.3: Damage profiles obtained in the spall experiment [27] and FE simulations. Stress wave 2 from Figure 3.2a is applied. The JH2-V material model with and without viscosity is compared.

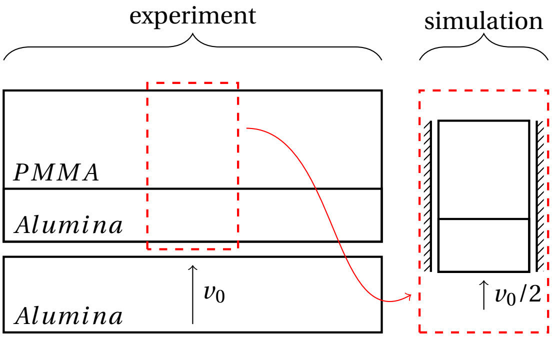

Figure 3.4: Plate impact experiment and simplified model. The alumina target material is backed by a PMMA plate. Due to the axial loading nature the problem can be simplified to a column of material, subjected to an applied velocity on its lower edge. In plate impact the impactor arrives with initial velocity v_0 and impacts on the target material, generating $v(t) = 0.5v_0$ if both materials are the same. Please note that the true thickness ratios are different from those depicted here.

SPALL - CONCLUDED

The spall simulations show that the rate dependent apex pressure in the JH2-V model allows to capture the rate effect under tension. The JH2 model fails to do so. This means that the apex viscosity is not only beneficial for regularization purposes, but it is also required in order to capture the (physical) rate dependent tensile strength.

3.3.2. PLATE IMPACT SIMULATIONS

The spall simulations from the previous section show that the viscosity regularized JH2 model works well for alumina ceramics. The spall strength as a function of loading rate could be captured and (as far as experimental data are available) the failure zone was also found to be correct. In the current section the material is tested under compressive loading. Again a plate impact experiment is simulated, this time with a sufficiently high stress to cause failure under compression.

In [55] results are reported for plate impact experiments on an aluminium oxide AD995, manufactured by the Coors Porcelain corporation. In these experiments a 5mm thick alumina flyer plate was given an initial velocity v_0. This flyer plate impacted a 10mm thick alumina target, which was backed by 25.4mm thick PMMA material. The impact velocity was such that the ceramic material failed under compression. The PMMA material was transparent, which allowed for a velocity measurement of the interface alumina/PMMA. This velocity signal at the interface contains information on the inelastic material behaviour. A schematic overview of the experiment is shown in Figure 3.4.

The plate impact experiment is simulated as a single column of four noded quadrilateral plane strain elements elements, with the JH2-V material model. A constant element size $h = 0.01$mm is used to mesh the column. A mixed Gauss integration scheme is used, where 2*2 integration is used for the deviatoric terms and 1 point integration for the hydrostatic terms [56]. Similar to the spall simulations the lateral movements of this column are constrained, while axial motion is allowed. The flyer plate is not modelled, instead a sudden velocity is applied on the target ceramic with a magnitude of half the flyer plate velocity. This generates a sudden shock wave in the ceramic target material, which will propagate as a stress wave. This idealized plate impact experiment is also shown on the right side in Figure 3.4.

The plate impact experiments in [55] report a material density of 3890kg/m3, which is slightly higher than what was used in the spall experiments (i.e. 3850kg/m3). Also the material stiffness is higher, 380GPa in the plate impact and 360GPa for the spall test. It is important to correct these values as they affect the wave speed in the material, which will in turn affect the interface velocity measurement obtained from the plate impact test. When changing the elastic properties the shock related P_{HEL} and σ_{HEL} should also be modified, as these quantities are related to the HEL of the material through the elastic constants. In the spall and plate impact experiments $HEL = 6.25$GPa, which gives $P_{HEL} = 3.25$GPa and $\sigma_{HEL} = 4.5$GPa for the modified material stiffness. The full parameter set with modified values can be found in the column 'Plate impact' from Table 3.2.

Figure 3.5 shows the experimental and numerical results for plate impact. The graph shows the velocity as a function of time, measured at the ceramic/PMMA interface. The dotted lines show the experimental results while the solid lines are used for the simulation results. An elastic stress wave arrives at the interface at point “A” in the graph. The velocity is found to rapidly rise to point “B”. At this point the material behaviour changes from elastic to inelastic. This point is referred to as the Hugoniot elastic limit (HEL) of the material. After reaching the HEL the velocity continues to rise until a maximum velocity is reached at “C”. The behaviour between points “B” and “C” will be referred to as the post-HEL behaviour. This post-HEL behaviour holds information on the ceramic strength during inelastic deformation. After reaching point “C” the velocity remains constant until the material experiences unloading at “D”. This unloading is caused by wave reflection on the free surface of the flyer plate. In the simulations the focus lies on the loading behaviour (post-HEL, from “B” to “C”) and no unloading is applied. Simulations are therefore terminated after 2μs and the unloading behaviour is not captured.

The experimental and numerical results can be compared in Figure 3.5. The arrival time of the stress wave and the HEL are captured well, as are the peak plateau values for the first four impact velocities. However, the post-HEL behaviour shows a major mismatch between experiments and simulations. This mismatch will be investigated closer to find its origin.

CHANGING POST-HEL BEHAVIOUR

For plate impact tests the post-HEL behaviour is determined by the inelastic response of the ceramic material. When using a material model such as the JH2-V model this relates to the plastic deformation and softening of the material. The velocity profiles obtained from the simulations in Figure 3.5 indicate a rapid loss of material strength. The experiments show a smooth post-HEL behaviour, indicating that failure of the material is more gradual and strength is retained for a longer time. To introduce this effect in the JH2-V model the softening related parameter d_1 and the viscosity parameters η and $\dot{\lambda}_t$ are obvious choices. However, in the JH2-V model the material strengths (intact and residual) may also play a role. The intact strength can be directly obtained from experiments, thus is a known quantity. The residual strength of ceramics is less certain, hence its effect on the post-HEL behaviour will be considered, more specifically the effect of the B parameter from (3.6).

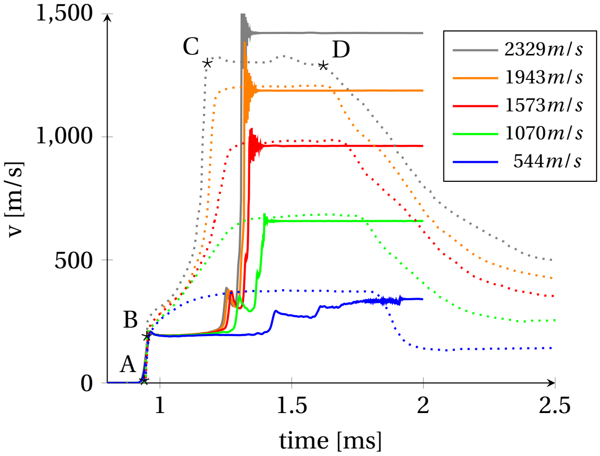

Figure 3.5: Simulation results for a plate impact test on alumina ceramic. The JH2-V model with the parameter set for the spall test is used, with a slightly increased material stiffness, density, P_{HEL} and σ_{HEL}. There is clearly a large difference in post-HEL behaviour. The dotted lines show the experimental results from [55], the solid lines are simulation results.

Figure 3.6 presents the velocity profiles for the spall test simulated with a larger residual strength. In the current results $B = 0.81$, while the previous results were obtained with $B = 0.31$. The current results show a closer agreement with the experiments. The post-HEL behaviour is now more smooth and also the peak plateau is reached at a time comparable to experiments. Although the post-HEL velocities are lower than the experimental values it can be found that increasing the B parameters improves the simulation results. It is however important to realize that there is almost no loss in strength for the chosen value of residual strength, as $B = 0.81$ lies close to the intact strength parameter $A = 0.93$. It is known that a ceramic pulverises under impact, which greatly reduces strength. So, although the plate impact results for simulations and experiments have a better match than before, it is not likely that this is a physically acceptable solution. There are other ways to retain a high material strength, such as a slower rate of damage.

The rate of damage in the JH2-V model is directly controlled by the failure strain formulation given in (3.9), as well as indirectly through the viscosity parameters η and $\dot{\lambda}_t$. The most obvious way of lowering the rate of damage is by increasing the d_1 parameter. Figure 3.7 shows the plate impact results for $d_1 = 0.050$, which is a factor ten larger than the $d_1 = 0.005$ used in the spall simulations. This higher value of d_1 makes the behaviour more ductile. For these results it is clear that the post-HEL gives a more smooth behaviour. The lowest two impact velocities seem to match well with the experimental results. However, for the highest three velocities the post-HEL curve is convexly shaped. Both the experimental results and the simulation with a higher B show a more concave response.

The convexly shaped simulation response of the highest three impact velocities indicate that the damage rate is now too slow for these cases. To speed up the rate of damage one can change the viscosity parameters. Since the viscosity η was already determined

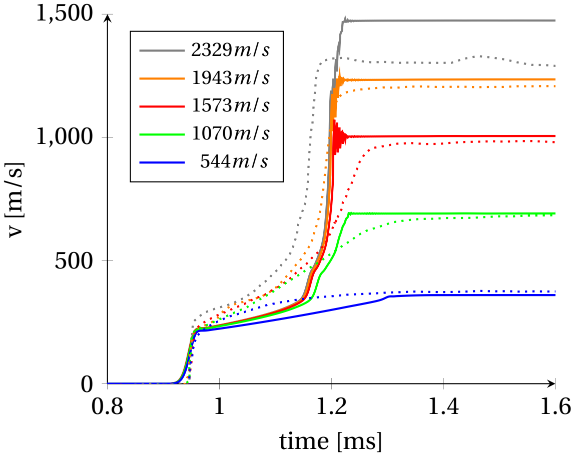

Figure 3.6: Simulation results for a plate impact test on alumina ceramic. The parameter set used to obtain Figure 3.5 was also used here, but the residual strength parameter B is now increased to $B = 0.81$. The post-HEL behaviour is now more smooth and the peak plateau arrival time is now also closer to the experimental values. The dotted lines show the experimental results from [55], the solid lines are simulation results.

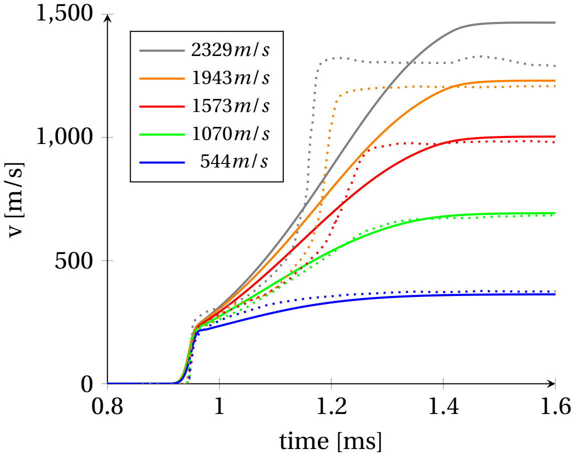

Figure 3.7: Simulation results for a plate impact test on alumina ceramic. The parameter set used to obtain Figure 3.5 was also used here, but with a softening parameter $d_1 = 0.050$. The dotted lines show the experimental results from [55], the solid lines are simulation results.

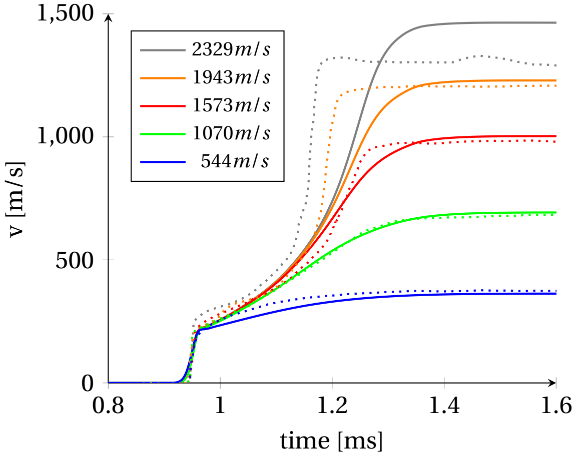

Figure 3.8: Simulation results for a plate impact test on alumina ceramic. The parameter set used to obtain Figure 3.5 was also used here, but with $d_1 = 0.050$ and $\dot{\lambda}_t = 40000\mathrm{s}^{-1}$. The dotted lines show the experimental results from [55], the solid lines are simulation results.

by the spall test, only the threshold rate $\dot{\lambda}_t$ can be altered. It is important to choose a threshold rate which leaves the lowest two velocities unaffected since they already show good agreement between simulations and experiments. After some parametric study a threshold value $\dot{\lambda}_t = 40 \cdot 10^3\ \mathrm{s}^{-1}$ was selected. This value is higher than the maximum rate experienced in the 1070m/s test, but below the maximum experienced rate in the 1573m/s test. Figure 3.8 holds the results for the new threshold rate. This new threshold is found to improve the results as the higher impact velocity results now show a more concave response in the post-HEL behaviour. The current value of the threshold rate does not pose a problem for the spall simulations, as the threshold rate of $\dot{\lambda}_t = 40 \cdot 10^3\ \mathrm{s}^{-1}$ is not reached during the spall simulations. Changing the threshold rate improves the simulation results. There is however still delay in the highest impact results compared to experiments, which can be found in the post-HEL behaviour as well as the peak plateau arrival time. Additional parametric study showed that the results can improve further by increasing the d_1 parameter once more to $d_1 = 0.500$. Results for this parameter set can be found in Figure 3.9. The parameter sets introduced in this section are also shown in Table 3.2 in the columns labelled 'variation 1, 2, 3'. Since none of these three parameter sets appears to be better than the other, a deeper investigation is required.

PLATE IMPACT CONCLUDED

When moving from spall simulations to plate impact simulations it was clear that the JH2-V model with a single set of material parameters was not able to properly predict both experiments. A major mismatch was found in the post-HEL behaviour of the material. The largest contributions were found to come from material softening, viscosity and the residual strength. Altering material properties resulted in a good match between experiments and simulations. However the residual strength had to be increased by a factor three and the failure strain even by a factor ten or hundred. These changes can

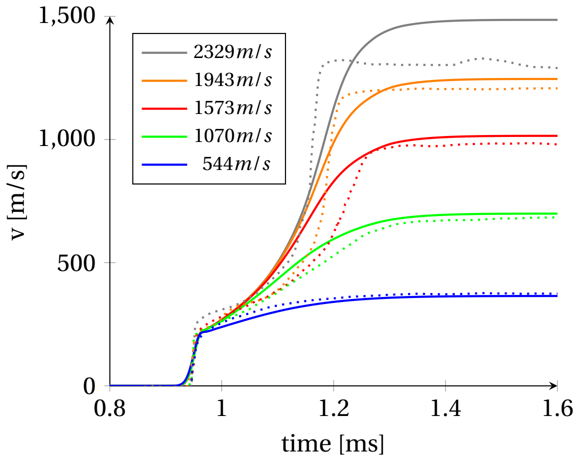

Figure 3.9: Simulation results for a plate impact test on alumina ceramic. The parameter set used to obtain Figure 3.5 was also used here, but with $d_1 = 0.500$ and $\dot{\lambda}_t = 40000\text{s}^{-1}$. The dotted lines show the experimental results from [55], the solid lines are simulation results.

no longer be explained by small differences in the tested materials. Hence, these large variation in the model parameters indicate that there is an inconsistency in the formulation. The current results do however not show if the mismatch is caused by the softening/viscosity or the residual material strength. In the next subsections additional tests will be performed to further investigate the origin of this mismatch.

3.3.3. SPHERE IMPACT

Two types of impact tests have been simulated and analysed so far. One in which failure occurred under tension (spall test) and one where failure occurred under compressive loading (plate impact). In both cases a dense alumina ceramic was used and an uniaxial deformation was imposed. These two extremes in loading condition did not give a unique answer in terms of material properties. In the current section a sphere impact test is simulated where the deformation is far from uniaxial and a wide range of stress states is encountered. Compression, tension and mixed mode loading will be found in this test, which can help revealing the correct material model behaviour.

In sphere impact experiments a projectile is given an initial velocity v_0 and impacts on a target material. This test is schematically shown in Figure 3.10. In the current section a steel projectile is assumed to impact on a ceramic target material. During this interaction both the projectile and target undergo (in)elastic deformation. Experimental results of sphere impact on alumina ceramic and silicon carbide ceramic are shown in Figures 3.11a, 3.11b and 3.11c. The figures show that the main mode of failure in the ceramic is cone cracking. The silicon carbide results also show a dark zone directly below the impact site. This is referred to as the quasi-plastic zone, which is characterized by micro-cracking and even plastic deformation. It is important to notice that the material in this subsurface zone is not pulverized. Although there is damage to the material the strength has not yet reduced to its minimum. This knowledge will prove vital in analysing

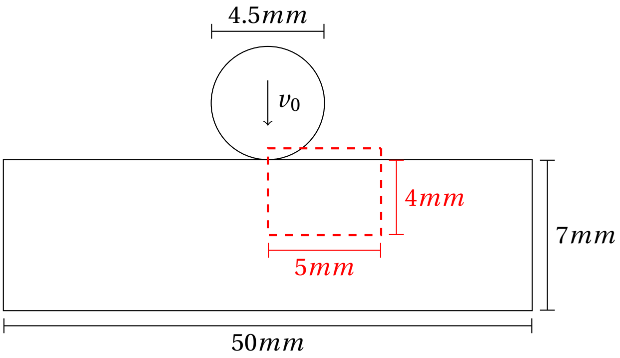

Figure 3.10: Sphere impact test, the projectile is given an initial velocity v_0. Geometry of the simulated problem is given. The red dashed box is the spatial domain in which the simulation results will be presented. Note that the figure does not show the true aspect ratios.

the sphere impact results.

The sphere impact experiment is simulated. The projectile is assumed to be a sphere with a diameter of 4.5mm, made of SAE51200 ball bearing steel. A Johnson-Cook material model was used to simulate this steel material, with a yield stress of 2.2GPa and hardening parameters from [59]. In the current simulations temperature and rate effects on the yield stress of the steel are ignored. The target is a ceramic plate with a thickness of 7mm and lateral dimension of 50mm (see Figure 3.10). The ceramic plate is not supported and without any material attached to the back surface. The ceramic material itself is a high density alumina ceramic, similar to the material previously considered in the spall and plate impact experiments. For the ceramic material the JH2-V model is used. As base model parameters the values from the plate impact test are chosen, as well as the three variations introduced in the previous section. These parameter sets can be found in Table 3.2 in the columns 'Plate impact' and 'variation 1,2,3'. The variations correspond to the parameter sets used to obtain the plate impact results from Figures 3.6, 3.8 and 3.9. The sphere impact experiment is simulated in a 2d axi-symmetric formulation, with the axis of impact as obvious axis of symmetry. Any lateral movement is constrained along this axis of symmetry and no other boundary conditions are applied to the system. As such the ceramic can be considered a free standing or unsupported target. Three noded linear elements are used to mesh this problem. The mesh is unstructured and the element size ranges from $h \approx 0.05$mm along the axis of impact to $h \approx 1.0$mm at the far side of the ceramic target. A penalty stiffness model with Coulomb friction ($\mu = 0.5$) is used to describe the contact between projectile and target.

Figure 3.12 shows the ceramic damage after sphere impact using four different parameter sets for the JH2-V model. The figures show only the material directly underneath the projectile corresponding to the dashed box shown in Figure 3.10. For all cases the alumina ceramic is impacted by a steel sphere with an initial velocity of 200m/s. The figures are taken after 1.4μs of simulated time. For the given tile thickness and elastic properties this is sufficient time for the initial pressure wave to travel to the back surface of the ceramic tile and return to the impact surface. This time is long enough to study the

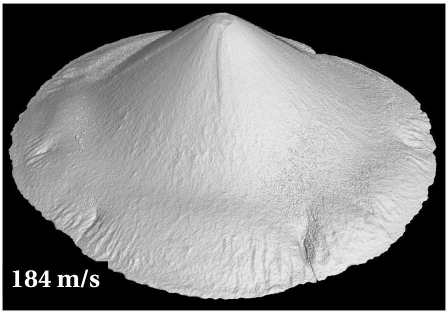

(a) An alumina ceramic cone, retrieved after a sphere impact experiment (E.P. Carton, TNO, personal communication, 2018). Figure was obtained by X-ray imaging (A. Thijssen, Delft University of Technology, personal communication, 2018).

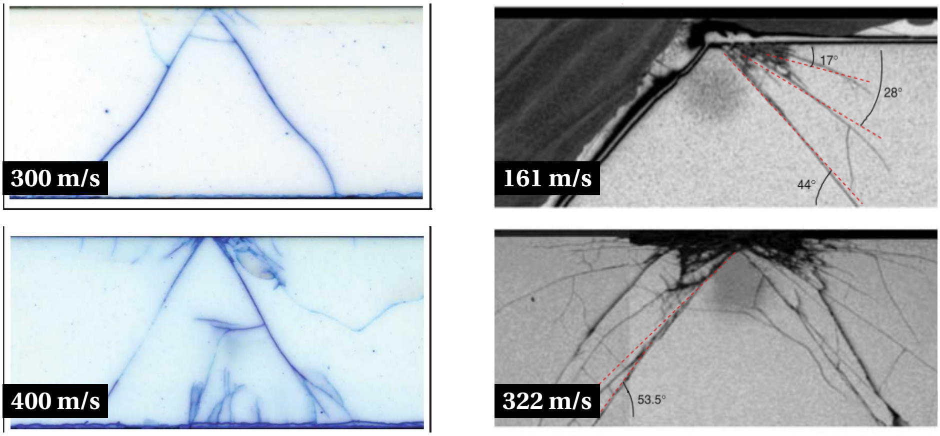

(b) Alumina ceramic after sphere impact, pictures are obtained from [57]. Comminution of ceramic directly below the projectile is absent.

(c) Silicon carbide ceramic after sphere impact, pictures are obtained from [58]. A quasi-plastic zone is found below the projectile, but the material is not comminuted.

Figure 3.11: Experimental results for a steel sphere impacting ceramic tiles. Top figure shows the result of impact on a ceramic plate without backing, the bottom figures are cross-sections of ceramic plates with backing after impact. Projectile velocities are shown. Cone cracking is clearly visible in all cases.

initiation of failure, but not enough to observe if the projectile is stopped by the ceramic. Although the latter is interesting from a practical point of view, the former is sufficient to investigate the previously found mismatch in parameters.

All cases show cone cracking (see Figure 3.12). However, the reference set and variation 1 of the model parameters both show a zone of fully failed material ($D = 1.0$) directly underneath the projectile. From (3.2) it can be found that these zones retain a strength under compression, but can no longer sustain any tensile loading. This is typical behaviour of fragmented material, which is what a ceramic is expected to be after full failure under compressive loading. Recall that full fragmentation was not observed in experiments (Figure 3.11), where some damage could be found underneath the projectile but the ceramic was not pulverized. This shows that the parameter set with a fast softening and the set with a high residual strength can not be correct. The variations 2 and 3, which have a slower softening than the reference set, provide a better match with experiments. Variation 2, with $d_1 = 0.050$, shows a cone crack as well as a (semi-) spherical zone of damage below the projectile. Although this is an improvement from the fully failed top layer found for a fast softening these results would still indicate a fully comminuted material. The best match with experiments is found for variation 3 with $d_1 = 0.500$, for which a clear cone crack forms. For this case minor damage is predicted below the projectile ($D \approx 0.01$), but the material is not fully failed as in the other cases. This minor damage is found from the figure as an ever so slightly light blue discolouration.

SPHERE IMPACT CONCLUDED

The plate impact and spall test have shown that it was impossible for the JH2-V model with a single parameter set to match both sets of experimental results. It was argued that both softening/viscosity or residual strength could be the reason for this mismatch. However, the spall and plate impact tests did not offer any certainty as to which option was the correct one.

Sphere impact was proposed as a third test case. This experiment is often performed on armour ceramics, where the main failure mechanism is cone cracking as well as some (incomplete) subsurface damage. Sphere impact simulations showed that these mechanisms could only be predicted for material with a slow softening and not for material with a high residual strength. So the sphere impact test has shown that the mismatch in earlier simulations and experiments was caused by the softening and viscosity.

For the plate impact experiment it was shown that slow softening is required. In the spall test a fast softening was assumed. However, it also would have been possible to use slow softening for the spall test and tune the viscosity accordingly. So, although the previous experiments have shown that there is some mismatch between experiments and simulations, the mismatch can still be solved by recalibration of the parameters. In the next section one more experiment is considered to investigate this behaviour.

3.3.4. RING ON RING

Three types of tests have been performed so far, namely a spall test with pure tensile loading, a plate impact test with pure compressive loading and a sphere impact test where a wide range of stress states including both tensile and compressive stresses. The

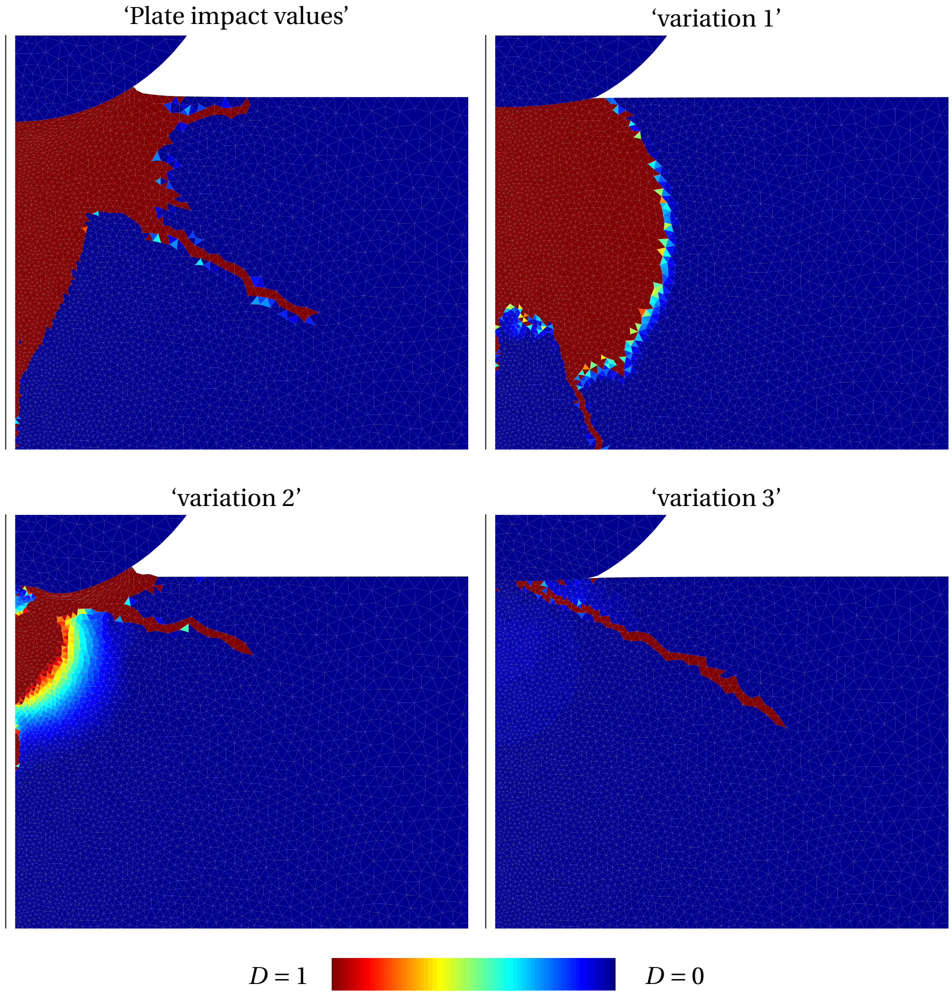

Figure 3.12: Sphere impact results for the JH2-V model. Damage variable $D \in [0..1]$ is shown after 1.4μs of simulated time.

results for these tests have shown an inconsistency in the material softening modelling. For the spall test a softening parameter $d_1 = 0.005$ was used, for which the material softening is fast and the response may be considered as being brittle. However, plate and sphere impact showed good agreement with simulations using $d_1 = 0.500$, for which the softening is slow and the response is more ductile. A possible solution to this inconsistency would be to increase the softening parameter for the spall test. In fact, the spall experiments could also be matched for $d_1 = 0.500$ by tuning the viscosity parameters. However, increasing d_1 would jeopardize the brittle response of ceramics under tension. This would be highly unwanted since the brittle nature of (armour) ceramic under tensile loading is a well accepted material trait.

A ring-on-ring (ROR) bending test is considered as final test. This is a tensile dominated test, where a disk of material is supported by a large ring on the bottom and loaded through a smaller ring on top. This creates a constant and bi-axial bending moment in the specimen inside the smaller ring. Figure 3.13 gives a schematic representation of the ring-on-ring test. The test is controlled by applying a deformation δ on the smaller inner ring, a force can then be measured either in the same ring or on the large bottom ring. The test is performed at a very slow loading rate ($\dot{\delta} = 0.1 mm/s$), such that the test can be considered quasi-static and inertia effects can be excluded. The low loading rate removes the dynamic effects such as wave propagation and allows to focus solely on the material failure. Please note that the material rate dependency from the JH2-V model is still present, even though inertial effects are excluded by using quasi-static simulations. The only requirement is that there is some measure of (pseudo) time in the simulation, which can be found from the applied deformation rate $\dot{\delta} = 0.1 mm/s$. This ensures the material model retains its regularizing properties.

An analytical solution for the stress field inside the specimen under ROR loading exists [60, 61]. This makes it possible to relate an applied force to a (tensile) stress in the disk and find the strength of the tested material. The tensile stresses in radial (σ_r) and tangential direction (σ_θ) at the bottom of the specimen, inside the internal ring can be given as

$$\sigma_r = \sigma_\theta = \frac{3F}{4\pi h^2}\left[2(1+\nu)\ln\left(\frac{a}{b}\right) + \frac{(1-\nu)(a^2-b^2)}{R^2}\right], \tag{3.11}$$

where F is the applied force, ν the Poisson's ratio, h the specimen thickness and a, b, R the radii of the internal ring, external ring and specimen.

Experimental results for ROR bending on alumina ceramics are available in literature. In [62] an ultimate tensile stress of Wesgo alumina is presented ranging from 190 to 260MPa. In [27] the experimental results show the ultimate tensile stress ranges from 168.6 – 232.7MPa. Between these two sources the experimental set-up differs in dimensions and the alumina ceramics are similar but not exactly the same.

The geometry of the test as presented in [27] was assumed, such that $R = 9$mm, $a = 5$mm, $b = 8$mm and $e = 1$mm. Since the ROR experiment was performed on the same material as the spall test the model parameters for spall are used as (brittle) base values. A more ductile behaviour is found by using $d_1 = 0.500$. The parameter sets used in the ROR simulations are those found in columns 'Spall' and 'variation 4' from Table 3.2. The ROR problem is simulated in a 2d axi-symmetric strain formulation. Here the centre of the disk is considered as axis of symmetry, where all horizontal movement is constrained.

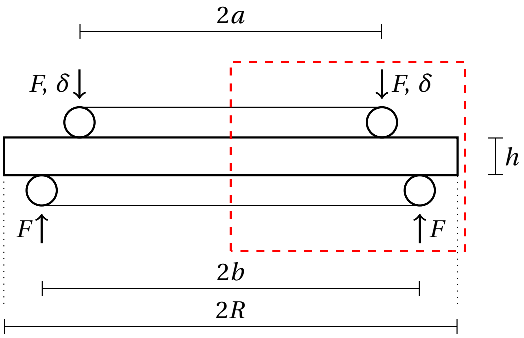

Figure 3.13: Ring on ring bending experiment. The red dashed box is the spatial domain which is used for a 2D axisymmetric simulation of the experiment.

Vertical movement is constrained for a single node on the bottom of the disk, at distance b. Vertical displacements are imposed on a single node on the top surface of the disk, at distance a. The mesh for this problem is unstructured and three noded linear triangular elements are used with a size $h \approx 0.025$mm. Figure 3.14 holds the force and displacement measured on the inner top ring during the simulation. The figure also shows two hatched zones corresponding to the experimental results from [62] and [27], for which the reported failure stresses were converted to forces using (3.11). When comparing to the experimental results it is clear that slow softening results in an overestimated material strength, while an acceptable material strength is found with fast softening of the material. The maximum stress found in the simulations was 240MPa and 329MPa for the fast and slow softening cases respectively.

RING-ON-RING CONCLUDED

The ring-on-ring test confirms that a fast softening is required under tension. Earlier it was demonstrated that slow softening was required for the compression dominated tests. This shows the obvious need for a separation in material softening, where controlling the response under tension and compression independently is possible. The next section will show that a separated material softening can indeed be used to match all previously described experiments, with a single set of parameters.

3.4. JH2-V MODEL IMPROVEMENT

The experiments and simulations in the previous sections have shown that the original failure strain formulation of the JH models is inadequate. The analysed experiments could only be matched by changing softening related parameters and could not be captured by a single set of model parameters.

For a ceramic the failure mechanisms under compression and under tension are significantly different. Failure under tension occurs by brittle fracture of the material, while a ductile response can be found under sufficiently high compression. Under high compression failure is characterized by crystal plasticity and micro-cracking. If the failure mechanisms under tension and compression are so different, it is reasonable to also

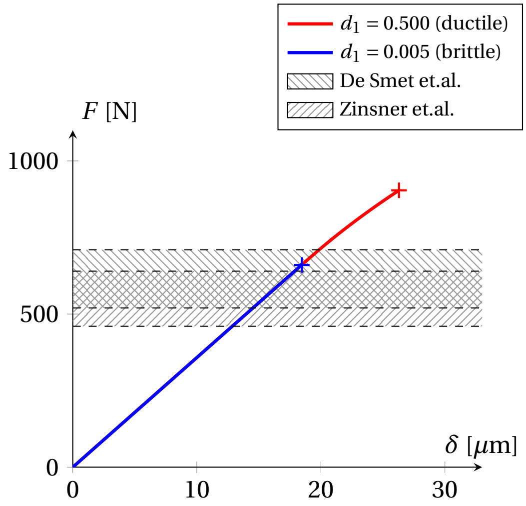

Figure 3.14: Ring on ring bending test. Results are obtained by simulation with the JH2-V material model, for two values of softening. The simulations fail to converge at the crosses, this is when a large number of points fail under apex return. This may be seen as the sudden and brittle failure of the specimen. The ultimate force for the two tests is found as 662N and 904N, corresponding to tensile stresses of 240MPa and 329MPa. Experimentally measured ranges from De Smet [62] and Zinsner [27] are given by the hatched areas.

distinguish between these two mechanisms in the material model. The material models by Deshpande-Evans and Simha presented in the section 3.2 acknowledge that a ceramic material has multiple failure mechanisms. These models capture each of the different failure mechanisms by its own softening/damage behaviour. In the JH2 material model failure is captured by the failure strain formulation (3.9). This single formulation includes a pressure dependency, but does not offer a clear separation in behaviour for each of the failure mechanisms. In fact the function couples the behaviour under tension and compression through the softening parameters d_1 and d_2. Because of this coupling, changing the failure strain under compression will inadvertently change the damage rate under tension and vice versa. In a recent publication the limited flexibility of the JH failure strain formulation (3.9) was also addressed [63], albeit for glass material using different strength formulations. In the publication a shift was proposed to the failure strain, to have zero plastic deformation to failure under low pressures and allow for accumulation of plasticity beyond some pressure threshold. This does indeed provide a clear separation between brittle tensile failure and more ductile compression failure. Such approach can however not be used in the current visco-plastic framework, since a non-zero plastic strain is required to activate viscosity and obtain regularization.

A new softening formulation is proposed, in which the damage rate under tension and compression can be controlled independently. The formulation for the rate of damage can remain the same as (3.8). The failure strain formulation from (3.9) is replaced by

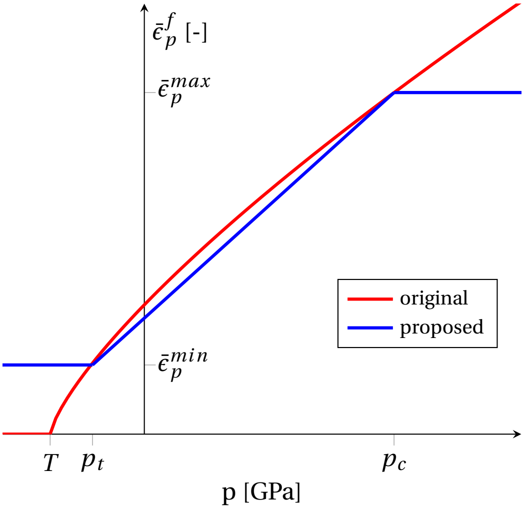

Figure 3.15: Failure strain as function of pressure, in the original JH2 and the proposed formulation.

the tri-linear equivalent plastic strain formulation

$$\bar{\epsilon}_p^f(\boldsymbol{\sigma}) = \begin{cases} \bar{\epsilon}_p^{min}, & p(\boldsymbol{\sigma}) < p_t \\ \left(\bar{\epsilon}_p^{max} - \bar{\epsilon}_p^{min}\right)\left(\frac{p(\boldsymbol{\sigma})-p_t}{p_c-p_t}\right) + \bar{\epsilon}_p^{min}, & p_t < p(\boldsymbol{\sigma}) < p_c \\ \bar{\epsilon}_p^{max}, & p_c < p(\boldsymbol{\sigma}). \end{cases} \tag{3.12}$$

This formulation assumes a failure strain $\bar{\epsilon}_p^{min}$ for pressures below p_t, a failure strain $\bar{\epsilon}_p^{max}$ for pressures above p_c and interpolates between these two values for intermediate pressures. This formulation allows for independent changes to the failure strain and thus damage rate under tension and compression. Furthermore, the model is simple, providing a clear advantage when calibrating the model as will be shown later in this section.

The proposed failure strain formulation is shown together with the original failure strain formulation in Figure 3.15. In this figure the failure strain is plotted for arbitrary model parameters. The proposed model parameters can be chosen such that the original formulation is linearly approximated in the domain $p_t < p < p_c$, but obviously this is not required.

The new formulation (3.12) requires information on the failure strains, as well as a pressure range for which the behaviour transitions from brittle to ductile. For brittle materials it is not uncommon to have a transition from brittle to ductile behaviour. Often this is linked to an ambient temperature, but a transition can also be found at a given confining pressure [64–66]. To use the proposed formulation one should ideally know the transition pressure. If this data is not available one may calibrate the model for a given test under tension and one under compression. The latter approach will be used in this chapter.

The spall and plate impact tests from the previous section can be used to calibrate the newly proposed failure strain formulation. These tests provide insight in the failure behaviour under uniaxial tensile and compressive loading. Results from sections 3.3.1 and 3.3.2 showed that the failure strain might differ by a few orders of magnitude between uniaxial tensile or compressive loading. A first approximation of the model parameters in equation (3.12) can be obtained as follows.

First consider uniaxial tensile loading on a ceramic with the material properties from Table 3.2. Under these conditions the yield strength will be reached at a pressure $p_{min} = -0.17$GPa. In the original failure strain formulation with $d_1 = 0.005$ this pressure leads to $\bar{\epsilon}_p^f(p_{min}) = 0.00015$. Similarly for uniaxial compressive loading a pressure of $p_{max} = 3.02$GPa is found and $d_1 = 0.500$ leads to a failure strain of $\bar{\epsilon}_p^f(p_{max}) = 0.4965$. Here the original model parameter d_1 was chosen as the values for which spall and plate impact simulations agreed well with experimental results. This procedure is also visualized in Figure 3.16, where the top graphs shows the intact material strength with uni-axial loading directions and the bottom graph shows the failure strain. For the failure strain the original and proposed formulations are plotted. This procedure shows how simple it is to calibrate the proposed failure strain model, using just two well established experiments.

The newly proposed tri-linear failure strain formulation (3.12) will now be used to simulate spall, plate impact, sphere impact and the ring-on-ring test. If the formulation is an improvement over the original one, all four experiments should be matched by the simulations. The JH2-V model parameters used in this final section of the chapter, for the various tests, are shown in Table 3.3. The model parameters related to viscosity and failure are kept the same in all simulations. The only variations in parameters are those in stiffness, density and Hugoniot pressure. These are well justified since the experimentally tested materials showed small variations in the elastic properties, as discussed in section 3.3.1.

Figure 3.17 provides the predicted spall strength as a function of loading rate, when using the proposed tri-linear failure strain formulation. The rate dependency in the spall strength is still captured by the model. The strengths of the JH2-V model with original and the proposed softening formulation are a very close match. This can be easily explained, as the problem is tension dominated and both formulations used a minimal failure strain $\bar{\epsilon}_p^{min} = 0.00015$ (see (3.10) and (3.12)). When the failure zone of the simulation is compared to the experiment in Figure 3.18, it is found that the failure zones agree well.

Figure 3.19 shows the inter-facial velocities measured in the plate impact simulation using the tri-linear failure strain formulation. The results agree well with the experimental results and are quite similar to those obtained with the original JH2 formulation with $d_1 = 0.500$. Again this can be easily explained since the problem is compression dominated and the failure strain in the original or tri-linear formulation is of the same order.

Figure 3.20 shows the damage predicted by a sphere impact simulation using the tri-linear failure strain formulation. The results are similar to those for $d_1 = 0.500$ from Figure 3.12. That is, a cone crack is predicted and some minor subsurface damage is present. Two differences can be found when comparing to the results from Figure 3.12. The first is that the cone crack for the tri-linear failure strain extends further into the target material. This can be explained by the more brittle behaviour found at tensile

Table 3.3: JH2-V model parameters using the improved failure strain formulation from (3.12). The model parameter sets for each test are shown. Only the stiffness, density and Hugoniot pressure are changed, which is justified because of small differences in experimentally tested ceramics.

variable	unit	Spall value	Plate impact value	Sphere impact value	ROR value
E	GPa	360.0	**380.0**	**380.0**	360.0
ν	-	0.22	0.22	0.22	0.22
ρ	kg/m^3	3850	**3890**	**3890**	3850
A	GPa	0.930	0.930	0.930	0.930
B	GPa	0.310	0.310	0.310	0.310
n	-	0.6	0.6	0.6	0.6
m	-	0.6	0.6	0.6	0.6
C	-	0.0	0.0	0.0	0.0
T	GPa	0.2	0.2	0.2	0.2
η	GPa·s	$0.028\cdot10^{-3}$	$0.028\cdot10^{-3}$	$0.028\cdot10^{-3}$	$0.028\cdot10^{-3}$
$\dot{\lambda}_t$	s^{-1}	$4\cdot10^4$	$4\cdot10^4$	$4\cdot10^4$	$4\cdot10^4$
HEL	GPa	6.25	6.25	6.25	6.25
P_{HEL}	GPa	3.50	**3.25**	**3.25**	3.50
σ_{HEL}	GPa	4.125	**4.50**	**4.50**	4.125
$\bar{\epsilon}_p^{min}$	-	$1.5\cdot10^{-4}$	$1.5\cdot10^{-4}$	$1.5\cdot10^{-4}$	$1.5\cdot10^{-4}$
$\bar{\epsilon}_p^{max}$	-	0.4965	0.4965	0.4965	0.4965
p_t	GPa	-0.17	-0.17	-0.17	-0.17
p_c	GPa	3.02	3.02	3.02	3.02

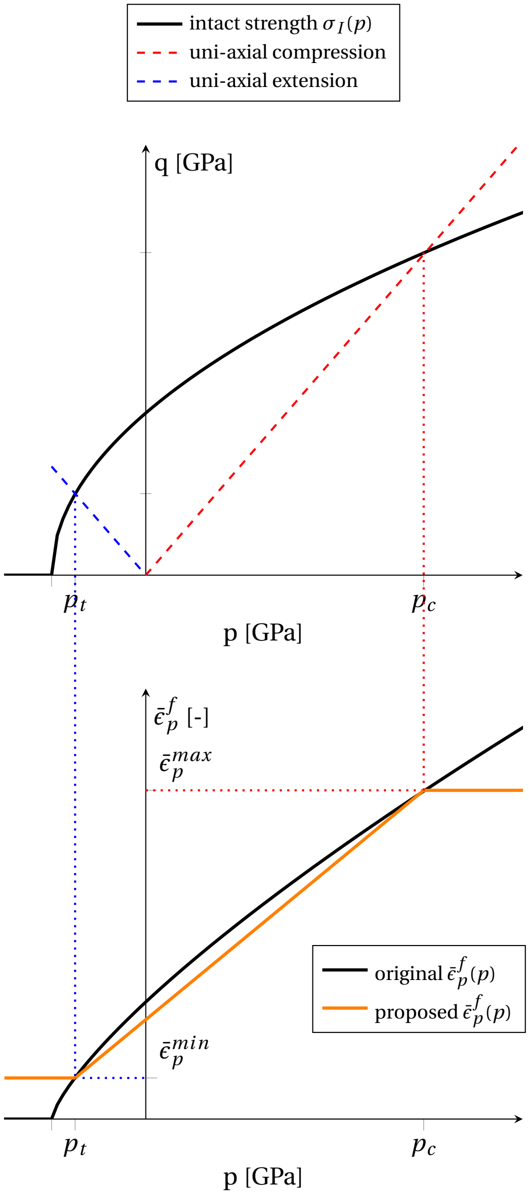

Figure 3.16: Intact material strength and failure strains plotted as a function of pressure. The original and proposed tri-linear failure strain is shown. The proposed failure strain formulation is fitted to the original failure strains, found under uni-axial deformation of the ceramic.

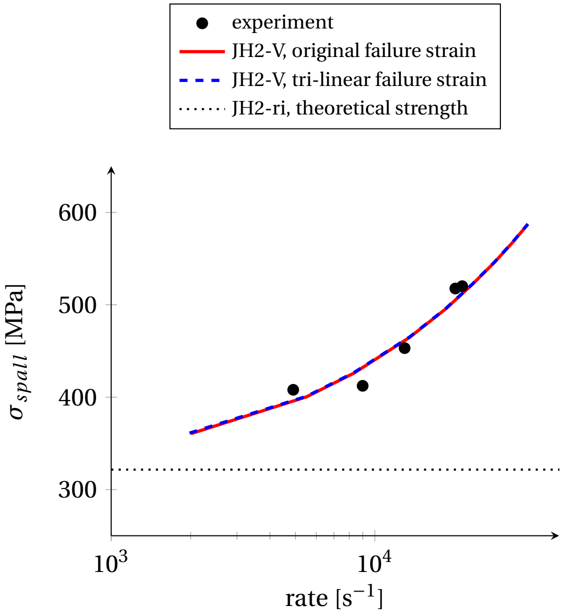

Figure 3.17: Spall strength, experimentally measured and predicted by simulation. The proposed tri-linear failure strain model is used, all cases use $\eta = 0.028 \cdot 10^{-3}$ GPa·s and $\dot{\lambda}_t = 40 \cdot 10^3$ s^{-1} as these values were used to obtain good results in sphere impact simulations. A minimal failure strain $\bar{\epsilon}_p^{min} = 1.5 \cdot 10^{-4}$ is used for both the original and the tri-linear failure strains.

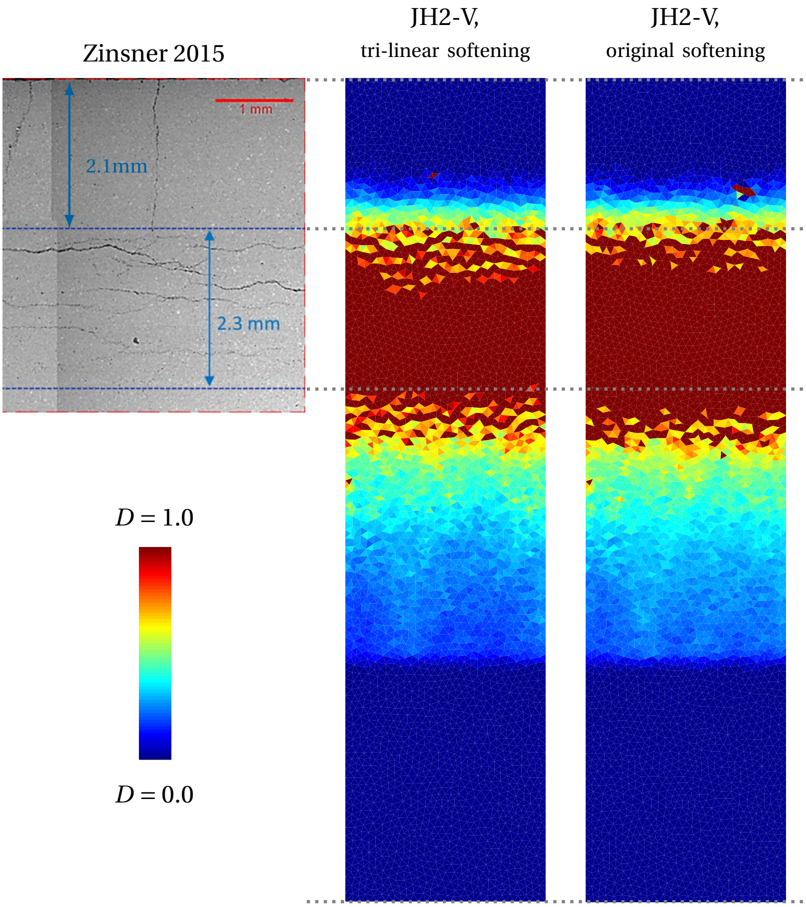

Figure 3.18: Damage profiles obtained in the spall experiment [27] and FE simulations. Stress wave 2 from Figure 3.2a is applied. The JH2-V material model with original and newly proposed tri-linear failure strain formulation is compared.

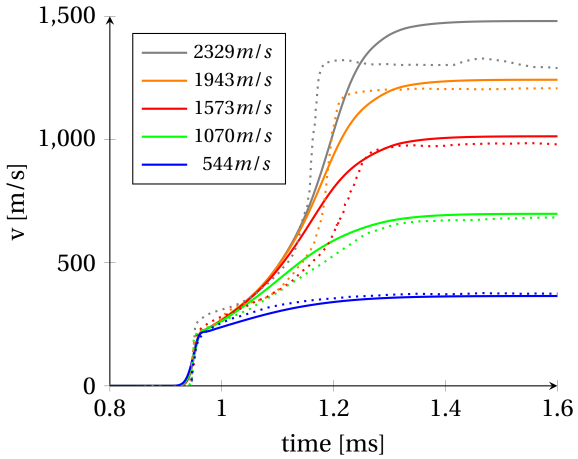

Figure 3.19: Simulation results for a plate impact test on alumina ceramic. The parameter set for the spall test is used, but with the newly proposed failure strain formulation and $\dot{\lambda}_t = 40000\text{s}^{-1}$. The results are very similar to those obtained with the original JH2 formulation with $d_1 = 0.500$ and $\dot{\lambda}_t = 40000\text{s}^{-1}$, from Figure3.9. The dotted lines show the experimental results from [55], the solid lines are simulation results.

states in the new formulation. The second difference is that the tri-linear formulation results show more damage at the target surface. Again this is a zone where the pressure is low (or even negative), for which the behaviour is brittle in the tri-linear formulation.

As a final step the ring-on-ring simulations are performed with the newly proposed failure strain formulation. A tensile strength is found of 251MPa. This is slightly higher than the previously found value for the original model with $d_1 = 0.005$. However, the strength predicted by the newly proposed model still falls within the experimentally measured ranges (190 – 260MPa from [62] and 168.6 – 232.7MPa from [27]).

3.5. CONCLUSIONS

A ceramic material may fail as a consequence of different mechanisms. Depending on the stress state in the material one or more of these failure mechanisms may be activated. Since the mechanisms are different, so should the modelling of these mechanisms be. The original JH2 model does not distinguish between different failure mechanisms. In the JH2 model the rate of damage is determined by the failure strain. This failure strain is a function of pressure, where tensile states have a low strain to failure and a brittle response while high pressures have a high strain to failure and a more ductile response. The failure strain is, however, a single function and behaviour under tension and compression are inseparably coupled. By simulating a number of experiments under different loading conditions it was shown that this single function is indeed incapable of properly capturing the behaviour of the various failure modes in ceramic material.

Four experiments were simulated using the JH2-V model with the original JH2 failure strain formulation. All experimental results were obtained from literature and in all experiments a similar high purity alumina ceramic was considered. The first experiment

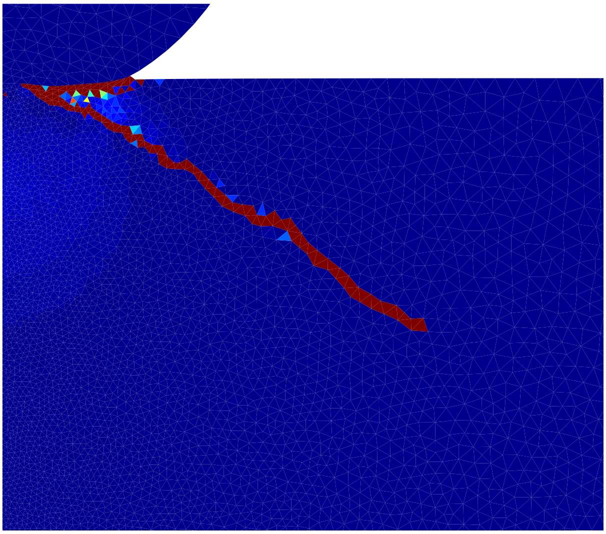

Figure 3.20: Sphere impact results for the JH2-V model with tri-linear failure strain. Cone cracks are clearly visible, as well as some minor subsurface damage. Complete failure of the ceramic below the projectile is not observed.

was spall, which loads the material in uni-axial extension. The second experiment was plate impact, loading the material in uni-axial contraction. Sphere impact was the third experiment, in which the material experiences a wide range of stress states. As a final test ring-on-ring bending was considered, a quasi-static test with failure of the material in bi-axial tension.

Simulation of spall and plate impact experiments showed that a match for both could only be obtained by changing the material parameters. Either increasing the residual strength of the material or the failure strain of the material was required to match the plate impact experiments by simulation. A recalibration of the model parameters would be sufficient to match both types of tests, although this would increase some model parameters by a few orders of magnitude compared to what is used in literature.

The sphere impact experiments and simulations were used to investigate the parameter choice in the material model. Increasing the residual strength of the material, which was found to give a match in plate impact results, did not lead to good results in the sphere impact test. It was found that a match with experiments could only be found by increasing the failure strain. At this point recalibrating the failure strain parameters would be sufficient to find matching results of the spall, plate impact and sphere impact tests. However, doing so would require a failure strain two orders of magnitude larger than what was reported in literature. This could jeopardize the brittle behaviour of the material under tension.

As a final check a ring-on-ring test was simulated. This quasi-static test loads the material in bi-axial tension. It was shown that the material tensile strength was greatly overestimated when using a high failure strain.

The results of the four experiments and simulations showed that the ceramic material required both a high and a low failure strain, depending on the stress state. The original failure strain formulation in the JH models could not be tuned to provide this range of failure strains. A new tri-linear formulation was proposed, in which failure strains under tension and compression were treated as independent quantities. With this formulation a brittle response could be obtained under tension, while maintaining a ductile response under compression. It was shown that this new formulation could be used to match all experiments considered in this chapter, for a single set of failure parameters. The latter is key, as this was not possible with the original failure strain formulation.

REFERENCES

[1] E. C. Simons, J. Weerheijm, and L. J. Sluys, *Simulating brittle and ductile response of alumina ceramics under dynamic loading,* Engineering Fracture Mechanics **216** (2019), https://doi.org/10.1016/j.engfracmech.2019.05.013.

[2] P. J. Hazell, *Ceramic Armour: Design and Defeat Mechanisms* (Argos Press, Canberra, 2006).

[3] S. M. Walley, *Historical review of high strain rate and shock properties of ceramics relevant to their application in armour,* Advances in Applied Ceramics **109**, 446 (2010).

[4] Z. Rosenberg and E. Dekel, *Terminal ballistics,* 2nd ed. (Springer-Verlag, Heidelberg, 2012).

[5] J. Cagnoux and F. Longy, *Spallation and shock-wave behaviour of some ceramics,* Le Journal de Physique Colloques **49**, C3 (1988).

[6] J. Lankford, C. A. Jr, A. Nagy, J. Walker, and A. Nicholls, *Inelastic response of confined aluminium oxide under dynamic loading conditions,* Journal of Materials Science **33**, 1619 (1998).

[7] S. Acharya, S. Bysakh, V. Parameswaran, and A. Kumar Mukhopadhyay, *Deformation and failure of alumina under high strain rate compressive loading,* Ceramics International **41**, 6793 (2015).

[8] J. Wade, S. Robertson, and H. Wu, *Plastic deformation of polycrystalline alumina introduced by scaled-down drop-weight impacts,* Materials Letters **175**, 143 (2016).

[9] M. Bhattacharya, S. Dalui, N. Dey, S. Bysakh, J. Ghosh, and A. K. Mukhopadhyay, *Low strain rate compressive failure mechanism of coarse grain alumina,* Ceramics International **42**, 9875 (2016).

[10] A. Fischer-Cripps and B. R. Lawn, *Stress Analysis of Contact Deformation in Quasi-Plastic Ceramics,* Journal of the American Ceramic Society **79**, 2609 (1996).

[11] A. A. Wereszczak, T. P. Kirkland, K. T. Strong, T. J. Holmquist, and D. S. A, *ORNL Quasi-Static Mechanical Characterization and Analysis : FY09 Annual Report to TARDEC Under contract DE-AC05-00OR22725,* Tech. Rep. (Oak Ridge National Laboratory, 2009).

[12] T. J. Ahrens, *Material Strength Effect in the Shock Compression of Alumina,* Journal of Applied Physics **39**, 4610 (1968).

[13] W. H. Gust and E. Royce, *Dynamic Yield Strengths of B4C, BeO, and Al2O3 Ceramics,* Journal of Applied Physics **42**, 276 (1971).

[14] A. Rajendran and J. L. Kroupa, *Impact damage model for ceramic materials,* Journal of Applied Physics **66**, 3560 (1989).

[15] A. Rajendran, *High Strain Rate Behavior of Metals Ceramics, and Concrete*, Tech. Rep. (University of Dayton Research Institute, Dayton, Ohio, 1992).

[16] Y. Partom, *Calibrating a material model for AD995 alumina from plate impact VISAR profile,* Journal de Physique IV **4**, 495 (1994).

[17] D. E. Grady and R. L. Moody, *Shock Compression Profiles in Ceramics*, Tech. Rep. March (Sandia National Laboratories, Albuquerque, 1996).

[18] D. Grady, *Shock-wave compression of brittle solids,* Mechanics of Materials **29**, 181 (1998).

[19] T. J. Vogler, W. D. Reinhart, and L. C. Chhabildas, *Dynamic behavior of boron carbide,* Journal of Applied Physics **95**, 4173 (2004).

[20] E. B. Zaretsky, *High temperature impact response of 998 alumina,* Journal of Applied Physics **114**, 183518 (2013).

[21] I. Girlitsky, E. Zaretsky, S. Kalabukhov, M. P. Dariel, and N. Frage, *Dynamic compressive and tensile strengths of spark plasma sintered alumina,* Journal of Applied Physics **115**, 243505 (2014).

[22] F. Gálvez, J. Rodríguez, and V. Sánchez, *Tensile strength measurements of ceramic materials at high rates of strain,* Journal of physics IV France **7**, 151 (1997).

[23] F. Gálvez, J. Rodríguez, and V. Sánchez Galvez, *Influence of the Strain Rate on the Tensile Strength in Aluminas of Different Purity,* Journal of Physics IV **10**, 323 (2000).

[24] F. G. Díaz-Rubio, J. R. Pérez, and V. S. Gálvez, *The spalling of long bars as a reliable method of measuring the dynamic tensile strength of ceramics,* International Journal of Impact Engineering **27**, 161 (2002).

[25] J. Buchar and S. Rolc, *Dynamic fracture of ceramics,* Journal de Physique IV (Proceedings) **134**, 681 (2006).

[26] B. Erzar and E. Buzaud, *Shockless spalling damage of alumina ceramic,* European Physical Journal: Special Topics **206**, 71 (2012).

[27] J. L. Zinszner, B. Erzar, P. Forquin, and E. Buzaud, *Dynamic fragmentation of an alumina ceramic subjected to shockless spalling: An experimental and numerical study,* Journal of the Mechanics and Physics of Solids **85**, 112 (2015).

[28] J.-l. Zinszner, B. Erzar, and P. Forquin, *Strain rate sensitivity of the tensile strength of two silicon carbides : experimental evidence and micromechanical modelling,* Philosophical transactions A (2017).

[29] G. R. Johnson and T. J. Holmquist, *A computational constitutive model for brittle materials subjected to large strains, high strain rates, and high pressures,* Shock Wave and High-Strain-Rate Phenomena in Materials (1992).

[30] G. R. Johnson and T. J. Holmquist, *An improved computational constitutive model for brittle materials,* AIP Conference Proceedings **309**, 981 (1994).

[31] G. R. Johnson, T. J. Holmquist, and S. R. Beissel, *Response of aluminum nitride (including a phase change) to large strains, high strain rates, and high pressures,* Journal of Applied Physics **94**, 1639 (2003).

[32] C. Simha, S. Bless, and A. Bedford, *Computational modeling of the penetration response of a high-purity ceramic,* International journal of impact engineering **27**, 65 (2002).

[33] V. S. Deshpande and A. G. Evans, *Inelastic deformation and energy dissipation in ceramics: A mechanism-based constitutive model,* Journal of the Mechanics and Physics of Solids **56**, 3077 (2008).

[34] V. S. Deshpande, E. A. N. Gamble, B. G. Compton, R. M. McMeeking, A. G. Evans, and F. W. Zok, *A Constitutive Description of the Inelastic Response of Ceramics,* Journal of the American Ceramic Society **94**, s204 (2011).

[35] E. C. Simons, J. Weerheijm, and L. J. Sluys, *A viscosity regularized plasticity model for ceramics,* European Journal of Mechanics / A Solids **72**, 310 (2018).

[36] A. Needleman, *Material rate dependence and mesh sensitivity in localization problems,* Computer Methods in Applied Mechanics and Engineering **67**, 69 (1988).

[37] W. Wang, L. Sluys, and R. De Borst, *Interaction between material length scale and imperfection size for localisation phenomena in viscoplastic media,* European Journal of Mechanics - A/Solids **15**, 447 (1996).

[38] A. Winnicki, C. J. Pearce, and N. Bićanić, *Viscoplastic Hoffman consistency model for concrete,* Computers and Structures **79**, 7 (2001).

[39] Dynaflow Research Group, *Jem-jive,* http://jem-jive.com.

[40] D. Sulsky, Z. Chen, and H. L. Schreyer, *A particle method for history-dependent materials,* Computer Methods in Applied Mechanics and Engineering **118**, 179 (1994).

[41] F. Li, J. Pan, and C. Sinka, *Modelling brittle impact failure of disc particles using material point method,* International Journal of Impact Engineering **38**, 653 (2011).

[42] L. B. Lucy, *A numerical approach to the testing of the fission hypothesis,* The Astronomical Journal **82**, 1013 (1977).

[43] J. J. Monaghan, *Smoothed particle hydrodynamics,* Annual Review of Astronomy and Astrophysics **30**, 543 (1992), arXiv:1007.1245 .

[44] R. Clegg, *Development and application of a Rankine plasticity model for improved prediction of tensile cracking in ceramic and concrete materials under impact,* 14th DYMAT Technical … (2002).

[45] E. Strassburger, *Visualization of Impact Damage in Ceramics Using the Edge-On Impact Technique,* International Journal of Applied Ceramic Technology **1**, 235 (2005).

[46] W. Riedel, S. Hiermaier, and K. Thoma, *Transient stress and failure analysis of impact experiments with ceramics,* Materials Science and Engineering B: Solid-State Materials for Advanced Technology **173**, 139 (2010).

[47] H. Zolghadr Jahromi and B. A. Izzuddin, *Energy conserving algorithms for dynamic contact analysis using newmark methods,* Computers and Structures **118**, 74 (2013).

[48] J. Ning, H. Ren, T. Guo, and P. Li, *Dynamic response of alumina ceramics impacted by long tungsten projectile,* International Journal of Impact Engineering **62**, 60 (2013).

[49] H. L. Ren, X. F. Shu, and L. I. Ping, *Numerical and experimental investigation of the fracture behavior of shock loaded alumina,* Science China: Physics, Mechanics and Astronomy **53**, 244 (2010).

[50] S. Feli and M. Asgari, *Finite element simulation of ceramic/composite armor under ballistic impact,* Composites Part B: Engineering **42**, 771 (2011).

[51] P. Lundberg, *Interface Defeat and Penetration : Two Modes of Interaction between Metallic Projectiles and Ceramic Targets,* Comprehensive Summaries of Uppsala Disserations from the Faculty of Science and Technology (2004).

[52] R. Krashanitsa and S. Shkarayev, *Computational Study of Dynamic Response and Flow Behavior of Damaged Ceramics,* in *46th AIAA/ASME/ASCE/AHS/ASC Structures, Structural Dynamics and Materials Conference* (2005) pp. 1–8.

[53] C. Swaroop and A. K. Srivastava, *Numerical Analysis of Ballistic Performance of Curved Ceramic,* in *Proceeding of STME-2013, International Conference on Smart Technologies for Mechanical Engineering* (Delhi, 2013).

[54] A. Tasdemirci and I. W. Hall, *Numerical and experimental studies of damage generation in multi-layer composite materials at high strain rates,* International Journal of Impact Engineering **34**, 189 (2007).

[55] D. E. Grady, *Dynamic Properties of Ceramic Materials,* Tech. Rep. February (Sandia National Laboratories, Albuquerque, 1995).

[56] T. J. Hughes, *Generalization of Selective Integration Procedures to Anisotropic and Nonlinear Media,* Short Communications , 1413 (1980).

[57] B. G. Compton, E. A. N. Gamble, V. S. Deshpande, and F. W. Zok, *Damage development in an armor alumina impacted with ductile metal spheres,* Journal of Mechanics of Materials and Structures **7** (2012).

[58] K. A. Iyer, *Relationships between multiaxial stress states and internal fracture patterns in sphere-impacted silicon carbide,* International Journal of Fracture **146**, 1 (2007).

[59] E. K. Öberg, J. Dean, and T. W. Clyne, *Effect of inter-layer toughness in ballistic protection systems on absorption of projectile energy,* International Journal of Impact Engineering **76**, 75 (2015).

[60] a. F. Kirstein and R. M. Woolley, *Symmetrical bending of thin circular elastic plates on equally spaced point supports,* Journal of Research of the National Bureau of Standards, Section C: Engineering and Instrumentation **71C**, 1 (1967).

[61] C. H. Hsueh, C. R. Luttrell, and P. F. Becher, *Modelling of bonded multilayered disks subjected to biaxial flexure tests,* International Journal of Solids and Structures **43**, 6014 (2006).

[62] B. J. de Smet, P. W. Bach, H. F. Scholten, L. J. Dortmans, and G. de With, *Weakest-link failure predictions for ceramics III: Uniaxial and biaxial bend tests on alumina,* Journal of the European Ceramic Society **10**, 101 (1992).

[63] T. J. Holmquist, G. R. Johnson, and C. a. Gerlach, *An improved computational constitutive model for glass,* Philosophical Transactions of the Royal Society A: Mathematical, Physical and Engineering Sciences **375** (2017), 10.1098/rsta.2016.0182.

[64] H. C. Heard and C. F. Cline, *Mechanical behaviour of polycrystalline BeO, Al2O3 and AlN at high pressure,* Journal of Materials Science **15**, 1889 (1980).

[65] E. Zaretsky, V. Paris, G. Kanel, and A. Savinykh, *Evidences of ductile and brittle responses of ceramics under shock wave loading,* Journal de Physique IV2 **110**, 917 (2003).

[66] E. Zaretsky, V. Paris, G. Kanel, and A. Savinykh, *Evidence of Ductile (Alumina) and Brittle (Boron Carbide) Response of Ceramics Under Shock Wave Loading,* Ceramic Transactions **151**, 105 (2003), arXiv:arXiv:1011.1669v3 .

4

AN EXPERIMENTAL AND NUMERICAL INVESTIGATION OF SPHERE IMPACT ON ALUMINA CERAMIC

4.1. INTRODUCTION

Ceramic materials are good candidates for armour systems because they have a high hardness and a relatively low weight. During impact on such a hard ceramic a projectile may deform and even fracture. During this interaction the ceramic target can also damage. Ceramic damage ranges from brittle crack formation to ductile plasticity when sufficient confinement is provided. Understanding this complex failure behaviour of ceramic is challenging, but necessary to improve ceramic armour performance.

Full projectile-target tests can provide useful information on an armour ceramic's protective capability. Upon impact, the ceramic is often pulverized and although the armour system's performance may be known [2], the actual failure mechanisms can generally not be studied in these tests. An alternative method is to perform spherical projectile impact tests, where a lighter and spherical projectile leads to clean failure of the ceramic. In a sphere impact experiment, cone cracks, radial cracks and lateral cracks can all be clearly identified when analysing the tested specimen. Thus, sphere impact offers a simpler way to study failure in ceramics under impact loading and literature offers many examples [3–6].

To understand the ceramic failure process during sphere impact one may simulate the experiment, for instance using the Finite Element Method [7–11]. However, perform-

---

This chapter is based on [1]

ing proper simulations is challenging as the problem is both highly dynamic and highly non-linear. The choices one makes on the models and methods will affect physical correctness, numerical soundness and computation time.

In order to derive a physically correct response in a sphere impact simulation the choice of material model is very important. For ceramic material one may for instance use one of the models by Johnson and Holmquist [12–14], the model by Simha [15] or one of the models by Deshpande and Evans [16, 17]. The model presented in 1994 by Johnson and Holmquist [13] (JH2) is an often used and widely accepted model, hence this model was chosen as starting point for the current research. The JH2 ceramic material model is a softening plasticity model, which is a class of models known to suffer from mesh dependency. In Chapter 2 the mesh dependency of this model was solved by introducing a viscosity on the tensile strength of the material model, renaming it to the viscosity regularized JH2 model or simply JH2-V. It was also shown that this viscosity allowed to properly capture rate dependency in the spall strength of ceramics. After providing a solution to mesh dependency the next step was to check the physical correctness of the JH2-V model. This was thoroughly done in Chapter 3,where the model was validated to four different types of experiments. It was found that the original failure formulation lacked flexibility to capture both the brittle behaviour under tension as well as the ductile behaviour under large confining pressures. An adaptation to the failure formulation was proposed, which separated the failure behaviour under tension and compression. This upgraded JH2-V model from Chapter 3is used as basis in the current paper, as it is known to give mesh independent and physically correct results for the relevant loading cases.

The goal of the current chapter is to study the failure of ceramics under sphere impact. Both numerical and experimental results will be presented. The chapter is structured as followed. First, the experimental method for sphere impact on ceramic material will be explained in Section 4.2. Experimental results are also shown in this section, as well as a schematic overview of all expected failure mechanisms in the test. In Section 4.3 the material models used to describe the projectile and target in the finite element simulations are presented. Section 4.4 continues to complete the numerical framework necessary for sphere impact simulations. Here additional model choices are investigated, to analyse the necessity to include material bulking and contact friction and to validate the mesh-independency of the upgraded JH2-V model. The completed framework is then used to perform a 3d simulation on sphere impact, to show that all failure mechanisms are captured correctly. Using this numerical framework, in Section 4.5, the simulations of sphere impact are compared to new experimental results. This section validated both the framework and the upgraded JH2-V model for sphere impact on ceramics. As a final part of this chapter, the simulation results are discussed in more details in Section 4.6. Here simulations provide insight into the failure process under sphere impact, which could not be derived from experiments.

4.2. SPHERE IMPACT EXPERIMENTS

Experiments were carried out [18] to monitor the damage evolution occurring in aluminum oxide (alumina) tiles impacted by a spherical projectile. The projectile was fired with a gas gun, at velocities $v_0 = 100$, 200 or $300 m/s$. A laser detector was used to measure the initial velocity of the projectile. Two cameras were used to record the impact ex-

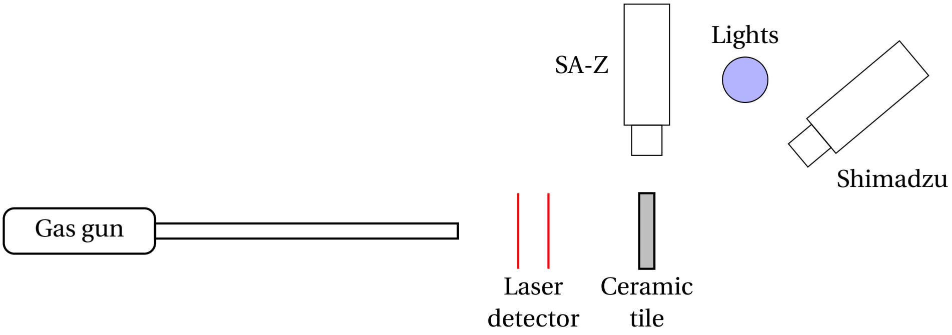

Figure 4.1: Experimental set-up, as used in [18].

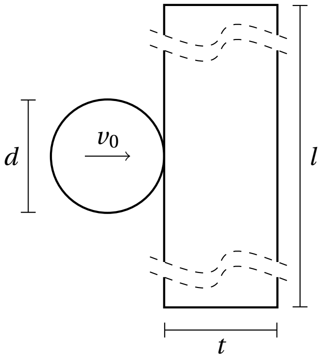

Figure 4.2: Sphere impact test, the projectile is given an initial velocity v_0. Geometry of the simulated problem is given. Note that the figure does not show the true aspect ratios.

periments. One Shimadzu HPV-X camera with 1.000.000 fps was used to record the back face response of the tile while a Photron FastCam SA-Z with 35.000 fps recorded the response of the ceramic tile from the side. The configuration of the experiment is schematically shown in Figure 4.1. Based on high speed video recordings and post-mortem analysis of the ceramic specimen, the failure of the ceramic target could be studied.

The projectile in the sphere impact experiments had a diameter $d = 6.35$mm and was made from chrome steel E52100 with a hardness of 62 HRC. The square ceramic tiles are made from alumina ceramic (Al2O3), with a lateral size $l = 101.6$mm. Two tile thicknesses of $t = 9$mm and $t = 13$mm were considered. The ceramic tile was unsupported at its back surface and was positioned standing on one of its sides. A schematic overview of the projectile and target is given in Figure 4.2.

4.2.1. RESULTS

A total of 17 experiments have been performed on 9mm and 13mm thick ceramic tiles, with impact velocities of 100-200-300m/s. The results of these experiments were previously reported by Defence Research and Development Canada (DRDC) in [18]. Figure 4.3 holds pictures of the ceramic material after the impact test. It shows the impacted front

Table 4.1: Experimental results from DRDC compared with simulations, based on failure mechanisms. For each experiment the ✗and ✓symbols are used to show if the failure mode was found. The ★symbol is used for unavailable test data.

9mm	Experiment, cracks		
velocity	cone	radial	lateral
100m/s	✓✓✓	✓✓✓	✓✓✓
200m/s	✓✓✓	✓✓✓	✓★✓
300m/s	✓✓✓	✓✓✓	✓✓✓
13mm	Experiment, cracks		
velocity	cone	radial	lateral
100m/s	✗✗	✗✗	✗✗
200m/s	✓✓✓	✓✓✓	✗✓✗
300m/s	✓✓✓	✓✓✓	✗✓✗

face of the ceramic tiles with any ejected and retrieved material placed next to the tile. Before taking the pictures the tile fragments were put back together. Except for the 13mm tile impacted at 100m/s, all ceramic tiles were split by radial cracks and show ejected ceramic cones. Four of the five ejected cones show that the tip is separated by a lateral crack and that the base is fragmented by radial cracks. Only for the 13mm tile impacted at 200m/s the ejected cone appears to be intact. However, application of a dye penetrant also revealed radial cracks in this cone, as the picture of this target's back surface shows in Figure 4.4. It was also attempted to reveal any lateral cracks in this cone by applying a dye penetrant, but unfortunately due to the rough cone surface a potential lateral crack could not be revealed in this cone.

In Table 4.1 the failure mechanisms of all experiments are reported. The symbols in the table indicate whether a particular failure mechanisms could be found in the experiment or not. The failure mechanisms in the experiments show good reproducibility. Most experiments performed under the same conditions show the same failure mechanisms. Exceptions are the lateral cracking for the 13mm tiles impacted at 200m/s and 300m/s. In these experiments only one test shows lateral cracking and two do not. It could be that these cracks were present but are not open and visible, similar to the radial cracking from Figure 4.4. Unfortunately the current dye penetrant method could not reveal any lateral cracking, so the existence of these cracks can only be speculated.

The observed failure mechanisms in the ceramic under impact agree well with literature, where four main failure mechanisms are described [4, 10, 19–21]. Three types of cracks form; cone cracks, radial cracks and lateral cracks. These were all observed in the sphere impact experiments. The fourth failure mechanism is found as inelastic deformation of the ceramic below the projectile, characterized in the material by plasticity and microcracking. This mechanisms is harder to observe and often requires additional processing and analysis of the specimen after the experiments. In the current experiments this was not done. Based on literature and the experimental observations presented in this section a schematic overview of failure can be made, which is presented in Figure 4.5. The numerical framework presented in the next sections should be able to predict all of these failure mechanisms.

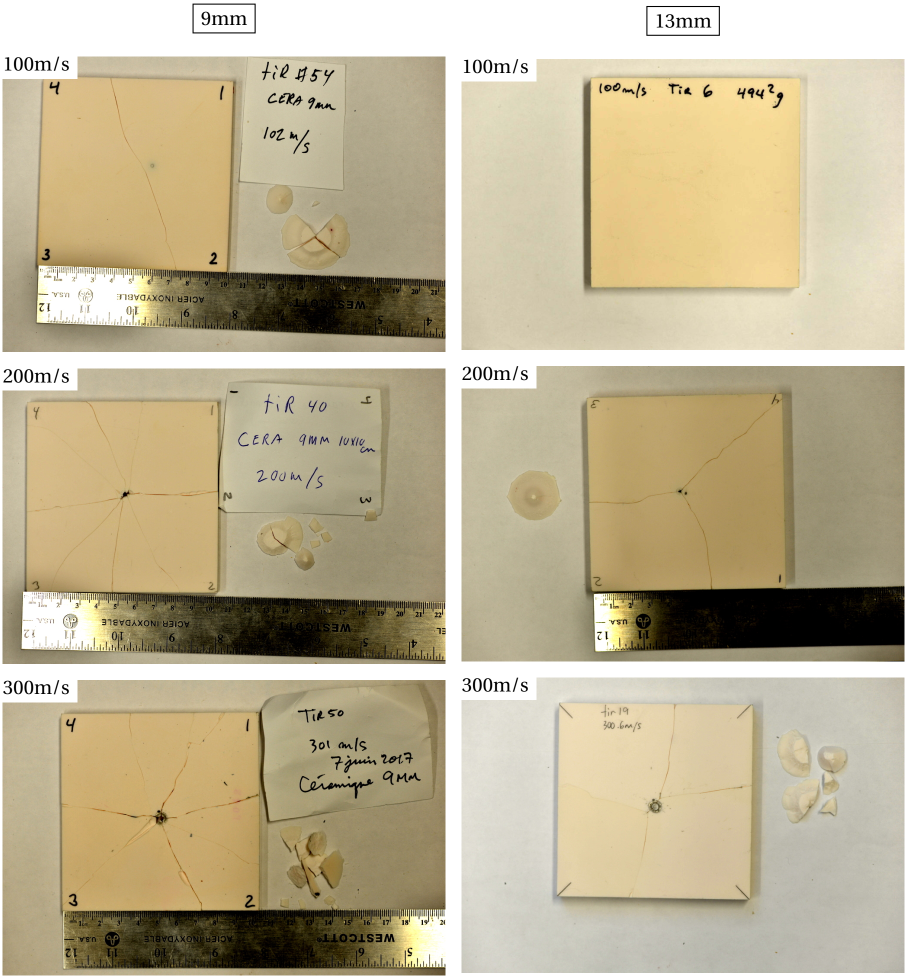

Figure 4.3: Experimental results of sphere impact on alumina ceramic. Two tile thicknesses are considered for three impact velocities. For all test cases the target front surface is shown, with (parts of) the cone next to it. The 13mm 100m/s cases did not result in cone formation.

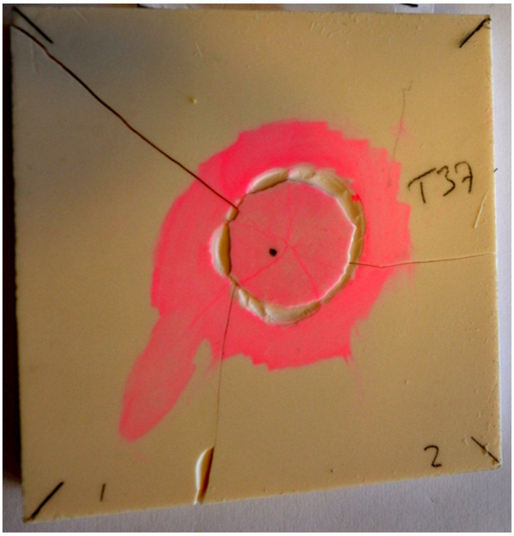

Figure 4.4: Back surface of a 13mm alumina tile impacted at 200m/s. Dye penetrant reveals unopened radial cracks in the cone and tile.

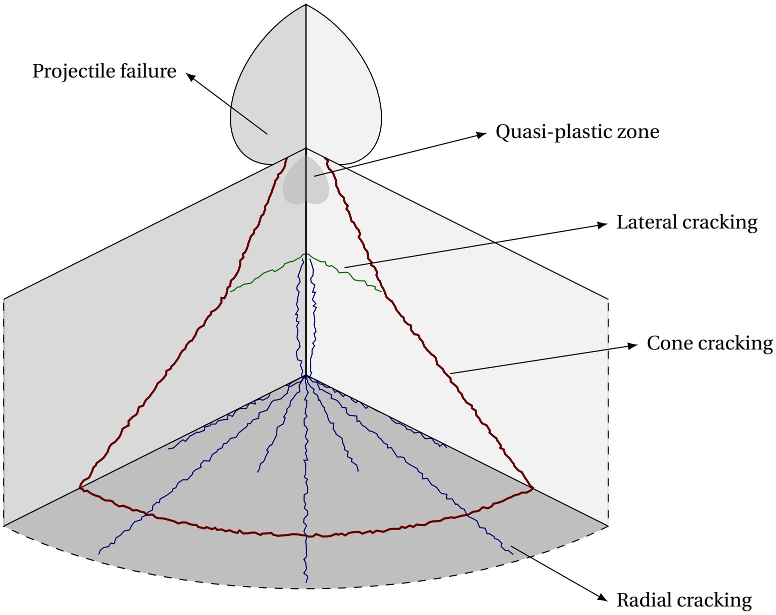

Figure 4.5: Schematic overview of failure mechanisms in sphere impact on ceramic material.

4.3. FINITE ELEMENT MODELLING

Finite Element (FE) simulations are performed, using an in-house C++ code written with the libraries of JemJive [22]. A key element of these FE simulations are the constitutive models. The models used to describe the projectile steel and the ceramic target are introduced in the current section. For the ceramic material model the formulation of material strength and failure will be briefly introduced. The material model parameters for both the steel and ceramic will also be given.

4.3.1. STEEL MATERIAL MODEL

The projectile used in the sphere impact experiments is made out of E52100 chrome steel. The behaviour of this material will be described by the Johnson-Cook constitutive model [23]. Parameters for this material and model are obtained from [24]. Elastic properties are: $E = 210\text{GPa}$, $\nu = 0.3$ and $\rho = 7800\text{kg/m}^3$. The yield stress is taken as $A = 2.4824\text{GPa}$ and hardening parameters $B = 1.4985\text{GPa}$ and $n = 0.19$ are used. Effects due to loading rate and temperature are disregarded for the projectile.

4.3.2. CERAMIC MATERIAL MODEL

The target material used in the sphere impact experiments is an alumina ceramic. This material will be described by the upgraded viscosity regularized Johnson-Holmquist-2 material model (JH2-V). Before explaining the intricate details of this model some clarification on the name of this model is given. The base ceramic model is the second model developed by Johnson and Holmquist, also known as the “JH2” model [13]. The material strength of this model was modified to include a viscosity, resulting in the “JH2-V” model [25]. In addition the failure formulation was modified, finally resulting in the “upgraded JH2-V” model [26]. The strength and failure formulation of this model are briefly explained in this subsection.

STRENGTH

The JH2 [13] material model is widely used to describe ceramic material under ballistic loading. The JH2 model is essentially a softening plasticity model with a yield function

$$f(\boldsymbol{\sigma}, D) = \sigma_{eq}(\boldsymbol{\sigma}) - \sigma_y(\boldsymbol{\sigma}, D), \tag{4.1}$$

where $\boldsymbol{\sigma}$ is the stress tensor, D is a scalar damage variable, σ_{eq} the Von Mises equivalent stress and σ_y the yield stress. Softening plasticity models are known to suffer from mesh dependency, which is also true for the JH2 model [25]. To solve this mesh dependency a rate dependency (i.e. viscosity) was added to the material model. In the JH2-V model the yield function is therefore given as

$$f(\boldsymbol{\sigma}, D, \dot{\bar{\epsilon}}_p) = \sigma_{eq}(\boldsymbol{\sigma}) - \sigma_y(\boldsymbol{\sigma}, D, \dot{\bar{\epsilon}}_p), \tag{4.2}$$

where the dependency of the material yield stress on the equivalent plastic strain rate $\dot{\bar{\epsilon}}_p$ is now clearly visible. The yield stress for the JH2-V model is given as

$$\sigma_y^*(\boldsymbol{\sigma}, D, \dot{\bar{\epsilon}}_p) = (1 - D)\ \sigma_i^*(\boldsymbol{\sigma}, \dot{\bar{\epsilon}}_p) + D\,\sigma_f^*(\boldsymbol{\sigma}). \tag{4.3}$$

Here * indicates a normalized value with respect to the equivalent stress σ_{HEL} at the Hugoniot elastic limit (HEL). The quantities of σ_i and σ_f are the intact and residual material strength of the ceramic. The material strengths for this JH2-V material model are defined as

$$\sigma_i^*(\boldsymbol{\sigma},\dot{\bar{\epsilon}}_p) = A\left(\frac{T(\dot{\bar{\epsilon}}_p)+p(\boldsymbol{\sigma})}{P_{HEL}}\right)^n, \tag{4.4}$$

$$\sigma_f^*(\boldsymbol{\sigma}) = B\left(\frac{p(\boldsymbol{\sigma})}{P_{HEL}}\right)^m. \tag{4.5}$$

Here $p(\boldsymbol{\sigma})$ is the pressure and $A,\ B,\ n,\ m,\ P_{HEL}$ are material properties, as is the apex pressure $T(\dot{\bar{\epsilon}}_p)$ which is now made a function of the equivalent plastic strain rate $\dot{\bar{\epsilon}}_p$. A mixed linear/logarithmic formulation was proposed, describing the apex pressure as

$$T(\dot{\bar{\epsilon}}_p) = T(\dot{\lambda}) = \begin{cases} T_0 + \eta\dot{\lambda} & \text{for } \dot{\lambda} < \dot{\lambda}_t, \\ T_t\left(1+\frac{\eta\dot{\lambda}_t}{T_t}\ln\left(\frac{\dot{\lambda}}{\dot{\lambda}_t}\right)\right) & \text{else.} \end{cases} \tag{4.6}$$

In this formulation T_0 is the rate independent apex pressure, η a viscosity parameter, $\dot{\lambda}$ the rate of the plastic multiplier, $\dot{\lambda}_t$ a threshold rate at which the behaviour switches from linear to logarithmic and T_t the apex pressure at this threshold rate. In addition to providing mesh independent results it was also shown in [25] that this formulation can correctly capture the rate dependent tensile strength observed in ceramic spall simulations [27].

FAILURE

In the JH2 and JH2-V models failure is introduced through the scalar damage variable D, for which the rate can be defined as

$$\dot{D} = \frac{\dot{\bar{\epsilon}}_p}{\bar{\epsilon}_p^f(\boldsymbol{\sigma})}. \tag{4.7}$$

Here a (stress dependent) equivalent plastic failure strain $\bar{\epsilon}_p^f$ is used. The rate of equivalent plastic strain is related to the rate of plastic strain, which can be found as

$$\dot{\boldsymbol{\epsilon}}_p = \dot{\lambda}\frac{\partial g}{\partial \boldsymbol{\sigma}}. \tag{4.8}$$

Here $\dot{\lambda}$ is the rate of plastic multiplier and g is the plastic potential function. In 4.4.1 more information on this potential function will be given.

In the original JH2 formulation the failure strain under tension and compression is coupled through a single function. In [26] this original JH2 failure formulation was used to simulate four experiments on very similar ceramics, but each with different loading conditions. It was found that the original JH2 failure formulation was lacking flexibility in the description of failure. As it allowed the model to capture only the brittle nature of the ceramic under tension *or* the ductile nature in compression. Instead for the JH2-V model a new failure strain formulation was proposed, where failure strains in tension

Table 4.2: Upgraded JH2-V material properties for alumina ceramic

variable	value	unit	variable	value	unit	variable	value	unit
E	380.0	GPa	n	0.6	-	$\bar{\epsilon}_p^{min}$	0.00015	-
ν	0.22	-	m	0.6	-	$\bar{\epsilon}_p^{max}$	0.5	-
ρ	3890	kg/m^3	P_{HEL}	3.25	GPa	p_t	-0.1625	GPa
A	0.930	GPa	σ_{HEL}	4.50	GPa	p_c	3.25	GPa
B	0.310	GPa	η	$2.8 \cdot 10^{-5}$	GPa·s			
T	0.2	GPa	$\dot{\lambda}_t$	$4 \cdot 10^4$	s^{-1}			

and compression are independent [26]. In this formulation the equivalent plastic failure strain is given as

$$\bar{\epsilon}_p^f(\boldsymbol{\sigma}) = \begin{cases} \bar{\epsilon}_p^{min}, & p(\boldsymbol{\sigma}) < p_t \\ \left(\bar{\epsilon}_p^{max} - \bar{\epsilon}_p^{min}\right)\left(\frac{p(\boldsymbol{\sigma})-p_t}{p_c-p_t}\right) + \bar{\epsilon}_p^{min}, & p_t < p(\boldsymbol{\sigma}) < p_c \\ \bar{\epsilon}_p^{max}, & p_c < p(\boldsymbol{\sigma}). \end{cases} \tag{4.9}$$

The failure strains under tension $\bar{\epsilon}_p^{min}$ and compression $\bar{\epsilon}_p^{max}$ are used, for pressure states below the pressure p_t and above the pressure p_c. In the intermediate pressure regime the failure strain is linearly interpolated. This JH2-V material model with the new failure strain formulation is the upgraded JH2-V model.

MATERIAL PARAMETERS

The model parameters for the upgraded JH2-V material model are taken from [26] and are shown in Table 4.2. For these model parameters the ceramic behaviour under tension, compression and mixed loading can be captured properly for the alumina ceramic considered.

4.4. FINITE ELEMENT MODELLING OF SPHERE IMPACT

The previous section has introduced the constitutive models to use in simulations on ceramic material. This provides a general basis to describe the material behaviour under dynamic loading. Before the sphere impact test can be simulated the numerical framework has to be completed.

The first modelling choice to make when using FE simulations is whether to use a 2d or 3d formulation for the problem. Many authors choose to simulate sphere impact in a 2d axisymmetric formulation [7, 10, 28, 29]. The main benefit is that the computation time is low. The problem of this 2d formulation is, however, that it is only valid as long as all failure phenomena are fully axisymmetric. The experimental results from Section 4.2 have shown that this is not true, since radial cracking is not an axisymmetric failure mechanisms. Therefore it is recommended to use 3d simulations when comparing to experimental results in section 4.5. However, these 3d simulations will take considerably more computation time than when using a 2d axisymmetric formulation, but it is more important to capture all failure mechanisms. The 2d simulations are not abandoned completely as they will be used to quickly study some initial model choices.

In this chapter the implicit Hilber-Hughes-Taylor-α (HHT-α) time integration scheme will be used [30]. One advantage of the implicit HHT-α method is that equilibrium is achieved at every time step. In addition, a critical time step size, typical for explicit methods, does not exist in the implicit method because it is unconditionally stable. Furthermore, the method includes some energy dissipation, which may reduce oscillations that are generally produced in contact problems [31]. Since the method is unconditionally stable one can take much larger time steps compared to explicit time integration schemes. This can greatly reduce the total computation time. However, the disadvantage is that implicit methods require iterations to be performed in each time step to find the equilibrium state. This convergence process will be faster if the systems behaves (near) linear within one time step, but may be slower if the system is highly non-linear within one time step. To keep the simulations robust, the time step is adaptively chosen, increasing or reducing the time step size depending on the number of required iterations. As the convergence behaviour of the system depends on the level of non-linearity, some model features will be carefully examined in this section. The goal is to keep the framework simple and fast, without losing too much accuracy.

To reduce the non-linearity in the system, the numerical framework is critically reviewed. Any model introduced by the user to describe for instance the material or the contact can introduce a non-linearity. There may be a general physical justification for these non-linearities, but since the current chapter deals specifically with the sphere impact test it is worth examining whether some of these non-linearities can be ignored.

The first source of non-linearity under consideration is the constitutive model. The pressure dependency in the material strength and the softening of the yield stress are important sources of non-linearity. However, the material strength is well established and material failure is required in the problem under consideration. Therefore both non-linearities can not be removed from the system. There is however another material feature which has not been introduced in Section 4.3. This is material bulking or dilatancy, which is the tendency of a material to expand while failing. Some ceramic material models, including the JH2 model, offer the possibility to include this behaviour. So it is possible to add bulking to the material model, but at a cost of introducing an additional non-linearity. The necessity of material bulking in sphere impact will be investigated in Section 4.4.1.

A second source of non-linear behaviour is the contact between projectile and target, for which a penalty stiffness formulation is used. Obviously this source of non-linearity can not be ignored, since the sphere impact is a contact problem by nature. However, one can choose how to describe the contact. More specifically, one may or may not include contact friction. Whether this model feature is required in sphere impact will also be investigated in Section 4.4.1.

After considering material bulking and contact friction the numerical framework is almost complete. Two more verifications are performed. The first one is to see if the upgraded JH2-V model indeed provides mesh independent results. The second and final verification is to perform a 3d sphere impact simulation in the proposed framework. This will show that all failure mechanisms described in Section 4.2 are properly captured. After this final verification the numerical framework for sphere impact is completed and can be used with confidence in the remainder of this chapter.

4.4.1. BULKING

When ceramic material fails and undergoes shear deformation it has a tendency to expand. This behaviour is referred to as dilatation or bulking. The result of dilation or bulking is an inelastic increase of volumetric strain. Most ceramic material models allow for this dilatation effect. The original JH models have an explicit bulking formulation, increasing volumetric plastic strain as damage in the material grows. A more suitable approach when using an implicit time integration scheme is to include a volumetric deformation in the material flow rule [17, 32], this was also shown to work for the JH2 model [33].

In a plasticity model the direction of plastic flow can be defined through the plastic potential function g, as can be seen from (4.8). Any volumetric component of plastic flow should therefore be included in the potential function. A simple plastic potential function which includes a volumetric component is based on the Drucker-Prager (DP) model, where the potential may be defined as

$$g(\boldsymbol{\sigma}) = \sigma_{eq}(\boldsymbol{\sigma}) - \alpha p(\boldsymbol{\sigma}). \tag{4.10}$$

In this potential function σ_{eq} is the equivalent stress, p the pressure and α a variable to scale the volumetric effect. It is easy to observe that volume preserving flow is found for $\alpha = 0.0$. In the DP model there are a number of ways to define the α variable, one possible relation [34] is given as

$$\alpha = \frac{6\sin\psi}{3 - \sin\psi}. \tag{4.11}$$

This sets a direct relation between the value of α and the angle of dilatancy ψ.

The potential function from (4.10) is simple but may be unphysical. This is because the volumetric plastic strain is unbounded in this formulation, it keeps on increasing as long as there is plastic deformation. To limit the amount of volumetric plastic flow the potential function (4.10) can be modified to

$$g(\boldsymbol{\sigma}) = \sigma_{eq}(\boldsymbol{\sigma}) - (1 - D)\alpha p, \tag{4.12}$$

where the volumetric component of plastic flow gradually reduces with damage and eventually disappears when the material reaches full failure at $D = 1.0$. This is similar to the model presented in [32] where the dilation effect is also scaled with damage. It is also in line with the concept of a critical state in soil mechanics, where shear deformation may reach a stable state without any further increase of volume [35, 36].

The sphere impact experiment from Section 4.2 is simulated in a 2d axisymmetric strain formulation. The potential function from (4.12) is used. As presented in the previous subsections the upgraded JH2-V model is used for the ceramic material and the Johnson-Cook model for the steel projectile. Results of 200m/s sphere impact on a 9mm ceramic tile when using the potential function are presented in Figure 4.6. Here the dilation angle is varied from $\psi = 0°..25°$ and the results are presented 10μs after impact. The first observation is that the main cone crack remains very similar for all angles of dilatancy. This is the most important observation, as cone cracking is the main failure mode in a ceramic target under sphere impact. The simulation with $\psi = 0°$ does show a partial second cone crack. For other values of dilatancy this second cone is suppressed

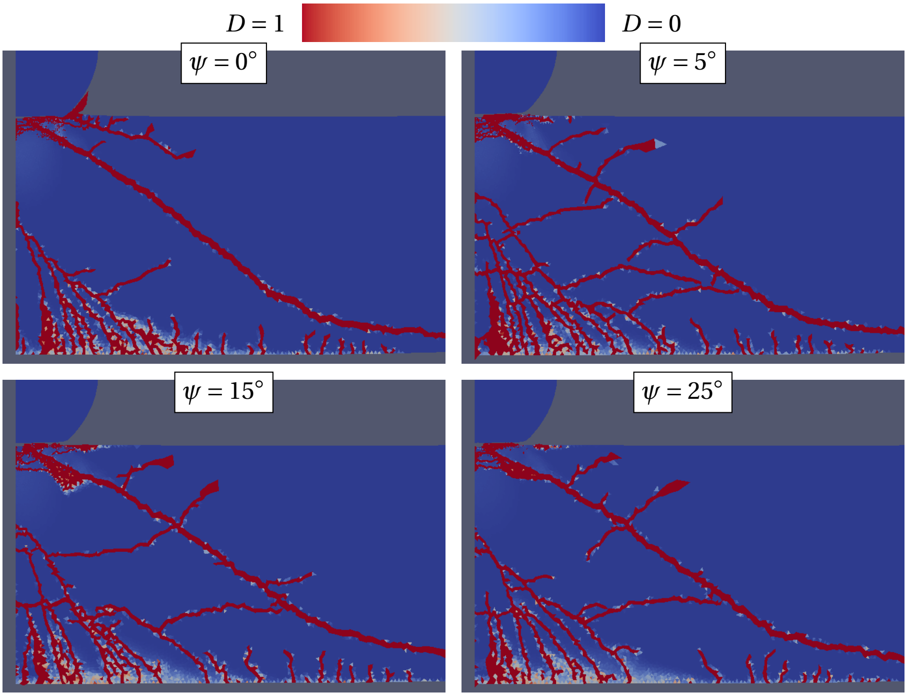

Figure 4.6: Effect of material bulking explored, potential function from (4.12) is used. The damage variable $D \in [0..1]$ is shown after 10.0μs of simulated time. A clear cone crack forms in all cases. Increasing the angle of dilation has only minor consequences for the failure mode, as it does not affect the primary cone crack.

and only surface damage remains. A second observation is that failure on the back of the target is present for all cases, albeit with some slight variations. It can be found that the number of cracks reduces as the dilatation angle increases and the damage is more diffuse for a high dilatation angle, although differences are small. This failure at the target back side should have been radial cracking, but in the 2d axisymmetric formulation this can obviously not be captured. Differences in the backside failure are therefore not too important for this initial consideration. A third observation can be made on the lateral cracking in the specimen. The location and number of lateral cracks appears to change when a different value of the bulking is chosen. There is however no clear trend in the lateral crack formation. Also this mechanism is of less importance because it appears during unloading. Overall it can be found that there are some small changes in the failure of the ceramic target when altering the dilation angle from $\psi = 0°..25°$, but no significant changes are found in the main failure mode.

In literature multiple values for dilatancy in ceramic material are given. Some authors choose to have a zero dilatancy [10, 17, 37], where others [32] choose a value $\psi = 15°$. This fits within the considered range in the current section. The results from Figure 4.6 showed only minor effect of dilatancy when using $\psi = 0°..25°$. Combining these findings leads to the conclusion that bulking is not important for the considered sphere impact experiment. It is important to note that this does not mean that bulking should never be included in the upgraded JH2-V material model. It simply shows that its effect is limited under sphere impact, quite possibly because there are no large shear deformations under these conditions. Any following simulations will be performed with volume preserving plastic flow (i.e. $\psi = 0°$). This reduces the non-linearity in the system and will aid the global convergence process of the implicit time integration scheme.

4.4.2. CONTACT FRICTION

As a projectile comes in contact with a ceramic target, a reaction force is exerted on the projectile. This reaction force slows down the projectile and may eventually defeat the threat of the projectile. In the contact of projectile and target the main forces are transmitted normal to the contact surface, however, sliding of the projectile along the target surface can occur during the impact event. This will generate frictional forces in tangential direction to the contact surface. Such a frictional force can be captured by introducing a Coulomb friction in the penalty stiffness contact model [38]. The question to be answered in this subsection is to determine if friction can be neglected or if it significantly changes the simulation results. Figure 4.7 shows the damage found in a 2d axisymmetric simulation, 10μs after being impacted by a steel sphere with an impact velocity $v = 200$m/s. The figure on the left is obtained with a coefficient of friction $\mu = 0.0$ and the one on the right with $\mu = 1.0$, whereas a typical coefficient of friction between steel and ceramic would be $\mu = 0.5$ [39–41]. The primary cone crack is very similar in both cases. A small secondary cone forms in the frictionless simulation, while only surface damage is found in the results with friction. Minor difference is found in the backside failure, which appears more extensive in the high friction case. Also lateral cracks are more frequent in the high friction case. The simulation results show that even if the coefficients of friction are very different, the results obtained are similar. Therefore, it can be concluded that friction does not need to be included in the current simulation of a sphere impact test. The results obtained in the following sections are therefore obtained without friction (i.e. with $\mu = 0.0$), which will simplify the simulations.

4.4.3. MESH DEPENDENCY

The upgraded JH2-V model presented in Section 4.3.2 is used for the simulations in the current chapter. In Chapter 2it was shown that this model can be used to give mesh independent results, thereby preventing spurious localization and the mesh bias effect. It is good practice to show that the model indeed provides mesh independent results for the current application. For sphere impact simulations mesh bias is of particular interest, as the absence of bias will confirm the validity of the predicted cone crack angles and paths. To study mesh dependency for the sphere impact problem the 2d mesh from 4.4.1 is used as a basis. Three variations to the mesh for sphere impact are considered. The first variation is a refinement or coarsening of the top surface of the target mesh. The second variation is again a refinement or coarsening of the mesh, this time for the internal element size of the ceramic target. The third and final variation is made by applying a bias in the mesh. The bias is applied through the input geometry of the mesh. Parallel lines spaced $1mm$ apart run from the surface to $3.6mm$ depth. The angles of these lines vary between the meshes from $45° - 70°$, with $1°$ increments. An example mesh with a

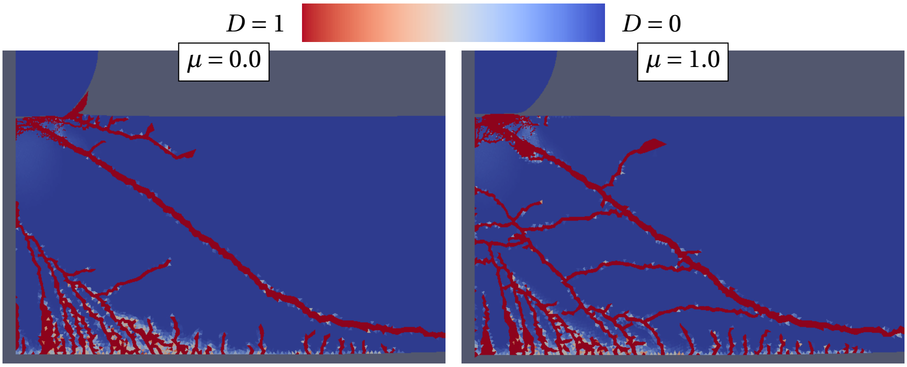

Figure 4.7: Effect of contact friction explored. Damage parameter $D \in [0..1]$ in ceramic target is shown 10μs after being impact by a steel sphere with initial velocity $v_0 = 200$m/s. Figure on the left shows the results obtained with a coefficient of friction $\mu = 0.0$, figure on the right is obtained with $\mu = 1.0$. Resulting cone cracks are highly similar and show that friction can be neglected for these simulations.

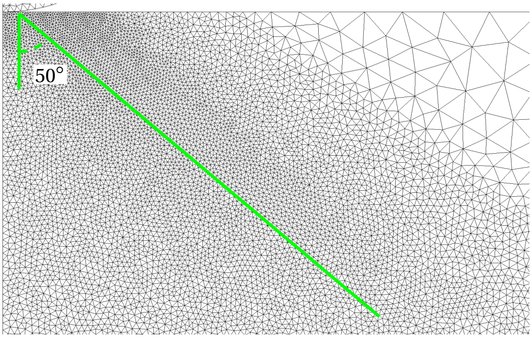

Figure 4.8: Mesh with a bias of 50°. Parallel lines running from the target surface are clearly visible.

bias of 50° is shown in Figure 4.8. The projectile mesh remains unchanged in all these mesh variations.

Figure 4.9a shows the traced paths of the cone crack tips, obtained for the first mesh variation in surface element size. The crack tip is traced for the first 1μs of the simulated time, which is enough to see initiation and some propagation. It is easy to observe that there is a considerable effect of the surface mesh size. It is found that the cone angle increases with surface mesh size. The cone angle can be measured to vary from 53° for the $0.0125mm$ surface mesh size to 61° for the $0.1mm$ surface mesh size. Although the angle changes between the meshes, the cone crack length is similar. For the biggest element size considered, only a ring crack initiates and the cone crack does not develop. This is because the stress field near the contact surface experiences high gradients in the stress field. These high gradients are not well captured by the linear triangular elements used. To get a reasonable description of these high gradients a fine mesh is required.

Figure 4.9b shows the traced paths of cone cracks, obtained for five different internal mesh sizes. Again the crack tip path is shown for the first 1μs of the simulated time. The element size at the target surface is chosen as $h = 0.050$mm and is equal for all cases. These results show a very similar cone crack path and initiation point for all five cases. The cone crack length does appear to be a function of internal element size, as finer elements lead to a longer cone crack.

Finally Figure 4.10 presents the cone crack angles measured in meshes with a bias. The bias range considered here is 45° – 70°, which encompasses the range of expected cone angle. For the series of simulations the resulting cone angle is found to vary between 56° – 63°, measured from origin to tip of the cone crack. When the angle of the bias is near the average cone angle of 60° one may find a small bias effect. The cone angles found for a bias angle below the average cone angle appear to be below the average. For bias angles above the average cone angle the opposite is found. However, this effect may be limited to a few degree change in cone angle and is not consistent for all bias angles. The range of measure cone angle is also much smaller than the bias given, indicating there is a limited effect of mesh bias.

Despite using the regularizing upgraded JH2-V material model there is some visible effect of the mesh on the cone crack initiation and propagation. Variation of the target surface mesh is found to have the largest effect. Smaller effects are found for the internal mesh size and bias. It is concluded that the mesh at the target surface should be sufficiently fine, but the internal mesh can be coarser. In the current chapter the comparison to experiments is only done qualitatively in Section 4.5. When performing a quantitative comparison one should consider the ±3° spread in simulated cone angle due to bias.

4.4.4. CHARACTERISTIC BEHAVIOUR

Sphere impact is a highly dynamic event. Failure of the ceramic is time dependent and failure mechanisms may interact. To give a good idea of what might occur in a ceramic under sphere impact a 3d simulation is performed and the results are analysed. This will also show whether all failure mechanisms found in 4.2 are captured properly, thereby validating the numerical framework. Figure 4.11 shows the 3d damage results for a 9mm thick ceramic target after being impacted at 300m/s, for different points in time. The projectile velocity is also plotted as a function of time. The results at 1.365μs clearly show an initiated cone crack (orange arrows) as well as a quasi-plastic zone (grey arrow). The quasi-plastic zone is generally difficult to see but in the simulations it may show up as a light blue discolouration, indicating a low level of damage. At 5.704μs the cone crack has extended further in the ceramic material. Radial cracks are also visible (blue arrows), both on the ceramic back surface and propagating in vertical direction along the central axis. This confirms that a 3d simulation is indeed required since radial cracking is expected. At 5.704μs the projectile has reached a zero velocity and the unloading phase begins. During the unloading phase lateral cracks form (green arrows), as is clearly visible in the snapshot at 7.409μs. Contact between target and projectile is lost around 7.409μs, which can be found from the constant velocity of the projectile after this point in time. The lateral cracks still continue to grow after the projectile loses contact. This can be found from the snapshot taken at 10.0μs, showing the fully grown lateral cracks which separate the cone into multiple parts. For this particular impact velocity an additional failure mechanism is found as a ring crack on the target back surface

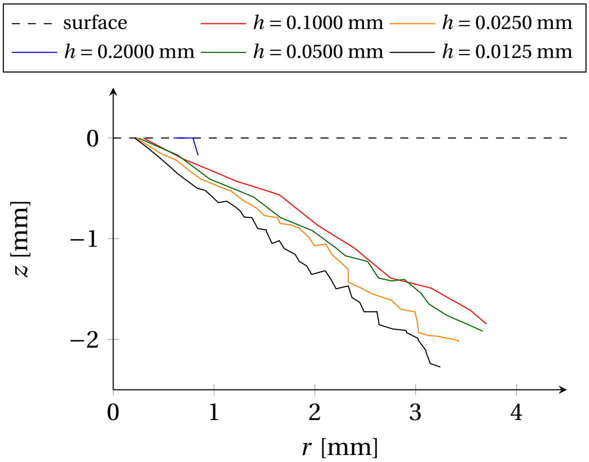

(a) Mesh dependency study, variable element size h at the contact surface. The target interior element size is the same for all cases. For a coarser mesh the radius of the surface ring crack is larger, as is the cone crack angle.

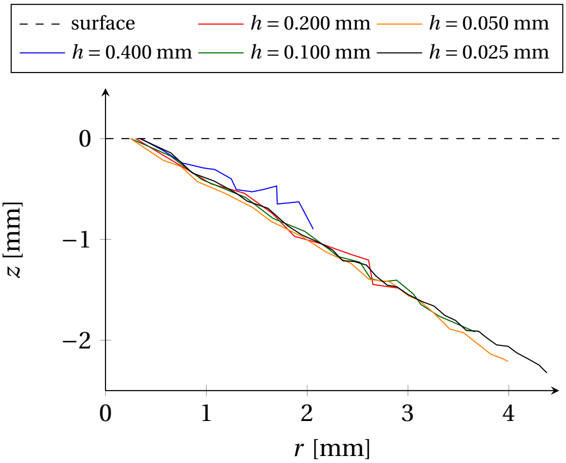

(b) Mesh dependency study, variable element size h in the target interior. The target surface element size is the same for all cases. The cone crack direction is found to be insensitive to the mesh size, but the crack length is.

Figure 4.9: Mesh dependency study on cone crack initiation and propagation. Cone crack paths are shown for different mesh sizes h.

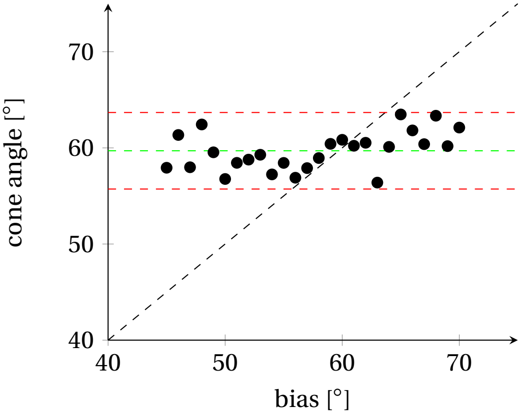

Figure 4.10: Cone crack angles obtained from the simulations with mesh bias. Elements are aligned to a given angle and the cone crack angle is measured. The considered bias range 45° – 70° is chosen as the expected cone angles are within this range. The green dashed line shows the mean value for the results, the red dashed lines indicate the 95% confidence interval of 56° – 63°.

(white arrow). This ring crack is generally not found. The snapshots from Figure 4.11 show how the failure mechanisms occur in time. This timing is very typical and all considered test cases show this order of failure. That is: first cone cracking and quasi-plastic zone, then radial cracking and last lateral cracking. The results of the current simulation show that the upgraded JH2-V model can capture all failure mechanisms expected in a sphere impact experiment. A thorough comparison of the failure mechanisms for other impact velocities and tile thicknesses will be presented in the next section.

4.4.5. CONCLUDING REMARKS

In this section the numerical framework for the sphere impact simulations was established. This first part of the section considered two sources of non-linear behaviour. The first was the possible addition of material bulking in the upgraded JH2-V material model. The second was including Coulomb friction in the contact between projectile and target. Both these model aspects were not found to have a considerable effect on cone cracking in the ceramic target under sphere impact, which is the main failure mode. Minor and negligible changes in failure on the target back surface and changes in lateral cracking were also found.

To complete the numerical framework for sphere impact FE simulations a final verification and validation was performed. The verification was to see if there is any mesh-dependency found in the simulation results. Although the upgraded JH2-V model was used, which was shown in an earlier contribution to provide mesh-independent results, some mesh dependency was observed. The greatest effect on the simulation results was found by changing the surface mesh, leading to variations in cone crack length and angle. Changing the internal mesh size or providing bias in the mesh was found to have only minor effect. In the study on mesh bias it was observed that the bias effect on the cone crack angle could be ±3°. The validation was to perform a full sphere impact sim-

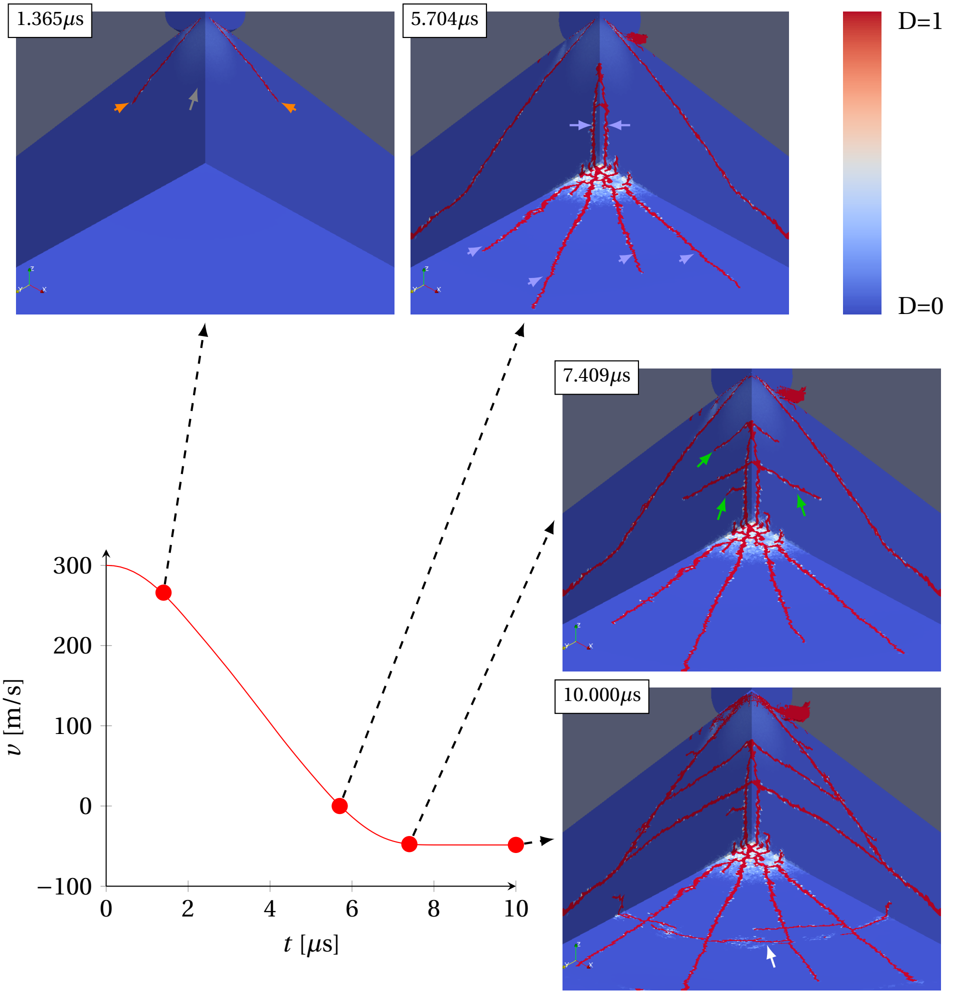

Figure 4.11: Velocity of the projectile plotted for a 3d sphere impact simulation. Damage variable $D \in [0..1]$ in the ceramic is shown at four points in time. The first point is just before radial cracking starts, the second point is when the projectile reaches zero velocity. The third point is (roughly) when contact is lost and the fourth when the simulation is complete.

ulation in 3d, to confirm that all failure mechanisms could be captured. These results were also analysed to determine the timing of the failure process. Overall, the simulation results showed that all failure mechanisms could be captured in the current numerical framework. It is therefore concluded that all following sphere impact simulations should be performed in 3d, with the upgraded JH2-V model without material bulking and without contact friction.

4.5. RESULTS

As presented in Section 4.2, the experiment under consideration is sphere impact where three different velocities are considered for two target thicknesses. The material models and parameters presented in sections 4.3.1 and 4.3.2 are used. Similar to the 3d simulations performed in the final part of the previous section, quarter symmetry will be used. The simulations only consider the first 10μs after projectile impact. This period of time is sufficient to reflect the impacting steel sphere [42] and to induce the damage and fracture processes in the ceramic tile.

Figure 4.12 shows the scalar damage value predicted in the simulations, ranging from intact (blue) to fully damaged (red). From top to bottom the impact velocity is chosen as 100-200-300m/s. The left column holds results for the 9mm thick ceramic tile and the right column for the 13mm thick ceramic tile. It is possible to see cone and lateral cracking in these frontal images of the impacted ceramics, as well a quasi-plastic zone and the vertical propagation of radial cracks through the thickness of the ceramic. Figure 4.13 shows the same impacted ceramics, but now seen from below. Radial cracking on the ceramic back surface is also visible from this viewpoint. Both the 9 and 13mm thick targets show more failure in the ceramic as the projectile velocity increases. For 100m/s no cone cracking is visible and only the 9mm thick tile shows radial and lateral cracking. The 13mm thick tile only shows surface damage and some slight discolouration in the sub-surface zone, but no cracking. The presence of cone cracking in the 9mm tile but not in the 13mm tile was expected for some impact velocity. This is because the amplitude of a spherical wave decays with distance squared. Therefore the stress wave amplitude will be more than halved for the 13mm thick tile. For 200m/s impact both tile thicknesses show cone cracking, although this cone only fully develops in the 9mm thick tile. For the 13mm tile the cone crack does not extend through the ceramic tile. It is also observed that the final part of the cone crack is found to extend towards the impact surface rather than away from it. Step by step analysis of the impact simulation has shown that the upward part of the cone crack forms when the projectile starts to rebound and the target is unloaded. Radial and lateral cracking is found in both tile thicknesses. For the 9mm thick tile the lateral cracks are found to separate the cone in three parts. The 300m/s impact cases show cone, lateral and radial cracking. Again the thin 9mm tile shows more damage than the thick tile. The thin tile shows additional ring/cone cracks at the impact surface, two lateral cracks and even a ring crack forming on the target back surface and within the formed cone. Some element inversion is also visible for both ceramic tiles impacted at 300m/s.

Similar to Section 4.2.1 the failure mechanisms were collected in a table. This is done in Table 4.3, in which the experimental results from Table 4.1 are repeated once more for easy comparison. The 9mm ceramic tile results agree very well between experiment and

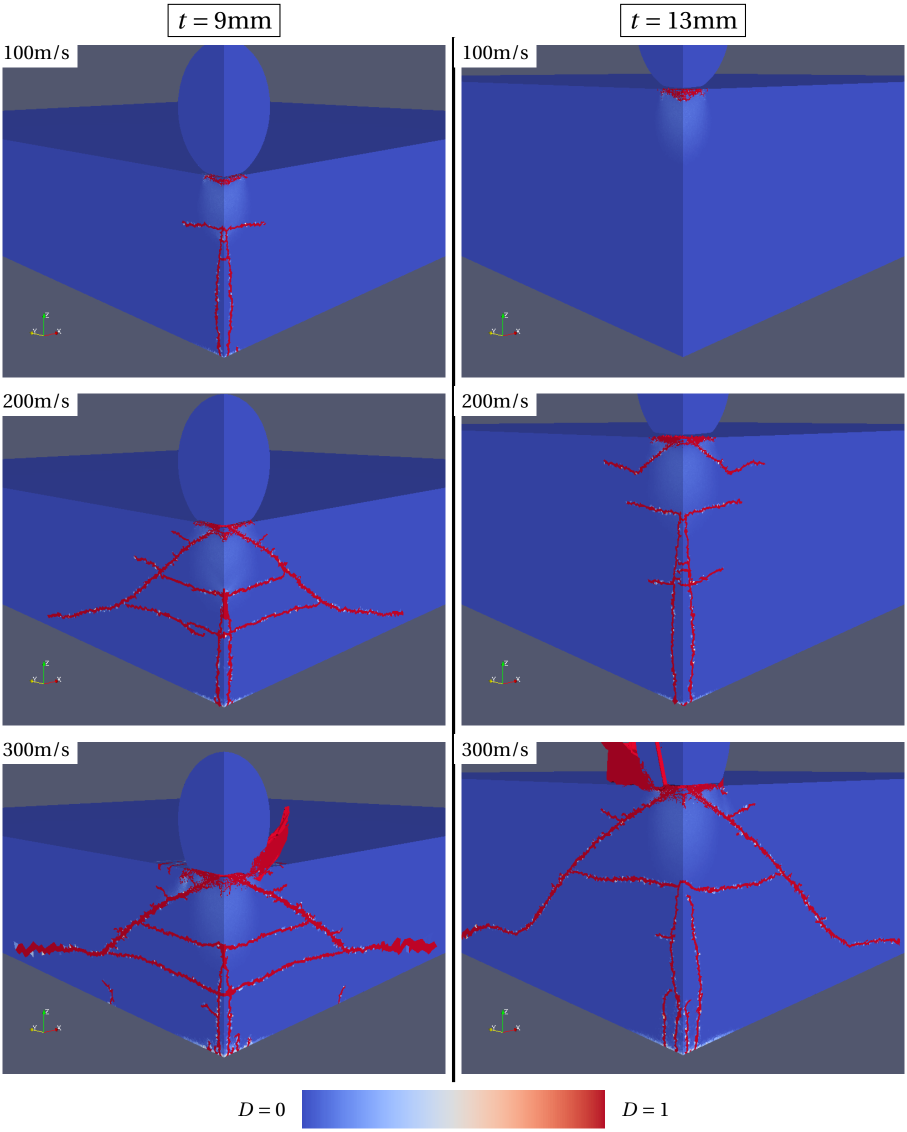

Figure 4.12: Sphere impact simulations performed in 3d with the same set-up as the experiments from DRDC. The simulations are terminated after 10μs of simulated time.

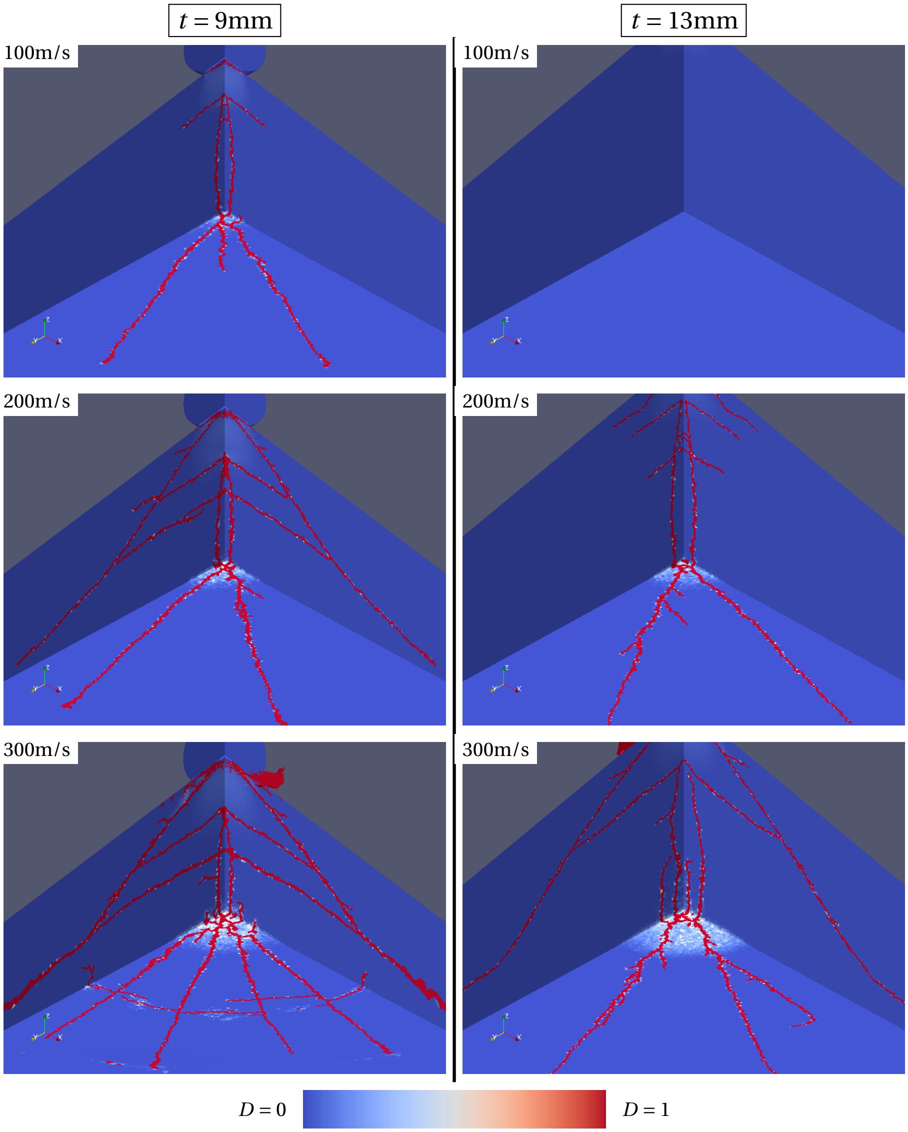

Figure 4.13: Sphere impact simulations performed in 3d with the same set-up as the experiments from DRDC. The simulations are terminated after 10μs of simulated time.

Table 4.3: Experimental results from Table 4.1 compared to simulations, based on failure mechanisms. For each experiment the ✗and ✓symbols are used to show if the failure mode was found. The ★symbol is used if the test data was not available. The simulations only have a single outcome. For the 200m/s impact on a 13mm tile the simulation shows a partial cone crack.

9mm	Experiment, cracks			Simulation, cracks		
velocity	cone	radial	lateral	cone	radial	lateral
100m/s	✓✓✓	✓✓✓	✓✓✓	✗	✓	✓
200m/s	✓✓✓	✓✓✓	✓★✓	✓	✓	✓
300m/s	✓✓✓	✓✓✓	✓✓✓	✓	✓	✓
13mm	Experiment, cracks			Simulation, cracks		
velocity	cone	radial	lateral	cone	radial	lateral
100m/s	✗✗	✗✗	✗✗	✗	✗	✗
200m/s	✓✓✓	✓✓✓	✗✓✗	✓/✗	✓	✓
300m/s	✓✓✓	✓✓✓	✗✓✗	✓	✓	✓

simulation. The only difference is the lack of cone cracking for the 100m/s simulation, which was clearly present in all experiments. For the 13mm ceramic tile there is again agreement in terms of failure mechanisms. Only exception is that all three experiments for 13mm and 200m/s show fully developed cone cracks, while only a partial cone crack was found in the simulation. Also for the 200 and 300m/s impact it is difficult to conclude that the lateral cracking is captured correctly, as the experiments do not seem to give a clear result for this mechanism.

Overall there appears to be good agreement between the failure mechanisms observed in simulations and experiments. The validation of the upgraded JH2-V model to be used in sphere impact simulations is now concluded. The models and methods can now be used to study the failure mechanics in more detail than what the experimental results allow.

4.6. DISCUSSION

In the current section conical and radial cracking of the ceramic target are analysed further using finite element simulations of sphere impact. Lateral cracking will also be briefly mentioned, but it is not considered to be an important failure mechanism in the projectile interaction as it forms during and after unloading.

4.6.1. CONE CRACKING

The process of cone cracking will be investigated further in the current section. For this purpose, sphere impact tests are simulated in the same numerical framework as before, but now impact velocities are ranging from 100 to 300m/s with 10m/s increments. In post-processing, the cone crack tip path was traced in the same way as was done in Section 4.4.3. This traced crack tip path gives information on the crack length during and after the impact event. The cone crack length is defined as the distance from point of initiation to the tip. The simulated cone crack length as a function of time for the 9 and 13mm tiles are shown in Figure 4.14. The results are shown up to 6μs, which is approximately when the projectile velocity is reduced to zero and when the unloading phase begins. After this point in time the cone crack may still grow, but as was seen in Figure 4.12, this can also be in an upward direction. This may give a false impression on cone crack length, hence the propagation is only considered up to 6μs.

For both the 9 and 13mm tile thicknesses cone cracking was first observed at an impact velocity of 170m/s. This suggests that, for the current model parameters, the impact velocity required for cone crack initiation is constant and independent of the tile thickness, which agrees with [10]. The current simulation results show that only a partial cone crack is formed for the 170m/s impact velocity. This partial cone initiates and grows roughly in the first μs after impact. The partial cone cracks are only a few millimetres in length and do not cause full failure of the ceramic target. As impact velocity increases one may find that the partial cone crack grows for a longer time, reaching an increased crack length. At a threshold impact velocity an interesting transition takes place, where the partial cone cracks start to grow again after an arrest phase. Increasing the velocity beyond this threshold velocity eventually even removes the arrest phase and the cone cracks are found to grow for the full 6μs. For the 9mm thick ceramic tile, the first restarted cone crack is found at an impact velocity of 200m/s, for the 13mm ceramic tile the threshold velocity is 230m/s. For the 9mm tile impacted at 200m/s one may find that the cone crack shows an arrest phase of a few μs, before continuing to grow after 4μs. At 210m/s impact there is also a small arrest phase and even the 220m/s impact case shows minor signs of arrest. Any impact velocity above that shows a continuously growing cone crack. For the 13mm thick ceramic target impacted at 230m/s, there may be a slight crack arrest just after 2μs but certainly not as convincing as for the 9mm target. Again for higher impact velocities the cone crack develops gradually without crack arrest. For both tile thicknesses the growth of the cone crack appears to slow down after some distance. This can be related to the way the crack length is measured, which is from base to tip. This gives a correct length for straight cracks, but starts to deviate when the crack is curved or with a sudden change in cone angle. For the simulations the crack may change angle when it grows closer to the back surface of the tile, as is clearly seen in Figure 4.12.

The cone cracking results in the current section do not show why the simulations in the previous section do not match the experiments. However, they do reveal an interesting difference in cone crack initiation and propagation. The initiation was found to be independent on the tile thickness, while the propagation phase of the cone crack was. This shows that there is a correlation between cone crack propagation and wave propagation in the target, which can therefore be affected by applying a backing to the system. If one tries to suppress cone crack initiation an armour benefits from a layer on the front surface.

4.6.2. RADIAL CRACKING

In the simulations radial cracking in the ceramic target starts after cone cracking is initiated. This process is expected based on wave mechanics, since cone cracks are found to form even before the first pressure wave reflects on the back surface. After initiation of the radial cracks they are found to extend both in radial and vertical direction through the ceramic tile.

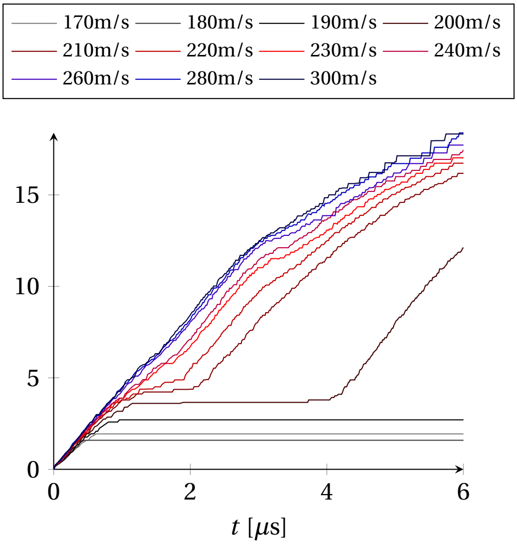

(a) Results for 9mm thick ceramic tile.

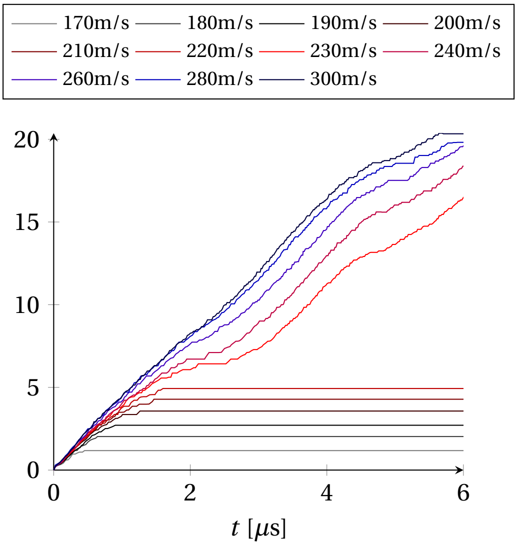

(b) Results for 13mm thick ceramic tile.

Figure 4.14: Cone crack length as a function of time, for variable impact velocity.

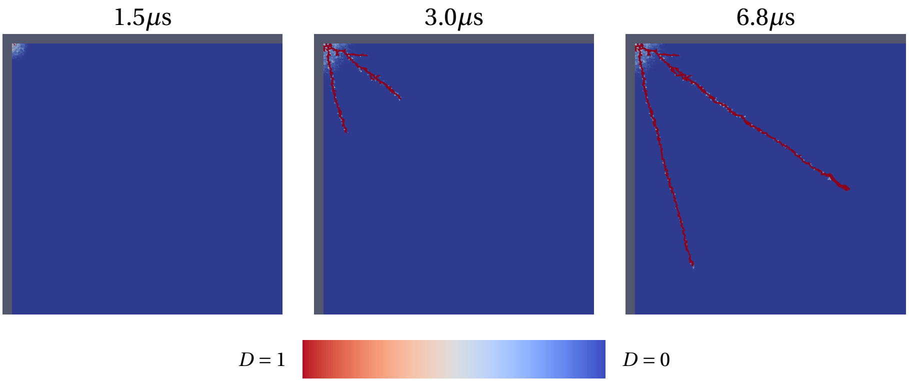

Figure 4.15: Sphere impact results for 9mm thick ceramic impacted at 200m/s. The damage is shown on the bottom of the ceramic target, the axis of impact is at the top left of the figure.

At first, radial crack propagation in radial direction is considered. Figure 4.15 shows snapshots for the 9mm ceramic tile impacted at 200m/s. The images show the damage on the target back surface, where quarter symmetry is used with the axis of impact in the top left corner. After 1.5μs the damage is found to start around the axis of impact, but no clear radial cracks exist yet. In the succeeding images the radial cracks have formed and extend in radial direction. In this particular impact case there are two radial cracks forming, but other tile thicknesses and impact velocities may show one, three or even four radial cracks. Generally more radial cracks are found if the impact velocity is higher, which could also be seen before in Figures 4.3, 4.13 and in literature [8, 43].

In second, the growth of the radial crack through the thickness of the tile is considered. Figure 4.16 shows snapshots of the 9mm ceramic tile impacted at 200m/s, this time a side view of the 3d result is presented. The top row shows the damage in the material, the bottom row the equivalent plastic strain. The quasi-plastic zone in the ceramic target just below the point of impact is clearly visible in the bottom row of figures. One may find that no clear radial cracking is found after 1.5μs but only a small amount of damage on the target back side, which is similar to the results in Figure 4.15. Between $1.5-3.0\mu$s after impact the radial crack grows and extends through the thickness of the ceramic tile. From the plastic strain plot it can be found that the crack stops roughly when it enters the quasi-plastic zone. This is likely related to the compressive stress state experienced in this zone. It is interesting to note that a lateral crack forms in this same location. This can also be observed in the simulation results from the previous section in Figure 4.12 and may explain why the experiments never show a radially fragmented cone tip.

Similar to the cone cracks it is possible to trace the radial cracks. Figure 4.17 holds the traced radial crack lengths as function of time. Radial crack length is defined here as distance from axis of impact to the radial crack tip. Again the results are presented for both the 9 and 13mm thick ceramic tiles. Unlike the cone cracks there is a considerable time after impact before the radial cracks start to grow. The vertical dotted line indicates when the compressive wave of impact first reaches the target back surface. This is the theoretical lower bound for radial crack formation. The cracks in the simulations do not

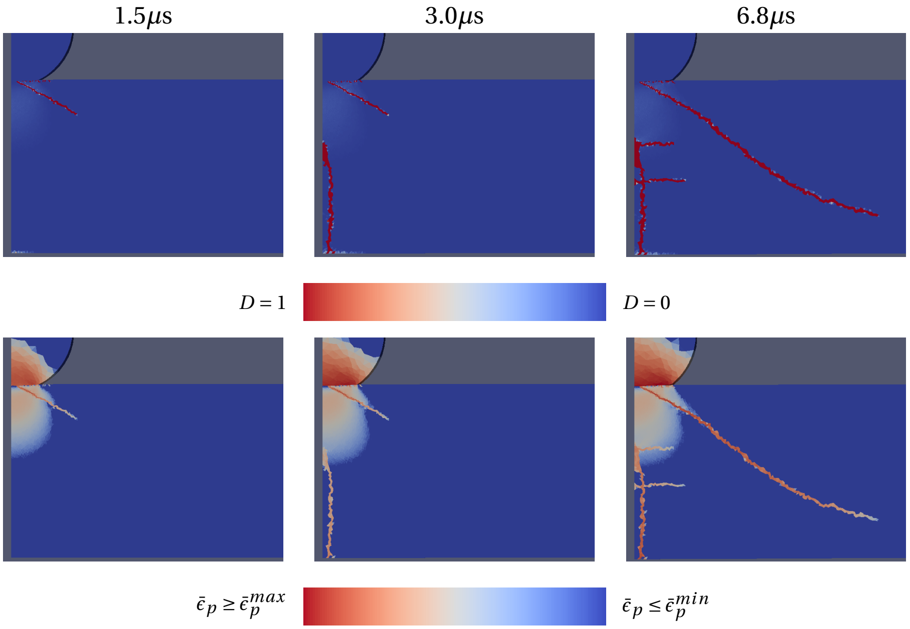

Figure 4.16: Sphere impact results for 9mm thick ceramic impacted at 200m/s. The deformed geometry is shown with (top) damage and (bottom) equivalent plastic strain. The damage is plotted on a linear scale, the equivalent plastic strain on a logarithmic scale.

form at this minimum, some time is needed before the tensile stress amplitude reaches the material strength and radial cracking is initiated. When a higher impact velocity is used the radial cracks form sooner, this holds true for both ceramic tile thicknesses. This was to be expected since a higher impact velocity increases the stress wave amplitude and should therefore require less rise time before radial cracking. After radial cracks are initiated the propagation velocity appears to be independent of the initial impact velocity. Crack arrest is not found in the radial crack graphs, although a slight reduction in crack growth rate is observed just after initiation for all cases. The results presented in Figure 4.17 are for an impact velocity 170-300m/s, which is the range in which cone cracking is observed. Radial cracks are however found below 170m/s, for the 9mm thick tile the first radial cracks appear at 60m/s impact and for the 13mm tile at 120m/s. This is in line with the experimental observations of the previous section, where 9mm thick tiles impacted at 100m/s showed radial cracking, but 13mm thick tiles did not. The observation that radial cracks initiate at a lower velocity than cone cracks confirms that a 3d simulation is necessary to study cone cracking in these unsupported sphere impact tests.

The results in Figure 4.17 can also be combined with the cone crack tip results from Figure 4.14. To compare both the cone crack tip radial coordinate is plotted (not the cone crack length). The cone crack tip positions are shown as dashed lines in Figure 4.17. Only two extremes of cone crack length are shown. The first cone crack lengths are for the lowest impact velocity still showing a propagating crack after 6μs, which is found at 200m/s for the 9mm thick tile and at 230m/s for the 13mm thick tile. The second cone crack lengths are those found for an impact velocity of 300m/s, for both tile thicknesses. One may find that radial cracks are initially only internal to the cone, but they pass and extend beyond the cone crack after some time and distance. When analysing experimentally tested ceramic targets after the impact event, this means the radial cracks will extend into the tile, in a seemingly uninterrupted path. One may be tempted to assume that this means the radial cracks are formed before the cone crack, but the simulation results show the opposite. Currently it is not yet possible to validate this claim through experiments.

4.6.3. GENERAL BEHAVIOUR

Initial results in this section showed damage plots for a 9mm thick ceramic tile impacted at 200m/s. This clearly showed that a cone crack initiates before radial cracks do. It also revealed that the radial cracks grow out and upward into the ceramic tile. The radial cracks stop to grow up as soon as they reach the quasi-plastic zone, which is also where a lateral crack is found to form during unloading. These observations are similar for all tile thicknesses and impact velocities for which cone and radial cracking is found. After the sphere impact test a ceramic cone has formed, with a separated but intact tip and a radially fragmented base. This is confirmed by both the numerical and experimental results from Section 4.5.

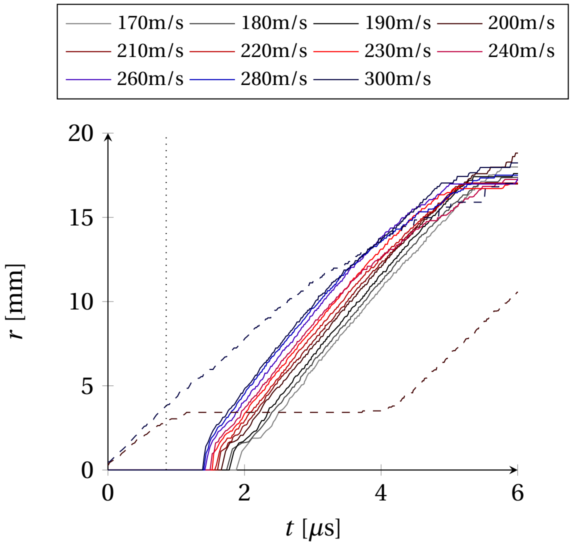

(a) Results for 9mm thick ceramic tile.

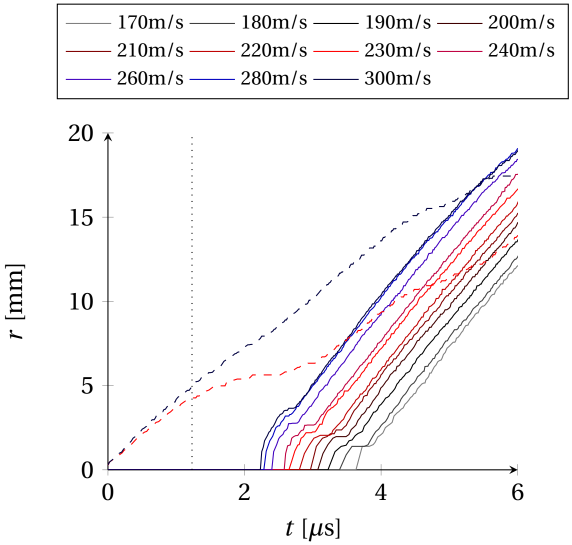

(b) Results for 13mm thick ceramic tile.

Figure 4.17: Radial crack length as a function of time, for variable impact velocity. Dashed lines show cone crack position, dotted vertical lines indicate when the compressive wave of impact first reaches the target back surface.

4.7. CONCLUSIONS

The upgraded viscosity regularized Johnson-Holmquist-2 material model was used to simulate ceramic material under impact in 3d. A numerical framework was specifically set-up for sphere impact simulations. Initial 2d simulation results revealed that material bulking and contact friction do not play a dominant role in sphere impact and these model characteristics were therefore ignored in further analyses. The mesh independency of the model results was also investigated. Although the JH2-V model is known to regularize the solution, small effects of the mesh on the results were found. As a final verification a characteristic 3D sphere impact test was performed. This showed that all failure mechanisms could be captured in the current framework and also gave some insight in the timing of failure. It was concluded that the framework for succeeding sphere impact simulations should be in 3D, but bulking and contact friction can be neglected.

Using the numerical framework presented in the first part of this chapter, the sphere impact experiments was simulated. Qualitative comparison of sphere impact simulations and experiments showed good agreement. Cone cracking could be captured in the simulations, but there was a mismatch on the impact velocity for which the cone cracks first appeared. However, radial and lateral cracking was properly captured in the simulations. Overall, the simulations showed that sphere impact on ceramic materials can be captured, which further validates the upgraded viscosity regularized Johnson-Holmquist-2 material model.

Now, using the proper material model and numerical framework, it is possible to investigate the failure processes and their sequence in more details. For this purpose, the sphere impact test was simulated for impact velocities ranging from 100 to 300m/s, with 10m/s increments. The analysis showed that there exists a threshold impact velocity for which cone cracking is first initiated. In the simulations this impact velocity was found to be equal to 170m/s and independent of the ceramic tile thickness. A fully developed cone crack does however appear at higher impact velocities, the exact value of which depends on the tile thickness. This shows that cone crack propagation is subjected to wave propagation phenomena, but initiation is not. Furthermore, radial and lateral cracking was investigated. From both simulations and experiments it can be found that the lateral crack separates the tip and base of the cone. The radial cracks are then found to fragment only the base of the ceramic cone. The radial cracks also extend beyond the cone crack and fragment the remainder of the target. Better understanding the failure mechanisms and their timing was the purpose of the last part of this chapter, which was therefore successfully concluded.

Finally, in the current chapter a numerical framework was formulated to study sphere impact on ceramic material. The model results were found to give good agreement with experiments. Furthermore, the model was used to study the failure processes in more details. It can be concluded that the upgraded JH2-V model in the current numerical framework provides a good basis for future research related to sphere impact on ceramic material.

REFERENCES

[1] E. C. Simons, J. Weerheijm, G. Toussaint, and L. J. Sluys, *An experimental and numerical investigation of spherical impact on alumina ceramic,* International Journal of Impact Engineering (under review).

[2] E. Carton and G. Roebroeks, *Testing Method for Ceramic Armor and Bare Ceramic Tiles,* Advances in Ceramic Armor X , 1 (2015).

[3] J. E. Field, D. Townsend, and Q. Sun, *High Speed Photographic Studies Of The Ballistic Impact Of Ceramics,* in *Proceedings of Spie* (1989) p. 672.

[4] K. A. Iyer, *Relationships between multiaxial stress states and internal fracture patterns in sphere-impacted silicon carbide,* International Journal of Fracture **146**, 1 (2007).

[5] M. Yamada, K. Sekine, T. Kumazawa, and Y. Tanabe, *Relationship between the cone crack and fracture mode in ceramics under high-velocity-projectile impact,* Journal of the Ceramic Society of Japan **118**, 903 (2010).

[6] E. K. Oberg, C. S. Dunleavy, P. Bourke, and T. W. Clyne, *Electrical monitoring of crack propagation during quasi-static loading and ballistic impact of alumina plates,* Journal of the European Ceramic Society **33**, 2663 (2013).

[7] Z. Wei, A. G. Evans, and V. S. Deshpande, *The Influence of Material Properties and Confinement on the Dynamic Penetration of Alumina by Hard Spheres,* Journal of Applied Mechanics **76**, 051305 (2009).

[8] R. B. Leavy, R. M. Brannon, and O. E. Strack, *The use of sphere indentation experiments to characterize ceramic damage models,* International Journal of Applied Ceramic Technology **7**, 606 (2010).

[9] A. Sanders, I. Tibbitts, D. Kakarla, S. Siskey, J. Ochoa, D. Ph, K. Ong, R. Brannon, and P. D, *Dynamic Behavior of Materials, Volume 1,* Strain **1**, 229 (2011), arXiv:arXiv:1011.1669v3 .

[10] B. G. Compton, E. A. N. Gamble, V. S. Deshpande, and F. W. Zok, *Damage development in an armor alumina impacted with ductile metal spheres,* Journal of Mechanics of Materials and Structures **7** (2012).

[11] R. B. Leavy, J. D. Clayton, O. E. Strack, R. M. Brannon, and E. Strassburger, *Edge on impact simulations and experiments,* Procedia Engineering **58**, 445 (2013).

[12] G. R. Johnson and T. J. Holmquist, *A computational constitutive model for brittle materials subjected to large strains, high strain rates, and high pressures,* Shock Wave and High-Strain-Rate Phenomena in Materials (1992).

[13] G. R. Johnson and T. J. Holmquist, *An improved computational constitutive model for brittle materials,* AIP Conference Proceedings **309**, 981 (1994).

[14] G. R. Johnson, T. J. Holmquist, and S. R. Beissel, *Response of aluminum nitride (including a phase change) to large strains, high strain rates, and high pressures,* Journal of Applied Physics **94**, 1639 (2003).

[15] C. Simha, S. Bless, and A. Bedford, *Computational modeling of the penetration response of a high-purity ceramic,* International journal of impact engineering **27**, 65 (2002).

[16] V. S. Deshpande and A. G. Evans, *Inelastic deformation and energy dissipation in ceramics: A mechanism-based constitutive model,* Journal of the Mechanics and Physics of Solids **56**, 3077 (2008).

[17] V. S. Deshpande, E. A. N. Gamble, B. G. Compton, R. M. McMeeking, A. G. Evans, and F. W. Zok, *A Constitutive Description of the Inelastic Response of Ceramics,* Journal of the American Ceramic Society **94**, s204 (2011).

[18] G. Toussaint and I. Polyzois, *Sphere impacts on alumina ceramics: Experiments and finite element simulations,* in *43rd International Conference and Exposition on Advanced Ceramics and Composites* (2019).

[19] D. Shockey, A. Marchand, S. Skaggs, G. Cort, M. Burkett, and R. Parker, *Failure phenomenology of confined ceramic targets and impacting rods,* International Journal of Impact Engineering **9**, 263 (1990).

[20] J. López-Puente, A. Arias, R. Zaera, and C. Navarro, *The effect of the thickness of the adhesive layer on the ballistic limit of ceramic/metal armours. An experimental and numerical study,* International Journal of Impact Engineering **32**, 321 (2005).

[21] Y. F. Gao, Z. X. Si, L. J. Wang, X. Q. Zhang, and S. T. Liu, *Stress Distribution and Deformation Behavior of Alumina Ceramic after Mini Bullet Dynamic Impact,* Key Engineering Materials **768**, 140 (2018).

[22] Dynaflow Research Group, *Jem-jive,* http://jem-jive.com.

[23] G. R. Johnson and W. H. Cook, *A constitutive model and data for metals subjected to large strains, high strain rates and high temperatures,* (1983).

[24] Y. B. Guo, Q. Wen, and K. A. Woodbury, *Dynamic Material Behavior Modeling Using Internal State Variable Plasticity and Its Application in Hard Machining Simulations,* Journal of Manufacturing Science and Engineering **128**, 749 (2006).

[25] E. C. Simons, J. Weerheijm, and L. J. Sluys, *A viscosity regularized plasticity model for ceramics,* European Journal of Mechanics / A Solids **72**, 310 (2018).

[26] E. C. Simons, J. Weerheijm, and L. J. Sluys, *Simulating brittle and ductile response of alumina ceramics under dynamic loading,* Engineering Fracture Mechanics **216** (2019), https://doi.org/10.1016/j.engfracmech.2019.05.013.

[27] J. L. Zinszner, B. Erzar, P. Forquin, and E. Buzaud, *Dynamic fragmentation of an alumina ceramic subjected to shockless spalling: An experimental and numerical study,* Journal of the Mechanics and Physics of Solids **85**, 112 (2015).

[28] B. G. Compton, E. A. Gamble, and F. W. Zok, *Failure initiation during impact of metal spheres onto ceramic targets,* International Journal of Impact Engineering **55**, 11 (2013).

[29] S. Das, W. Ronan, H. N. Wadley, and V. S. Deshpande, *Penetration of confined ceramics targets,* Extreme Mechanics Letters **18**, 45 (2018).

[30] H. M. Hilber, T. J. Hughes, and R. L. Taylor, *Improved numerical dissipation for time integration algorithms in structural dynamics,* Earthquake Engineering & Structural Dynamics **5**, 283 (1977).

[31] H. Zolghadr Jahromi and B. A. Izzuddin, *Energy conserving algorithms for dynamic contact analysis using newmark methods,* Computers and Structures **118**, 74 (2013).

[32] D. Fernández-Fdz, R. Zaera, and J. Fernández-Sáez, *A constitutive equation for ceramic materials used in lightweight armors,* Computers & Structures **89**, 2316 (2011).

[33] E. C. Simons, J. Weerheijm, and L. J. Sluys, *Fully Implicit Plasticity Model for the Characterization of Ceramics in Ballistic Protection,* in *22nd Technical Meeting DYMAT 'Experimental Testing and Modelling of Brittle Materials at High Strain-Rates'* (Grenoble, 2016) pp. 17–22.

[34] E. de Souza Neto, D. Peric, and D. Owens, *Computational Methods for Plasticity,* 1st ed. (John Wiley & Sons Ltd, Chichester, 2008).

[35] M. D. Bolton, *The strength and dilatancy of sands,* Géotechnique **36**, 65 (1986).

[36] E. Detournay, *Elastoplastic model of a deep tunnel for a rock with variable dilatancy,* Rock Mechanics and Rock Engineering **19**, 99 (1986).

[37] E. A. N. Gamble, B. G. Compton, V. S. Deshpande, A. G. Evans, and F. W. Zok, *Damage development in an armor ceramic under quasi-static indentation,* Journal of the American Ceramic Society **94** (2011), 10.1111/j.1551-2916.2011.04472.x.

[38] P. Wriggers, T. Vu Van, and E. Stein, *Finite element formulation of large deformation impact-contact problems with friction,* Computers & Structures **37**, 319 (1990).

[39] H. E. Sliney, *The Friction and Wear of Ceramic / Ceramic and Ceramic / Metal Combinations in Sliding Contact,* Tech. Rep. (U.S. Department of Energy, 1993).

[40] J. Takadoum, *Tribological behaviour of alumina sliding on several kinds of materials,* Wear **170**, 285 (1993).

[41] R. Munro, *Evaluated material properties for a sintered alpha-alumina,* Journal of the American Ceramic Society **80**, 1919 (2005).

[42] M. M. Chaudhri and S. M. Walley, *Damage to glass surfaces by the impact of small glass and steel spheres,* Philosophical Magazine A **37**, 153 (1978).

[43] D. B. Rahbek, J. W. Simons, B. B. Johnsen, T. Kobayashi, and D. a. Shockey, *Effect of composite covering on ballistic fracture damage development in ceramic plates,* International Journal of Impact Engineering **99**, 58 (2017).

5

CONCLUSION

The goal of the thesis was to simulate sphere impact on a ceramic material and use simulations to understand the failure in ceramic under impact. The key focus of the research has been the constitutive modelling of ceramic material. A new constitutive model was proposed in this thesis. The model was based on the Johnson-Holmquist-2 (JH2) ceramic material model, which is often used to describe the behaviour of a ceramic under ballistic loading. The original model has been modified in two steps to ensure the predicted behaviour to be: (1) numerically sound and (2) physically correct. To obtain numerically correct results mesh dependency of the JH2 model had to be solved. For this purpose a viscosity was added to the hydrostatic tensile strength in the model. To improve the physically correctness of the model the plastic failure strain formulation was modified, to allow for both brittle failure under tension and ductile failure under compression. As a final step a numerical framework for sphere impact simulations was defined. Using this numerical framework and the improved constitutive model sphere impact experiments were simulated, leading to new insights on failure of ceramics under sphere impact.

The mesh dependency of the JH2 model and a solution for this problem were discussed in Chapter 2. Here a viscosity to the hydrostatic tensile strength was proposed, renaming the model to the viscosity regularized JH2 model, or simply JH2-V. A mixed linear / logarithmic viscosity formulation was used, to provide regularization at all loading rates but prevent unphysical growth of the failure zone under high rate loading. This mixed formulation was shown to give mesh independent results, removing any spurious localization of the failure as well as removing the mesh bias effect in the results. The newly introduced rate dependent tensile strength did not only solve for mesh dependency, it also allowed the model to capture rate dependency found in the spall strength of ceramic materials. This was not possible in the original JH2 model, but only in the JH2-V model.

The physical correctness of the JH2-V model developed in Chapter 2 was thoroughly examined in Chapter 3. Four experiments on ceramics were simulated using the JH2-V model with the main purpose to validate the results. This validation, however, revealed an inability of the model to predict both brittle failure under tension and ductile failure under compression. This inability was found to originate from the plastic failure strain formulation, used by the JH2 and JH2-V material models. In the original formulation the failure strain is a function of pressure, which should account for the difference between failure under tension and compression. However, this single formulation inadvertently couples the failure strain under tension and compression. As a result either failure under tension or compression could be captured correctly, but not both. A solution was found by upgrading the failure strain formulation, using two independent failure strains for high and low pressures. By using this failure strain formulation both brittle failure under tension and ductile failure under compression could be captured, with a single set of material parameters. The upgraded JH2-V model was shown to correctly capture the ceramic behaviour in all four experiments considered.

The upgraded JH2-V material model can be used to simulate ceramic behaviour, as the validation steps in Chapter 3 have shown. A final step towards sphere impact simulations is to define the full numerical framework in which these simulations should be performed. Model aspects related to the projectile, the contact and additional features for the ceramic constitutive model were considered in Chapter 4. Finally it was concluded that simulations should be performed in 3d, without contact friction or ceramic bulking. It was shown that all failure mechanisms could be captured by simulating in this numerical framework. Comparison of simulation results to experiments showed good agreement, although some discrepancies in cone crack initiation were found. The upgraded JH2-V model and the numerical framework were finally used to perform a detailed study of ceramic failure under sphere impact. This revealed a typical order of failure processes in the ceramic material and also showed how the failure mechanisms interact. A cone crack and a quasi-plastic zone are first to form. After some time radial cracks will appear, growing in radial direction as well as through the thickness of the ceramic target. Radial cracks are initially internal to the cone, but may grow beyond the cone towards the end of the interaction. The radial cracks extend through the thickness of the ceramic target up to the quasi-plastic zone. This is also the position where a lateral crack will form when the material is unloaded. A typical post-experimental specimen shows an ejected cone with a separated tip and a radially fragmented base. The ceramic target will also be split by radial cracks.

It is concluded that the upgraded JH2-V model can correctly capture ceramic behaviour under dynamic loading. In the current numerical framework sphere impact experiments can be correctly simulated. The constitutive model and numerical framework provide a good basis for future research related to sphere impact and other ballistic tests on ceramic material.

5.1. FUTURE RESEARCH

The constitutive model and numerical framework presented in this thesis allowed to successfully simulate sphere impact on a ceramic material. The sphere impact test was chosen because it is a simple and controllable dynamic test. The upgraded JH2-V constitutive model which was tested and validated on this sphere impact test may now also be used to the full scale ballistic loading of the ceramic armour system. Although the model was shown to give correct results in sphere impact, there will be new challenges when simulating ballistic loading on armour systems. Some of the future challenges were already revealed during the current project. This section will discuss some potential future research topics related to (1) the constitutive model, (2) the numerical framework and (3) experiments on ceramics.

5.1.1. CONSTITUTIVE MODEL

The JH2 ceramic material model was chosen as a base model. The upgraded JH2-V model is the final constitutive model used in this thesis. There are still some features in this model which are a good candidate for improvement. First some possible improvements from a physical point of view:

- In Chapter 4 of this thesis it was found that cone cracking in simulations appeared at lower velocities than in experiments. One possible explanation is that tensile failure is not properly captured in the current model. The current model relates the material strength and softening to the pressure state in the material. This might overestimate the material strength under combined tensile and compressive stresses. Some models try to deal with this by including a dependency on the lode angle [1, 2], or even on the principal stresses [3]. This changes the basis of the material model, but may be worth investigating.

- A new failure formulation was proposed for the JH2 material model, where softening under tensile and compressive states was separated. The model could be extended one step further by having two scalar damage variables to drive softening, one for tensile failure and one for failure under compression. The rationale is that failure under tension and compression not only accumulates differently, but also affects the material strength in a different way. For instance, lowering either the deviatoric or hydrostatic material strength.

Improvements for a constitutive model can have a physical justification, but there may also be numerically justified improvements. Consider that the Finite Element Method was used in the current thesis, in which the system of equations was solved using an implicit time integration scheme. This implicit integration scheme allows for large time steps and can result in relatively fast simulation of dynamic problems. To keep this implicit integration scheme robust the system of equations should be (near) linear. This is complicated, since material failure itself is inherently non-linear. Therefore, in Chapter 4, some non-linearities of the constitutive model were evaluated, to find and remove any unnecessary sources of non-linearity. More sources of non-linearity can be found in the JH2-V model than those discussed in Chapter 4. Two of these are discussed below. Obviously one must ensure the model still provides physically correct results after removing some non-linearity.

- The JH2 intact and residual strength formulations have a singularity in their derivate at their respective apexes. These singularities are detrimental to the local and global Newton-Raphson procedure. A change in the strength formulations may alleviate this. For example, using a strength formulation such as in the JHB model [4], where there is no singularity at the apex. Since the apex deals with low or negative pressure behaviour this may very well be studied together with better capturing tensile failure in the model.

- The JH models maintain a constant ultimate hydrostatic tensile strength up to the point of full failure. In the JH2-V model the ultimate hydrostatic tensile strength is even increased as function of loading rate. In both models there is no mechanism which lowers the hydrostatic tensile strength, except for full failure when there is a sudden collapse to zero strength. Providing a smooth softening of the hydrostatic tensile strength to zero may improve convergence behaviour of the local and global system of equations. Furthermore, from a physical point of view a softening of the hydrostatic tensile strength may even be a more realistic approach to damage. This topic may be studied together with a separation of the damage variables, as a tensile damage variable may be a good candidate to drive hydrostatic strength reduction.

Although the focus has been on the ceramic material model, it should be kept in mind that there are two materials involved in this interaction, the other being from the projectile. In the current thesis the projectile was simplified to one material (steel) and a Johnson-Cook (JC) model was chosen for the projectile in the simulations. Two factors were not considered in the current simulations, they may be included to improve the simulation results:

- Temperature and loading rate effects in the JC model. Currently the model parameters for this projectile were simplified to ignore these effects. Temperature effects are likely to lower the yield strength of the projectile, while rate effects will increase its strength.

- Failure of the projectile. Experiments showed not only plastic deformation of a projectile, but also severe fragmentation for high impact velocities. This fragmentation was not captured by the current projectile material model.

Both the temperature/rate effect and failure of the projectile are likely to change the exerted force by the projectile onto the ceramic. Properly capturing these effects may give more physically realistic results.

5.1.2. NUMERICAL FRAMEWORK

In Chapter 4 a framework was presented to properly simulate sphere impact on a ceramic material. There are many more options related to the framework which one may consider, apart from choosing the best ceramic material model. There are two consideration which will become more important as higher impact velocities are to be studied. This is related to large deformation and rotation found in some of the sphere impact simulations. Two extensions of the current framework should be considered:

- In the current framework the model is based on infinitesimal strain (small strain). In some impact experiments deformations are large and an extension to large deformation should be considered. For this, use a strain measure which can describe large rotation and deformation. Since this adds a geometric non-linear behaviour to the system, its effect on convergence for the implicit time integration scheme should be reinvestigated.

- Apply either element erosion schemes or re-meshing algorithms to solve for element inversion. The former may be simple, but choosing the right erosion scheme is difficult and may reintroduce mesh dependency to the problem. The latter approach is more appealing from a theoretical point of view, as energy and mass in the system can be maintained. However, re-meshing may be costly and some loss of accuracy due to data transfer is to be expected.

5.1.3. EXPERIMENTAL WORK

This work has been numerical in nature, with a strong focus on constitutive modelling. To validate the upgraded JH2-V model results, experiments are indispensable.

- Many experimental results can be found from literature, even large collections of experimental results [5]. However, consistent data sets for which the same ceramic has been used in a wide range of experiments is lacking. This became clear in Chapter 3, where the simulation results were thoroughly compared to experiments. Unfortunately the experimental results did not originate from the same source and although the ceramic material was similar, it was not the same. Ideally one would need to have a consistent set of experiments performed on the same material.

- In Chapter 4 a qualitative analysis of sphere impact and the damage in ceramic was performed. The simulation results could also be studied quantitatively, for instance by measuring the cone angle under an increasing impact velocity. This would provide valuable information necessary to improve the final armour system behaviour. However before the numerical results can be used for a quantitative analysis they need to be validated. Although current research presents some quantitative results [6], the quantitative data show great variation. New experiments will be needed, with a larger number of tests to clearly identify trends in the quantitative data.

- In Chapter 4 the simulation results were used to analyse timing of failure. This is one of the strongest points of the simulation, since one is able to follow ceramic failure internally and as a function of time. Interesting observations on interaction of cone and radial cracks were done. Although strength and failure of the material model were thoroughly validated for individual load cases, it makes sense to also validate the timing of failure for the considered sphere impact cases. For instance one needs to know when a cone crack initiates and when it is fully developed. There is a serious challenge here for the experiments. A good approach is to simplify impact loading and first study crack propagation in notched specimens under impact, such as done in [7]. Although more challenging loading conditions can also be studied, as is shown in [8] where the radial crack velocity is determined in an alumina ceramic under sphere impact.

REFERENCES

[1] D. Bigoni and A. Piccolroaz, *Yield criteria for quasibrittle and frictional materials,* International Journal of Solids and Structures **41**, 2855 (2004), arXiv:1010.1823 .

[2] D. Fernández-Fdz, R. Zaera, and J. Fernández-Sáez, *A constitutive equation for ceramic materials used in lightweight armors,* Computers & Structures **89**, 2316 (2011).

[3] C. Simha, S. Bless, and A. Bedford, *Computational modeling of the penetration response of a high-purity ceramic,* International journal of impact engineering **27**, 65 (2002).

[4] G. R. Johnson, T. J. Holmquist, and S. R. Beissel, *Response of aluminum nitride (including a phase change) to large strains, high strain rates, and high pressures,* Journal of Applied Physics **94**, 1639 (2003).

[5] T. J. Holmquist, A. Rajendran, D. W. Templeton, and K. D. Bishnoi, *A Ceramic Armour Material Database*, Tech. Rep. (TARDEC, Warren, Michigan, 1999).

[6] G. Toussaint and I. Polyzois, *Sphere impacts on alumina ceramics: Experiments and finite element simulations,* in *43rd International Conference and Exposition on Advanced Ceramics and Composites* (2019).

[7] Y. Duplan, P. Forquin, B. Lukić, and D. Saletti, *Numerical analysis of a testing technique to investigate the dynamic crack propagation in armour ceramic,* EPJ Web of Conferences **183**, 3 (2018).

[8] E. K. Oberg, C. S. Dunleavy, P. Bourke, and T. W. Clyne, *Electrical monitoring of crack propagation during quasi-static loading and ballistic impact of alumina plates,* Journal of the European Ceramic Society **33**, 2663 (2013).

ACKNOWLEDGEMENTS

Delft, January 2020

This is it, the end of an interesting five and a half year journey. These are the final words I will write to complete this thesis. A thesis which would not have been possible without the help of many people. I am grateful for all the help that I have received and would like to use these final words to thank those who have contributed most to the thesis you see before you.

First and foremost I would like to thank my supervisors Bert Sluys and Jaap Weerheijm. Without you this thesis would simply not have been possible. Bert, I appreciated the open door policy where you were immediately ready to discuss any problems I faced in our research and always were able to provide me with useful new leads. Jaap, I enjoyed sharing ideas and together trying to explain the many challenging experimental and numerical results we encountered.

I would like to thank the explosions, ballistics and protection group from TNO. From which this research was initiated and supported. Every visit gave me valuable new ideas and background information on experiments or applications of ceramic armour.

I would also like to thank the international partners I met through a TNO collaboration. This collaboration provided me with a platform to share ideas with experts in the field from the Swedish FOI and the Canadian DRDC. From the Canadian research institute DRDC I would like to thank both Geneviève Toussaint and Ionas Polyzois. Who kindly provided me with new experimental results for my final journal paper.

Erik Jan Lingen, who thought me the basics of C++ and JemJive. Frans van der Meer, who has helped me to see the power of JemJive and provided me with the needs to get started in my research. Frank Everdij, who has been a valuable support during my PhD. Not only has he provided me with everything I needed to perform my simulations, he as also showed me tips and tricks on how to be a good software developer. I also thank my office neighbours Anneke and Jaap. Who made me feel welcome every day and ensured the day would always start with a smile.

My former colleagues at the TU Delft for our daily lunches, coffee breaks, walk & talk in the Mekelpark and the weekly beers in PSOR. Sharing our knowledge and love for the research field we were in, but also exchanging ideas about anything we see in the world around us. I would like to extend special thank Prashanth, Yaolu, Tiziano, Kai, Adriaan, Mehdi, Iuri, Noori, Ali, Jafar, Fariborz, MZ, Marcello and Luís.

Finally I would like to thank my friends and family. My swimming friends, with whom I spent countless hours training before dawn. Anne, who stood by my side for the duration of my PhD. My twin sister Karin, her fiancé Lars and both my parents. All who have given me their love and support needed to finish this PhD journey.

Erik Simons

CURRICULUM VITÆ

Erik Cornelis SIMONS

22-01-1989	Born in Leiden, the Netherlands.
2001-2007	Grammar School Rijnlands Lyceum Wassenaar, the Netherlands
2007-2010	Bachelor in Civil Engineering Delft University of Technology, the Netherlands *Thesis:* Top Beam Buckling of Truss Bridges
2010-2013	Master in Civil Engineering Delft University of Technology, the Netherlands *Thesis:* Simulation of Strain Localization with an Enriched Gradient-Enhanced Damage Model
2014-2019	PhD candidate in Computational Mechanics Faculty of Civil Engineering and Geosciences Delft University of Technology, the Netherlands *Supervisor:* Dr. ir. J. Weerheijm *Promotor:* Prof. dr. ir. L.J. Sluys
2019-current	Scientific Software Engineer Nearfield Instuments

LIST OF PUBLICATIONS

JOURNAL ARTICLES

3. **E. C. Simons**, J. Weerheijm, G. Toussaint, L. J. Sluys, *An Experimental and Numerical Investigation of Spherical Impact on Alumina Ceramic*, International Journal of Impact Engineering, under review.

2. **E. C. Simons**, J. Weerheijm, L. J. Sluys, *Simulating brittle and ductile response of alumina ceramics under dynamic loading*, Engineering Fracture Mechanics, **216**, 2019.

1. **E. C. Simons**, J. Weerheijm, L. J. Sluys, *A Viscosity Regularized Plasticity Model for Ceramics*, European Journal of Mechanics / A Solids, **72**, 2018.

CONFERENCE CONTRIBUTIONS

4. **E. C. Simons**, J. Weerheijm, L. J. Sluys, *A Mesh-Independent Material Model for Quasi-Static and Dynamic Simulation of Ceramic Armour*, In: CERMODEL - Modelling and Simulation Meet Innovation in Ceramics Technology, Trento, Italy, 2017.

3. **E. C. Simons**, J. Weerheijm, L. J. Sluys, *Mesh-Independent Damage-Plasticity model for the Characterization of Ceramics*, In: 22nd DYMAT Technical Meeting, Grenoble, France, 2016.

2. **E. C. Simons**, J. Weerheijm, L. J. Sluys, *Mesh-Independent Damage-Plasticity model for Ceramics in Ballistic Protection*, In: 26th International Congress of Theoretical and Applied Mechanics, Montreal, Canada, 2016.

1. **E. C. Simons**, J. Weerheijm, L. J. Sluys, *A Mesh-Independent Damage-Plasticity model for the Characterization of Ceramics in Ballistic Protection*, In: European Congress on Computational Methods in Applied Sciences and Engineering, Crete, Greece, 2016.